Kenneth Simonsen
Robert Stevens

Investigation on
LONG-SPAN SUSPENSION BRIDGES DURING ERECTION
The Great Belt East Bridge

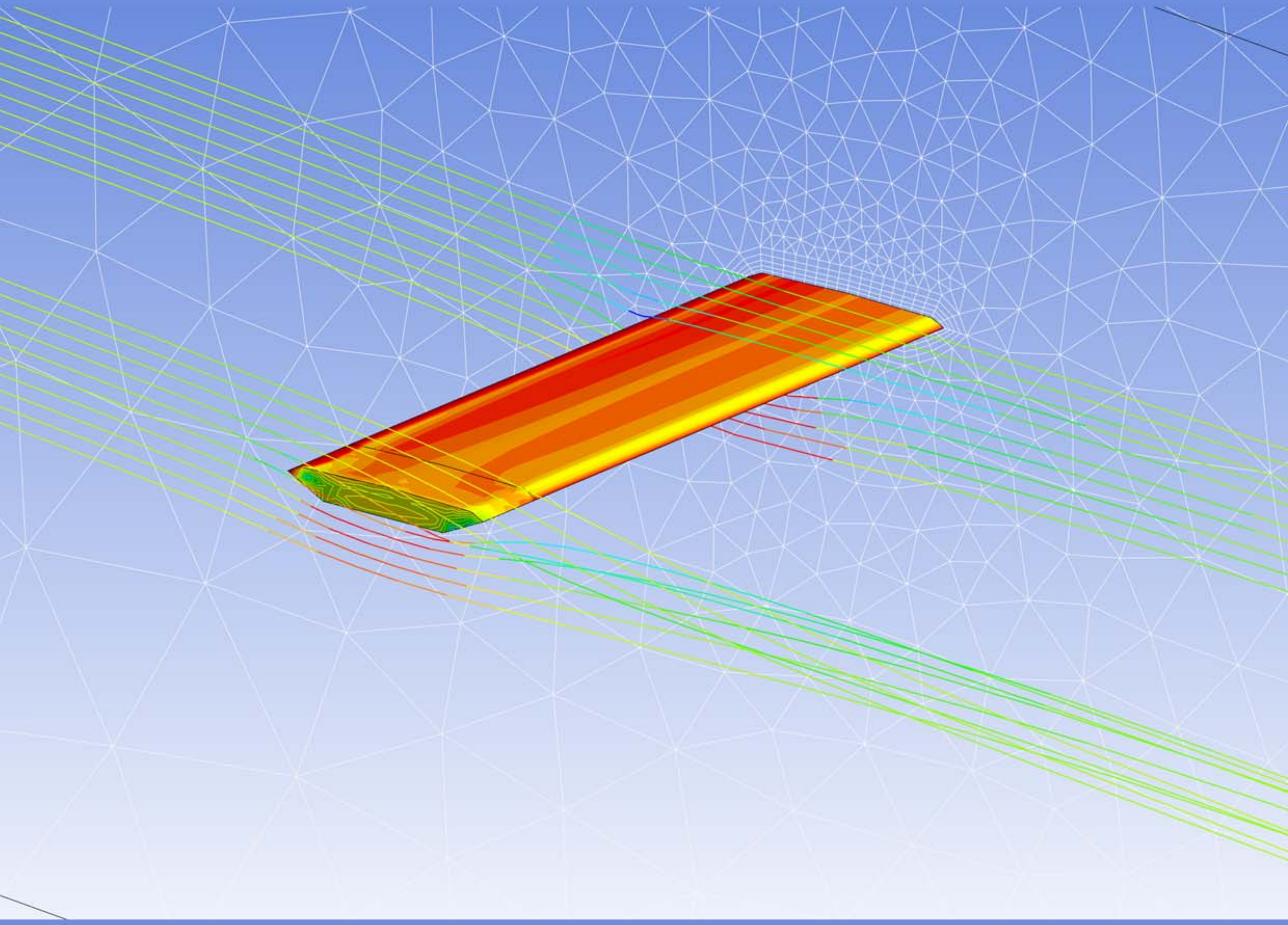

Department of Civil Engineering
Aalborg University 2008
Master of Science in Civil and Structural Engineering

ABSTRACT

In this rapport, the aeroelastic phenomenon, flutter is investigated for the Great Belt East Bridge. The bridge is examined at two different stages during construction: when only 15% of the bridge deck is mounted and when the bridge is fully erected. A numerical approach, CFD, is used for both stages.

According to the well-known Scanlan theory, the aerodynamic loads are described by a set of aerodynamic parameters, which can be derived by use of different approaches. These aerodynamic derivatives are found by a two dimensional analysis of the cross section of the bridge, by a forced oscillation test. The derivatives are used in determination of the critical flutter wind velocity for the fully erected bridge. The purpose of this 2d-test is to validate the CFD as a mean of computing critical flutter wind velocities. The resulting critical flutter wind velocity of $71.9\frac{m}{s}$ found, is not far from the velocity found in wind tunnel tests, $70\frac{m}{s}$ to $74\frac{m}{s}$.

For the investigation of the bridge during erection, two three dimensional analysis are performed. A forced vibration test is performed in a similar way as for the two dimensional case. In this analysis the fluid is allowed to flow around the free end of the bridge, introducing some end effects. The structural behavior of the bridge during construction shows that the lowest vertical eigenfrequency is very close to the lowest torsional eigenfrequency. This implies that the critical flutter wind velocity should be somewhat lower for the bridge during construction. This velocity is found at $47.6\frac{m}{s}$. Wind tunnel tests of this construction stage show a critical flutter wind velocity of $43.3\frac{m}{s}$

The rapport further investigates the possibility of using a fully coupled fluid-structure interaction when determining critical flutter wind velocities. A two degree of freedom system is used to determine the motion of the bridge deck, which is assumed rigid. A first order backward Euler integration scheme is applied in Ansys 11 when prescribing the movements of the system. The mesh of the fluid domain is very coarse, in order to reduce the computation time. The simulations have been run, but with some difficulties with respect to damping. The test show a critical flutter wind velocity of approximately $20\frac{m}{s}$ to $25\frac{m}{s}$ which is far lower than the wind tunnel tests. The test is, however described in the report, as the method gives a very good visual and physical understanding of the aeroelastic phenomenon.

PREFACE

The present work is the final thesis for the Master's degree in Civil and Structural Engineering at the University of Aalborg, by Robert Stevens and Kenneth Simonsen. The purpose is to investigate the subject of aerodynamic instability of long-span suspension bridges. The work is verified by using experimental data from wind tunnel tests of the Great Belt Bridge. The phenomenon is considered for both a bridge during construction and a fully erected bridge.

The report has been composed in the period from the 3rd of February 2008 to the 11th of June the same year. The work has been supervised by assistant professor Jesper Stærdahl, Professor Niels Sørensen and senior project manager of the bridge department in Rambøll, Lars Thorbek.

The procedure for the computations is documented in such a way, that the results can be reproduced in the future, and the investigations continued. Furthermore, programs and simulation data are available on the enclosed CD. References are provided by use of the Harvard Method.

Kenneth Simonsen Robert Stevens

Date of completion: 11th of June 2008.

Total number of pages:

Pages in appendix:

Number of publications: 4

TABLE OF CONTENTS

1. PRELIMINARIES

1.1. INTRODUCTION TO THE REPORT

The research on fluctuating wind loads on long-span cable-supported suspension bridges is an ongoing process, encouraged by the increasingly larger bridge spans. The increase in bridge span has often been implemented without a proportional increase in stiffness, which has resulted in large flexibility of most of the cable-supported bridges seen today. Large flexibility often leads to large vibration amplitudes and under special conditions to the total collapse of the bridge, as seen with Tacoma Narrows Bridge.

Suspension bridges must be designed to support the static wind forces, lift, drag and moment, created by the mean wind, but also the dynamic load cases, created by an interaction between the wind force and structural motion, known as aeroelasticity. Aeroelasticity can be said to be the mutual interaction of forces, originating from inertia, elasticity (forces from elastic deformation), and aerodynamics. The aeroelastic phenomena seen for long-span suspension bridges are flutter, galloping and vortex shedding induced vibrations. Flutter is chosen as the focus area of this report. In chapter 3 the phenomena are shortly described.

At the moment, the investigation of the stability of bridges is widely based on wind tunnel testing, but as Computational Fluid Dynamics (CFD) simulation techniques have developed, so has the use of these to reduce the expensive and time-consuming wind tunnel tests. Furthermore, use of CFD gives the opportunity for good visualization of the flow conditions, and thereby a better understanding of the problem at hand. CFD is only used as a complement to the wind tunnel tests, which is essential in proofing of the stability of the bridge. Implementing CFD does not serve as a replacement for the wind tunnel tests, but is instead used as a tool to document the results from the experiments supplemented by the possibility of easily changed input parameters, and thereby small parameter studies, and as mentioned before, the use of simulation tools.

1.2. PURPOSE OF THE REPORT

The purpose of this report is to show to which extend it is possible to use CFD to consider the stability problems that can occur in large flexible cable-supported suspension bridges due to aeroelastic phenomena. As mentioned in the introduction, CFD does not replace the wind tunnel tests, but is used as a complimentary tool. Therefore, the calculations by CFD must be verified, by comparing the calculated results with experimental values. This is done to clarify the reliability and robustness of the CFD-simulations. The simulation is not considered to be useful if the experimental values can not be reproduced. The Great Belt East Bridge is used throughout this thesis because plenty of investigations have been carried out previously. This makes a very good reference for a comparison of results.

As a starting point, the CFD-simulations are verified by treating a 2d bridge section, and analyzing the flutter phenomenon by finding the aerodynamic derivatives and critical values. The CFD-simulation is given boundary conditions, mesh refinement and other variables, so that the experimentally found values can be reproduced and a comparison with the experimental values will show any inaccuracies in the modeling assumptions.

With the knowledge gathered from the 2d simulation, CFD is implemented in finding the aerodynamic derivatives and critical values with consideration of end flow around the bridge deck, simulating the construction phase. Experimental data is also available for this situation, and the CFD-simulation can therefore also be verified.

The main purpose of this report can be said to be enabling CFD programs to simulate stability problems for large flexible cable-supported bridges. When the results are satisfactory, the tools integrated in the used simulation tool, are used to create a basis for a better understanding of the problem.

2. TREATMENT OF FLUTTER

2.1. INTRODUCTION

The purpose of this chapter is to describe how the flutter phenomenon has been treated in previous work. For a short introduction to the flutter phenomenon in general, see section 3.2.4. The report focuses on the CFD-approach, but the calculations in this report are verified by use of results from wind tunnel tests, described in section 2.3. The results from the tests are available in [Hansen 2008] and [Hansen 1996].

2.2. STUDY OF PREVIOUS WORK

In order to start an investigation of aerodynamic properties of long span bridges, it seems natural to comment on some previous results. In the following, a short introduction is given to a few of the papers and references used in this thesis. All the papers and references deal with the analysis of the flutter phenomenon for the Great Belt East Bridge.

[Hansen 1996] is an analysis of critical flutter wind velocities for the Great Belt East Bridge during construction. The report was carried out by Svend Ole Hansen ApS for the company Steinman in order to comment on the work done by the consulting engineers from COWI. The report is based on wind tunnel tests and concludes that the critical stage during construction is when five bridge sections have been erected. The bridge deck is at that stage 249 meters long. The natural frequencies and modal masses used in [Hansen 1996] have been adopted in this thesis. The resulting critical flutter wind velocity has been found to $43.3\frac{\text{m}}{\text{s}}$. The flutter phenomenon is found to occur as a coupling between the two lowest eigenmodes for torsion and vertical translation.

[Frandsen 2003] has carried out extensive numerical bridge deck studies using CFD. She uses a coupled fluid structure formulation in finding critical flutter wind velocities for the fully erected bridge. The fluid domain is meshed rather coarse, but the results are surprisingly good. Even though the smallest mesh elements have a characteristic length of approximately one meter, she captures the beginning of a vortex street behind the bridge deck. The fluid domain is modeled with 1900 nodes in an irregular unstructured mesh. [Frandsen 2003] finds the Strouhal number for the Great Belt East Bridge to be $St = 0.26$, which is somewhat higher than the values measured in wind tunnel tests, which show $0.11 \le St \le 0.15$. [Frandsen 2003] finds the critical flutter wind velocity for the fully erected bridge to be between $65\frac{\text{m}}{\text{s}}$ and $70\frac{\text{m}}{\text{s}}$. This is slightly lower than the values measured in the wind tunnel of the Danish Maritime Institute in 1992 and 1993. These tests show critical flutter wind velocities between $70\,\frac{\text{m}}{\text{s}}$ and $75\,\frac{\text{m}}{\text{s}}$. The conclusion of the paper is that computational fluid dynamics, combined with a finite element model of the structure, may provide a good approximation to the critical flutter wind velocities. The results are however not good enough to trust without verification from wind tunnel testing.

[Awruch and Braun 2003] employs two different techniques for finding critical flutter wind velocities. A forced vibration test has been performed in a numerical model where the fluid domain is modeled with 8400 nodes. The vibrations are simulated by altering the angle of the wind in the inlet. The test is used in deriving the aerodynamic derivatives. The critical flutter wind velocity has been found to be $73\,\frac{\text{m}}{\text{s}}$. [Awruch and Braun 2003] has also carried out a fluid-structure interaction on the same mesh of 8400 nodes. The work shows a critical flutter wind velocity of $69\,\frac{\text{m}}{\text{s}}$. Both results are relatively close to the results found in wind tunnel tests, as mentioned earlier. The Strouhal number is found to be $St = 0.18$, which in also close to the measured values.

2.3. WIND TUNNEL TESTING

The approach used in this report, is verified by use of results from aeroelastic tests of the Great Belt Bridge performed in a wind tunnel. The procedures used in the CFD simulations are conducted so that the results produced are based, if possible, on the same assumptions and presented in the same way.

Model testing in a wind tunnel are dependent on model laws, which ensures the correct interpretation of the test results when using scaled models. The model laws can be used to consider the following forces on a scaled model:

- Inertia forces
- Gravitational forces
- Viscous forces

In aeroelastic models, the dominating forces are identified as the inertia forces from the wind flow since these forces create the motion-induced wind loads. The inertia forces must be scaled correctly, so the response of the model, in the wind tunnel is similar to full scale. This means that it is of major importance that the natural frequencies, defined by mass and stiffness, and the structural damping in the model are scaled correctly. Usually this is done by use of Froude's model law. It is well known that Reynolds's model law is very difficult to fulfill for scaled wind tunnel testing, since this only could be done by use of a different fluid or by using extreme wind velocities. The viscous forces of a wind tunnel tests are therefore not correctly scaled, but since flow separation for a bridge deck profile mainly is dictated by the sharp edges of the bridge deck, and therefore not dependent of Reynolds number, this has small significance in this case. [Hansen and Dyrbye 1997]

Aeroelastic model testing in a wind tunnel is a complicated affair, when all the significant modes, contributing to a phenomenon such as flutter, are to be modeled correctly. Furthermore, the scaled model must contain all the geometrical details, and building a model is therefore a very time consuming and expensive assignment. Due to these difficulties, an aeroelastic section model test is often used when determining critical flutter wind velocities in a wind tunnel. In these tests the bridge deck is modeled as a rigid body where the masses and stiffnesses are modeled at the end of the section model. An example of the setup of an aeroelastic bridge in a wind tunnel can be seen on Figure 1.

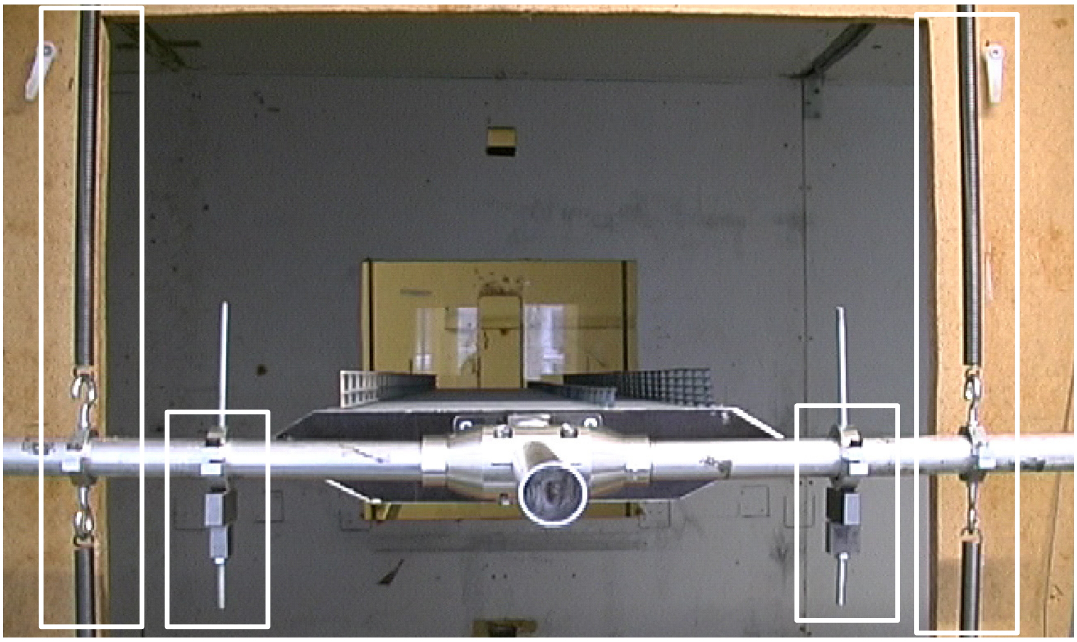

Figure 1: Aeroelastic model in a wind tunnel. The modal parameters of the bridge are ensured by the weights and springs, marked on the figure.

When investigating the bridge during the erection phase, the section model is withdrawn from the entire width of the tunnel, thereby allowing flow around the free end. The critical flutter wind velocities can be determined by three different methods [Hansen and Dyrbye 1997]:

1. Vibration test –Transient behavior of the bridge is considered after an initial displacement
2. Forced oscillation test – Forces from a known oscillation are used.
3. Buffeting tests – The bridge deck behavior is analyzed for different velocities.

Wind tunnel tests are usually based on method 1 and 2. It is possible to use method 3, where the forces are measured for a known oscillation, by use of pressure taps on the bridge decks surface, but this method gives some practical complications. Placing pressure taps on the model is very time consuming and ads to the complexity of the model and the demand in equipment. Introducing a known forced oscillation can also be difficult. Therefore, method 1 is usually used, where the transient behavior of the bridge is observed, when this is given and initial displacement. This method is also used in this report. Method 3 also gives a good illustration of the aerodynamic instability, since a correctly scaled model, will go into flutter at the critical velocity, and the behavior is similar to that in full scale. Method 3 can therefore be introduced, by testing the bridge for increasing wind velocities, and observing when instability occurs.

3. THE NATURE OF WIND LOADS ON BRIDGE DECKS

3.1. INTRODUCTION

In this chapter an introduction to the load phenomena occurring on bridge decks are given. As mentioned in the preliminaries, the report focuses on the flutter phenomenon, but knowledge of other phenomena is essential for fully understanding the nature of the problem and thereby understanding the solution method. Furthermore, the simple description given in this chapter will be of use later on to understand the basis of the computational model created.

As mentioned in the introduction, the effects occurring when flexible long-span suspension bridges are subject to wind-induced forces, can be rather extreme and in the most severe situations leading to collapse. In the following, the wind-induced motions will be described in more detail, but with focus on the flutter phenomena.

3.2. WIND-INDUCED FORCES ON BRIDGE DECKS

A bridge deck immersed in a flow interacts with the flow, and is as a result of this exposed to surface pressures. The incoming turbulent flow will cause the forces on the bridge deck to be time dependent. Furthermore, for almost any, not perfectly, streamlined shape, signature turbulence created by the body itself also causes the lift, drag and moment to be time-varying. Normally, the forces are divided into static forces, associated with the mean wind, and forces related to the pressure fluctuations, caused by the turbulence, often referred to as buffeting. In general it can be said, that the influence the wind load has on bridge decks, regardless of the origin, are dependent on the aerodynamic characteristics of the bridge deck. For example, a perfectly streamlined deck can be designed so no lift force will occur, but naturally the outline of a bridge deck is dependent on other parameters such as strength, size requirements and practical measures which seldom make such a design possible. [Scanlan 1993] [Vario 2002].

Wind-induced loads on bridge decks are often divided into three different categories.

- Extraneously induced excitation. This covers dynamic loads due to turbulence in the incoming wind. It is not commonly seen that extraneously induced loads give rise to very large movements, as the energy in the incoming wind normally is very low at the structures lowest eigenfrequencies. The motions caused by fluctuating winds are known as buffeting.

- Instability caused by turbulence created by the structure itself, known as signature turbulence. This covers the well known Von Kármán's Street which is likely to be in resonance with the structure.
- Aerodynamic instability (negative damping) – where motion-induced wind loads arises on the structure. This covers phenomena such as galloping and flutter.

[Morgenthal 2000]

Before describing the different flow phenomena in detail, a more overall description of the flow situation is performed. This description is done the easiest by considering the bridge deck to be motion-less and thereafter moving.

In general, the wind-induced forces on a bridge section can be divided into the following parts, as previously described.

$$F_{tot}(t) = F_m + F_t(t) + F_{ae}(t) \tag{3.1}$$

where

F_{tot} is the total wind load on the bridge section

F_m is the mean wind load

F_t is the turbulent wind load, from the signature turbulence and buffeting

F_{ae} is the aeroelastic forces from the motion-induced wind loads

[Vario 2002]

The origin of the loads for a motionless and moving bridge deck will be described in the following section.

3.2.1. MOTIONLESS BRIDGE DECK

For a motionless bridge deck, the time-varying wind-induced loads are generated by the turbulence, and the mean wind is assumed to create a static load. The turbulence for a motionless deck can be divided into turbulence from the incoming wind and the signature turbulence. The turbulence in the incoming wind is traditionally treated in two parts. This can be closely connected to the procedure in which wind loads on structures are treated, for example in [EN 1991-1-4 2005], where the turbulence is divided into background turbulence, and resonant turbulence. Background turbulence is associated with the high energy levels in the low frequent turbulence. For cases in which the turbulence length scale, associated with the background turbulence, is large compared to the characteristic size of the bridge section, a large correlation of the wind forces are seen across the bridge section for the turbulence in the incoming wind. In such cases the wind force can be treated as quasi-static. In case of resonant turbulence, vortices act with frequencies close to the structures eigenfrequency, as seen with vortex shedding. In a similar way, as with the background turbulence, the correlation is also of significant importance.

The correlation between the signature turbulence and the turbulence in the incoming wind is also of importance, but usually the two components are treated separately, assuming no correlation since the frequency of the two contributions are separated.

If the characteristic size of the bridge is larger than the turbulence length scale, the background turbulence, and in some cases the resonance turbulence, cannot be treated as quasi-static. This is often the case for large bridges. The difference from the quasi-static case is usually described by use of aerodynamic admittance functions, which described the lack of correlation [Hansen and Dyrbye 1997]. In this case, the harmonic contents of the two turbulence contributions, signature turbulence and the turbulence in the incoming wind, must be treated as working together.

3.2.2. MOVING BRIDGE DECK

In a similar way as for the motionless bridge deck, the description of the wind-induced loads is done in both a quasi-static and a dynamic state.

In the quasi-static state, it can be assumed that the aerodynamic forces acting on the bridge section are solely dependent on its current motion, since this force can be calculated as the velocity pressure, from the difference in the moving speed and the speed of the incoming wind. When not treating the problem as quasi-static, the wind-induced force is no longer independent of the bridge decks previous motion, as shown later in this report. Consideration of the motion of the bridge deck can be taken into account by use of the aerodynamic derivatives, defined in detail later in this section. It is seen that the derivatives are dependent on a reduced frequency, which in a similar way as can be shown for the aerodynamic admittance function, works as a frequency filter on the wind components, making it possible to describe the self-excited forces for different motion patterns. The procedure for this is described in detail later in this section. [Hansen and Dyrbye 1997] [Scanlan 1993]

A more detailed explanation of some of the wind-induced loads can be found in the following sections.

3.2.3. VORTEX SHEDDING

Periodic movements of a structure may happen when the vortices formed around the body is shed at a frequency close to the eigenfrequency of the structure. Both vertical and torsional modes can be considered. A principal sketch of the phenomenon is seen on the figure below.

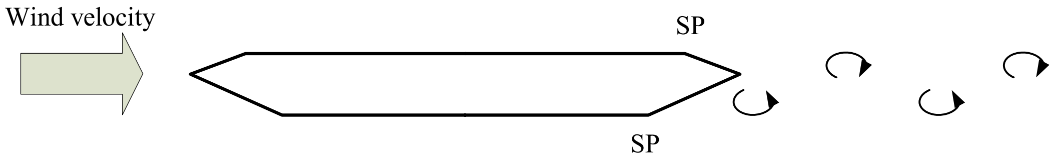

Figure 2: Principal sketch of the vortex street created by a bridge deck. SP indicates the separation points where the vortices are shed from the bridge deck.

Vortex induced motions can be avoided by ensuring that the frequencies of the vortices created are widely separated from the structures natural frequencies. This is done by altering the geometry of the bridge design or changing the natural frequencies. [Morgenthal 2000]

The shedding frequency, defined in(3.2), can be found by considering the vortices in the vortex street behind the bridge. The shedding frequency is usually described by use of Strouhal's number, defined in (3.2).

$$\begin{aligned} f_s &= \frac{v_{vs}}{l_v} \\ f_s &= S_t \frac{U}{D} \end{aligned} \tag{3.2}$$

where

f_s	is the shedding frequency [Hz]
v_{vs}	is the mean wind velocity in the vortex street [m/s]
l_v	is the length between the vortices [m]
U	is the mean wind velocity in the incoming wind [m/s]
D	is a characteristic length, usually the height of the bridge [m]
S_t	is Strouhal's number [-]

[Hansen and Dyrbye 1997]

The necessary values for determination of Strouhal's number for the bridge deck, treated in this report, can be found by use of two contour plots from the simulation, one illustrating the horizontal velocity and one illustrating the vortices.

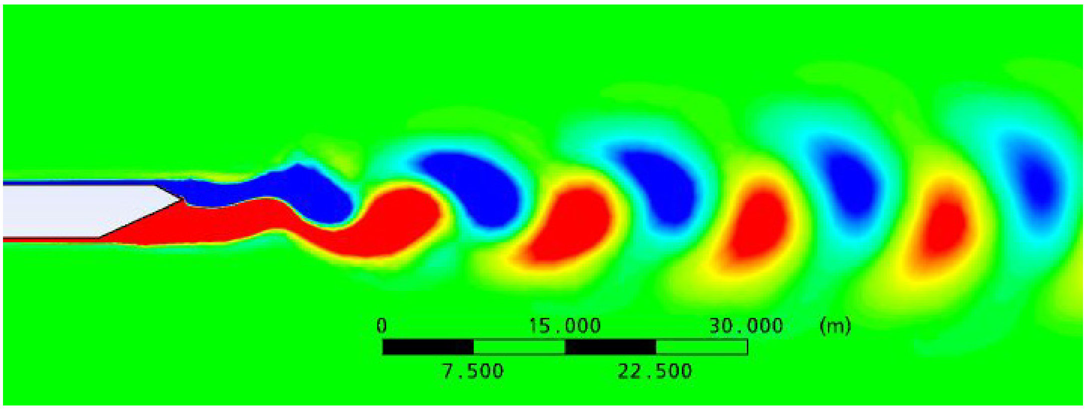

Figure 3: Vortices created behind the bridge deck.

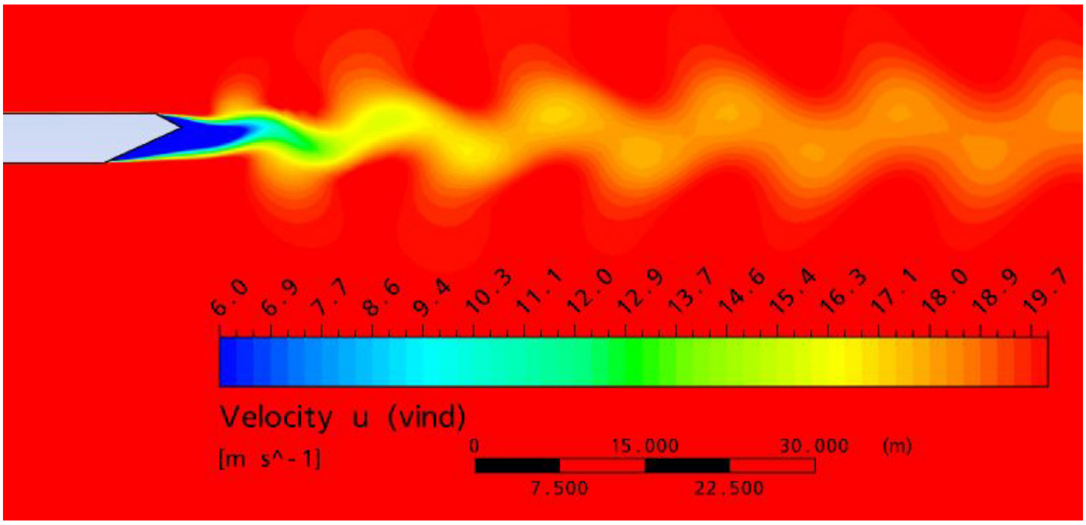

Figure 4: Horizontal velocity behind the bridge deck.

The necessary values can be extracted visually from the two figures, and the Strouhal's number can then be found by use of (3.2).

A more correct way would be by considering the moment load from the shed vortices in the frequency domain. This is seen in Figure 5. The spectrum is found for incoming winds of 20 $\frac{m}{s}$ and Strouhal's number is then found to 0.27. This is a rather high value, which could be caused by some complications in simulation of the turbulent boundary layer. This is not investigated further. Wind tunnel measurements give Strouhal's number between 0.11-0.15 and [Awruch and Braun 2003] finds Strouhal's number by use of CFD to 0.18.

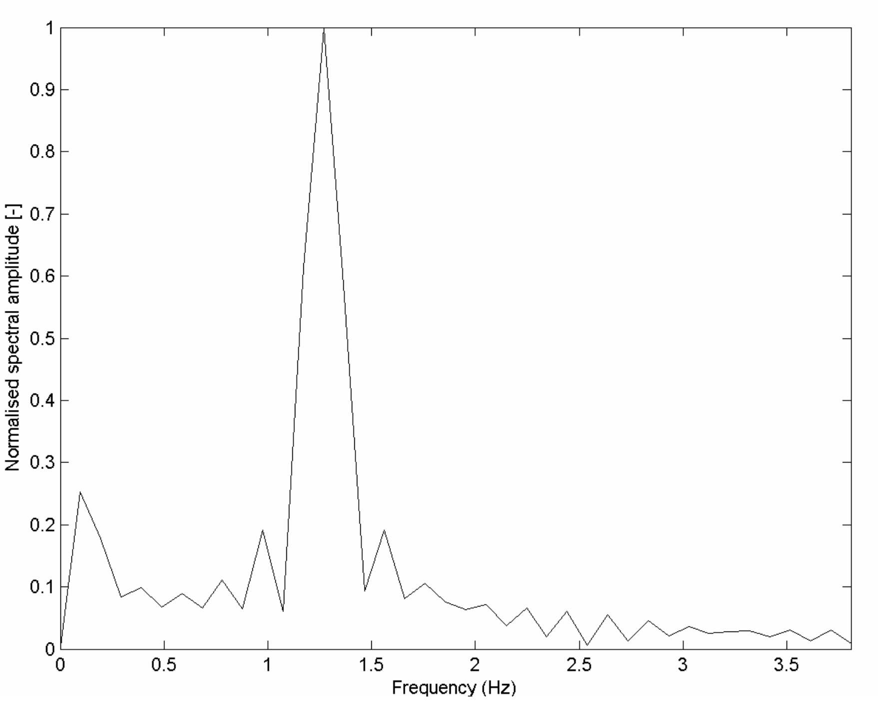

Figure 5: Fourier spectrum of the moment coefficient for the bridge deck exposed to an incoming wind of 20 m/s.

3.2.4. AERODYNAMIC INSTABILITY

Flutter and galloping both occur for wind which does not act in resonance with the structure, both described as aerodynamic instability phenomena. In addition, the phenomena are independent on the turbulence of the incoming wind, but can arise in a uniform flow. Galloping is the phenomenon occurring when the structural vibrations are almost perpendicular to the incoming wind and is characterized by negative aerodynamic damping as the driving force. A principal sketch of the flow and forces introduced on a cross section is showed in Figure 6.

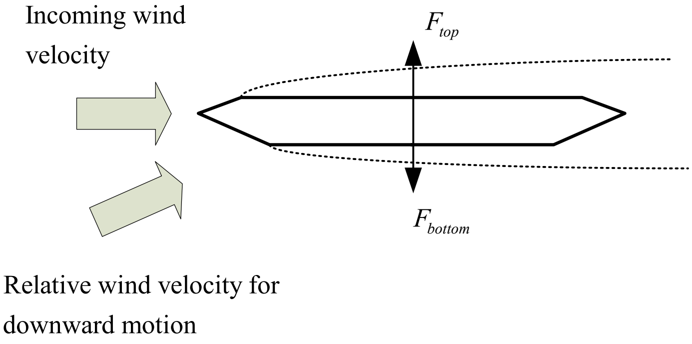

Figure 6: Principal sketch of galloping for a bridge deck. Galloping occurs when $F_{bottom} > F_{top}$.

Due to the downward motion of the bridge deck, the streamline on the bottom-side of the bridge deck flows closer to the boundary than the streamline on the top-side, as shown on the figure above. This result in an increase in the velocity on the bottom-side, which will decrease the static pressure, relative to the top-side, cf. Bernoulli's equation, hereby introducing negative aerodynamic damping. This may result in a wind-induced force, working parallel with the motion.

The remaining phenomenon to be described is flutter, which is the focus area of this report. Flutter is a combination of a coupled vertical motion and a rotational motion. A principal sketch of the phenomenon is seen in Figure 7, where it is assumed that a flutter vibration is fully developed.

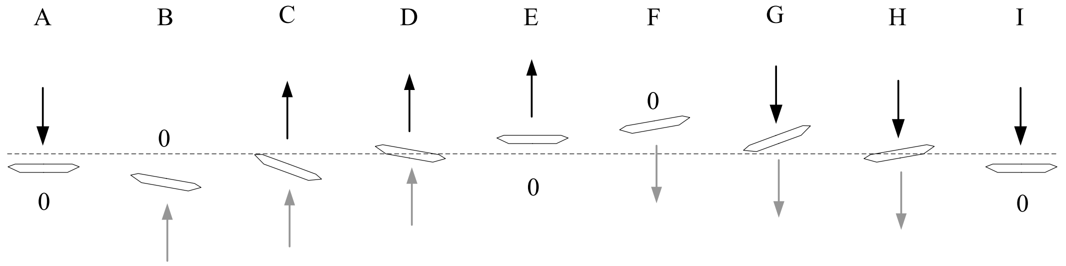

Figure 7: Flutter vibrations for a bridge deck. Black arrow indicating the movement of the deck, grey the vertical wind force. [Hansen and Dyrbye 1997]

It is important for the coupled flutter vibration, that there is a phase difference between the torsional and the vertical movement. If there is no phase difference between the two movements, the resulting work is zero. The coupled flutter vibration is shown in the figure above and described below in the following. The phase difference in Figure 7 is 45°.

- **A.** The bridge deck is moving down and the total force is zero. The work done in this stage is zero.
- **B.** The force on the bridge deck is positive and the vertical velocity is zero. The work done in this stage is zero. The moment is also working in the same direction as the rotation.
- **C.** The stored elastic strain energy now forces a vertical movement, enhanced by a vertical wind force. The total work in this stage is positive.
- **D.** As C.
- **E.** As A with a reversed velocity

The stages from E to H are similar to those from A to D, only symmetric around the axis of zero vertical displacement. The wind forces shown in Figure 7 are schematic, and may vary a little for different cross sections. As an example, the wind force in stage A is found to be slightly positive for the Great Belt Bridge, as shown later in this report. Flutter is said to occur when the energy input, from the wind velocity, is equal to the energy dissipated. This velocity is known as *the critical flutter wind velocity*. The aerodynamic damping loads become negative when exceeding the critical flutter wind velocity, and thereby further increasing the vibration amplitudes.

For flutter to occur, the torsional frequency must exceed the vertical frequency for the bridge movements, but only marginally. This ensures the continued energy transfer to the system which is crucial for the phenomenon to arise. Else the energy transfer will dissipate due to structural damping. [Hansen and Dyrbye 1997]

The definition sketch for the treatment of flutter is seen on Figure 8 .

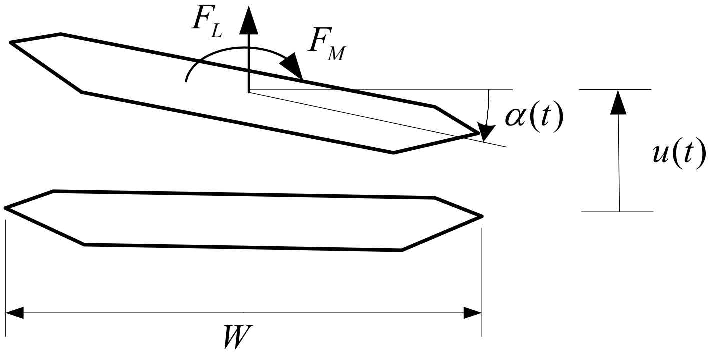

Figure 8: Definition sketch for flutter. F_L and F_M are the lift and moment respectively. u and a are the vertical and rotational motion respectively.

3.3. GOVERNING EQUATIONS FOR THE FLUTTER PHENOMENON

The wind-induced forces on a bridge deck have been briefly explained in the previous section. By use of this, a derivation of the formula, with which the aeroelastic forces, in the case of flutter, can be described. This is used to determine the aerodynamic derivatives and thereby the critical values for the wind velocity for a given bridge deck. Since the phenomenon, beside the aerodynamic forces, is dependent on inertia and elasticity it is rational to use the equation of motion as the governing equation. Both a vertical and rotational motion is included in the phenomenon. The full derivation can be seen in appendix A.

$$\begin{aligned} m\ddot{x} + c\dot{x} + kx &= F(t) \\ I\ddot{\alpha} + c_{\alpha}\dot{\alpha} + k_{\alpha}\alpha &= M(t) \end{aligned} \tag{3.3}$$

where

m, I	is the mass or mass moment of the system respectively
c	is the damping of the system
k	is the stiffness of the structure
x, α	is the vertical or rotational displacement respectively
F(t), M(t)	is the lift- or moment force respectively

[Nielsen 2004]

The dot denotes the number of differentiations with respect to time, thereby describing the acceleration and velocity. In the following, the procedure is only described for the vertical motion. Description of (3.3) are now done by use of the aerodynamic derivatives introduced by [Scanlan 1978]. In its original form, 18 derivatives are introduced. There are three load terms, described by three velocity and three deflection terms. The terms containing the accelerations are considered negligible, since a heavy structure as a bridge, only is exposed to small accelerations. Furthermore, the derivatives describing the vertical displacement are considered to be of minor importance. [Scanlan 1978]

$$\begin{aligned} m\left(\ddot{u} + 2\zeta_{u}\omega_{0,u}\dot{u} + \omega_{0,u}^{2}u\right) &= \frac{1}{2}\rho U^{2}W\left(KH_{1}^{*}\left(K\right)\frac{\dot{u}}{U} + KH_{2}^{*}\left(K\right)\frac{W\dot{\alpha}}{U} + K^{2}H_{3}^{*}\left(K\right)\alpha\right) \\ I\left(\ddot{\alpha} + 2\zeta_{\alpha}\omega_{0,\alpha}\dot{\alpha} + \omega_{0,\alpha}^{2}\alpha\right) &= \frac{1}{2}\rho U^{2}W^{2}\left(KA_{1}^{*}\left(K\right)\frac{\dot{u}}{U} + KA_{2}^{*}\left(K\right)\frac{W\dot{\alpha}}{U} + K^{2}A_{3}^{*}\left(K\right)\alpha\right) \end{aligned} \tag{3.4}$$

The time dependent force in (3.3) is described in more detail in the previous chapter, and is denoted in (3.1). By use of the assumptions of the expected flows, as described in section 3.2, the force *F(t)* is expanded.

$$F(t) = F_{m} + F_{t}(t) + F_{ae}(t) + F_{ae,b}(t) \tag{3.5}$$

where

$F_{ae,b}$	is the aeroelastic forces related to buffeting

The force described in (3.5) is considered as containing all the load contributions on a bridge deck.

Considering the forces in (3.5), the turbulence contribution to the total force, *F(t)*, is disregarded. By this assuming that the contribution to the aerodynamic forces from buffeting and vortex shedding is negligible. An argument for this is that buffeting results in a random response, which can be considered to prevent the occurrence of single-mode flutter. Furthermore, the wind field around bridge decks, often seen high above water, is seen to have low turbulence intensity. For multi-mode cases, a similar assumption can not be made, where the random forces is capable of contributing to higher frequency modes. It must be noted that buffeting can be included in the investigation, by finding the aeroelastic contributions from the turbulence in the incoming wind. This is an ongoing research field and is not investigated further in this report. Another effect that is disregarded is vortex shedding, which is possible to simulate, as shown in appendix B, by using a fine mesh in the flow simulation, and by controlling y^+. This can be shown to be without influence on the flutter derivatives [Nielsen et al. 2008]. If the vortex shedding is to be implemented in the solution of the critical flutter wind velocity, the linear expression for the flutter condition cannot be used. A nonlinear approximation of the motion effects on the aerodynamic forces must be introduced to describe the cross-wind contributions. [Nielsen et al. 2007] [Vairo 2002] [Scanlan 1993] [Scanlan 1997] [Diana et al. 2006]

4. BASIC ASSUMPTIONS

4.1. INTRODUCTION

This chapter will describe the approach taken in treating the bridge deck simulations, and thereby finding the critical values. Furthermore, the chapter will emphasize the assumptions made, and the results of these.

4.2. STRUCTURAL BEHAVIOR OF THE GREAT BELT BRIDGE

As the aerodynamic derivatives are used in describing the motion-induced forces, knowledge of the bridge's structural behavior is essential, since the response of any structure are dependent on parameters such as mass, stiffness, form of deflection and the natural frequencies, as described in the governing equations in the previous chapter. The main structural components of a long suspension bridge can be seen on Figure 9.

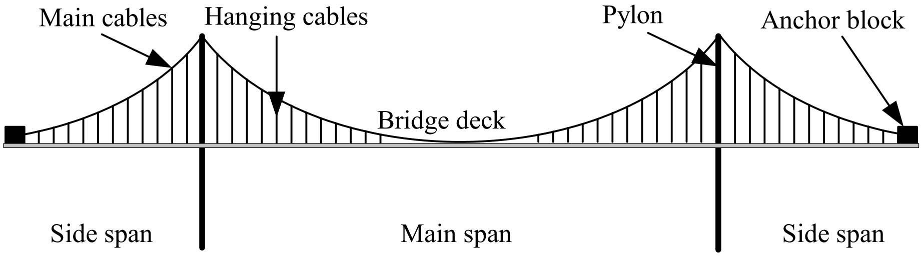

Figure 9: Main structural components of a long suspension bridge.

As seen in the previous chapter, the bridge is simplified to a simple 2-dof system. By doing this, it is important to include all the vibrating masses from the entire construction. The response of the section model is not just described by considering the small section, but must be done by taking the whole bridge into account, including deck, cables and pylons. For example, the vibrating cables are of major importance to the modal masses. Furthermore, the modal load must also be introduced, but when considering a small mid section for the lowest symmetrical modes, where the value of the mode shapes are close to one, the modal size of the load are of smaller importance.

Besides the modal mass and load, a precise description of the natural frequencies of the bridge is essential in determining the correct critical wind velocities for flutter, since the relation between the vertical and torsional frequency are of great importance to the energy transfer essential for the phenomenon.

This report focuses on flutter mode 1, and a multi-mode analysis is not performed. In flutter mode 1, only the lowest modes are relevant. As mentioned previously, the problem is solved by use of the aerodynamic derivatives, where the drag components are removed. It is noted, that for suspensions bridges with spans above 1 km, the horizontal deflections becomes significant, and should be included in the investigation [Hansen and Dyrbye 1997]. In this report, only the vertical and torsional modes are considered. The simplest lowest modes are that of the 1. symmetrical and 1. asymmetrical mode for both vertical and torsional movements. The modes are seen on Figure 10.

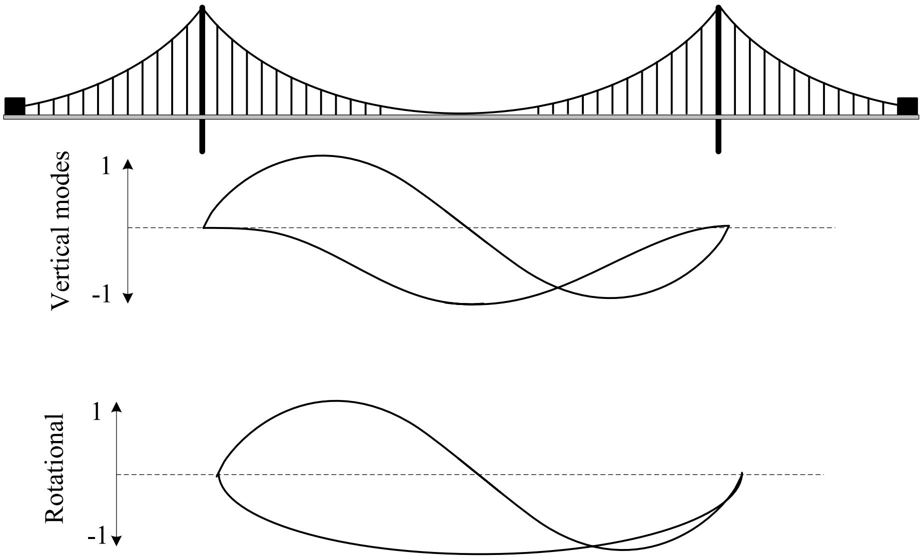

Figure 10: The lowest vertical and torsional modes for the bridge. Free interpretation after [Hansen 1996]

As mentioned in appendix A, the coupling between the vertical and torsional modes is of importance. Coupling between symmetrical modes are more likely to occur when these have their largest deflections at the same part of the bridge deck, and symmetrical modes are not likely to couple with asymmetrical modes. For example, by considering Figure 10, the lowest symmetrical vertical mode, will have its largest deflections, where the first asymmetrical torsional mode have its smallest vibrations. The coupling coefficient between the two lowest asymmetric modes shown in the figure is found to 0.79, and the mode coupling coefficients in flutter mode 1 are close to one. [Hansen 1996] [Hansen and Dyrbye 1997]

4.2.1. STRUCTURAL ASSUMPTIONS

As mentioned in the introduction of this report, the bridge is treated at two different stages: during construction and when fully erected. The numerical simulations utilize the symmetry conditions around the centre of the bridge. When analyzing the bridge during construction, the numerical model moves as a rigid body. This has been done to reproduce the results found by the section model tests in the wind tunnel. To ensure that the right input parameters are used and to interpret the results in the correct way, it is here described which parameters are used in both the 2d and 3d case, and how the wind load is treated.

2-dimensional bridge section

To calculate the critical flutter wind velocity for the fully erected bridge, a mid section is considered. The calculated critical velocity is therefore the value at which this section goes into flutter. As seen in Figure 10, the deflections for the symmetrical modes, used in flutter mode 1, has its maxima at the middle of the bridge deck, and is therefore exposed to the largest motion-induced wind loads. The parameters used in the calculation are found as the modal mass for the completed bridge. As mentioned earlier, it is essential that the modal mass is introduced, to ensure that the energy dissipation, from the movements of vibrating cables and other structural components of the bridge, is found correctly. Furthermore, to use the formula, described in appendix A, the generalized wind load must also be found. The modal load is assumed to be close to identical to the measured wind load, based on the assumption made earlier, that the mode shape has a value close to one in the mid section considered. Using the measured value of the wind load directly is therefore assumed to be a good approximation. The results of the modal analysis of the fully erected bridge, used in the calculation of the critical flutter wind velocity, are seen in Table 1.

Table 1: Constants used in determining the critical flutter wind velocity and the flutter frequency for the completed bridge. [Hansen 1997] [Hansen 1996]

Modal mass per unit length [kg/m]	19.562
Modal mass moment of inertia [kgm^2/m]	2.342.626
Natural vertical frequency [Hz]	0.0985
Natural rotational frequency [Hz]	0.2549
Width of the deck [m]	31
Density of air [kg/m^3]	1.185
Structural vertical damping ratio	0.01
Structural rotational damping ratio	0.01

The damping ratio used includes structural damping and the aerodynamic damping from the aerodynamic forces on the cables. [Hansen 1996]

The section is treated as a rigid body in the simulation, thereby not considering the deflection of the bridge deck itself. The deflection is considered small compared to the much larger vibrations of the bridge, and therefore assumed to have only a small effect on the motion-induced wind loads.

3-dimensional bridge section

The 3-dimensional case is the bridge during construction. Two methods can be used in erecting the bridge. Transport limitations normally dictate the length of the bridge deck sections, so the major difference is found in the starting point of the erection. From a structural point of view, only two starting points are relevant to use, to ensure a symmetric load distribution. The two starting points are illustrated on the figure below.

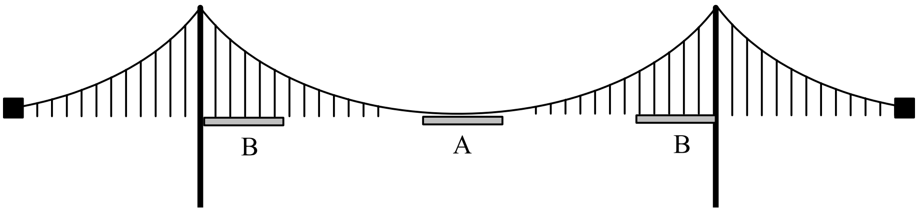

Figure 11: Erection starting points.

As seen on the figure the two starting points are A: starting from midspan, and B: starting from the two pylons. Start point A relies on the increase in rotational stiffness from the cables. In general, the stiffness of the structure in the early erection phases can be solely ascribed to the cables, since the stiffness of the bridge deck is relatively small. The separation of the lowest vertical and torsional frequencies is important to the developing of flutter. The separation is expressed by the frequency ratio, γ_ω, As described in appendix A, a large frequency separation will lead to a large critical flutter wind velocity, since the energy transfer in the coupled flutter mode is dependent on the energy transfer between the vertical and torsional mode. This transfer is at its highest when the torsional frequency is only slightly larger than the vertical. Based on this, it must be concluded that a large frequency separation in the erection sequence is desired.

For case A, the stiffness of the dynamic system is mainly originating from the cables which contribute a great deal to the modal mass. The vertical frequency of a bridge deck erected from the middle can be seen to be close to constant, due to a proportional increase in both mass and stiffness. The relation between the mass moment of inertia and the rotational stiffness will increase, thereby resulting in an increasing natural rotational frequency. This is illustrated on Figure 12.

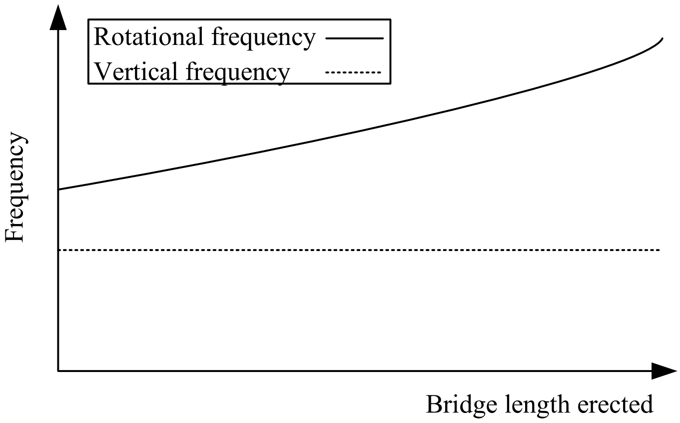

Figure 12: Principal sketch of the rotational and vertical frequency as a function of the erected length. [Hansen and Dyrbye 1997]

The frequency separation, seen in the figure, is the reason for the increasing critical flutter wind velocity for a longer bridge deck. This is not investigated further in this report, but can be seen in [Hansen 1996].

For case B, the torsional stiffness is ensured by the pylon, on which the bridge deck is supported. The deck does not rest on the pylon, but is mounted by use of brackets providing a rotational support [Thorbek 2008]. When extending the bridge deck towards the midspan, the rotational stiffness of the bridge deck will decrease, proportional to the length, thereby reducing the critical flutter wind velocity, as a result of the frequency separation decreasing. Often, the critical flutter wind velocity found for this case, is smaller than the one found for case A. In general, the most important difference between A and B, is that the modes considered for case A, will result in the wind load being converted to kinetic energy in vibrating cables to a larger extend then in case B. This has a stabilizing effect. Considering the cables are therefore of great importance when considering flutter in large suspension bridges.

Sometimes a combination of the two erection sequence strategies is used. A great advantage in this case, is that the bridge deck mounted in the cables around the pylons will increase the mass of the dynamic system, and thereby increasing the modal mass of the bridge deck mounted in the midspan, considering that this is dependent on the induced wind load being converted into kinetic energy of the cables, as mentioned previously. This will lead to a higher rotational frequency, resulting in a higher frequency separation. This report focuses on erection method A which was used when erecting the Great Belt East Bridge.

The mode shapes for the 3-dimensional case are, since the bridge deck has yet to be erected, dominated by the main cable movements. Approximating it by the two lowest symmetrical modes, as seen on Figure 10, is a possibility, but [Hansen and Dyrbye 1997] has calculated the cable movements for when 20 % of the bridge deck is erected. The movements of the main cables can be seen in Figure 13.

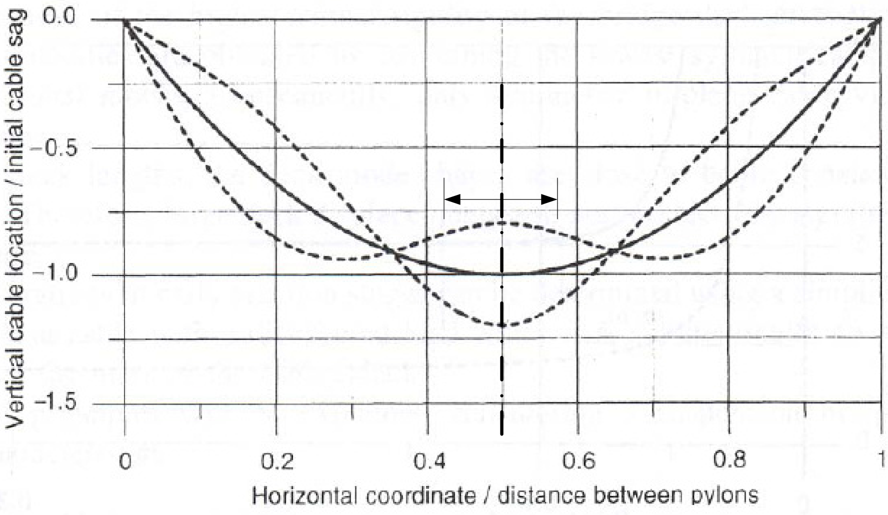

Figure 13: The movements of the main cables in the main span for the lowest relevant symmetrical mode shapes for both vertical and torsional movements. The solid line illustrates the neutral position. The length of the critical bridge length is marked [Hansen and Dyrbye 1997]

As mentioned in the beginning of the report, an erected length of bridge deck of 249 meters is critical, resulting in the lowest critical flutter wind velocity. The bridge deck length is marked on Figure 13. The Great Belt Bridge was erected, by hoisting a 57 meter long center section up, and thereafter mounting 48 meter sections on each side, one at the time. The 249 meter long bridge deck can then be illustrated as shown on Figure 14. [Thorbek 2008]

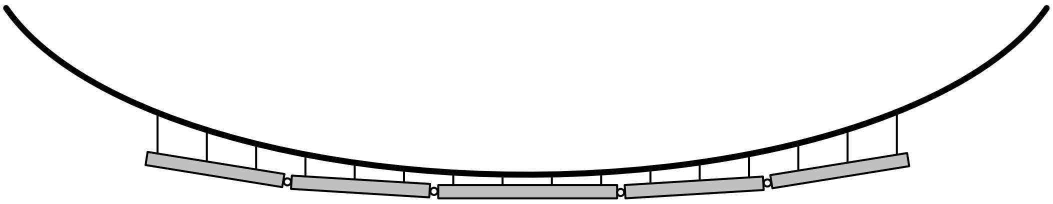

Figure 14: Principal sketch of 249 meters of erected bridge deck.

A picture of the Great Belt Bridge at this stage of erection can be seen on Figure 15.

Figure 15: Illustration of the Great Belt Bridge with 249 meters of erected bridge deck. [Frandsen 2003]

Is it assumed that the mode shape for a 20 % completed bridge, is almost similar to the case where 249 meters are completed, corresponding to approximately 15 %. By considering Figure 13, the variation of the mode shape, in the interval considered, a rather small, thereby minimizing the error made by treating this as a section with constant mode shape. Still, it is of critical importance to separate modal and actual masses in the calculations, as these are critical to the determination of the correct critical flutter wind velocity. By use of the same assumptions as for the 2-dimensional case, the modal load is assumed close to the measured wind load. The mid section will deflect, as seen in principal on Figure 14, but the magnitude of this deflection is considered small compared to the much larger bridge vibrations. The section is therefore treated as a rigid body.

The results of the modal analysis are seen in Table 2.

Table 2: Constants used in determining the critical flutter wind velocity and the flutter frequency for a bridge under erection. [Hansen 1996]

Modal mass per unit length [kg/m]	33.400
Modal mass moment of inertia [kgm^2/m]	6.724.000
Natural vertical frequency [Hz]	0.109
Natural rotational frequency [Hz]	0.135
Width of the deck [m]	31
Density of air [kg/m^3]	1.185
Structural vertical damping ratio	0.01
Structural rotational damping ratio	0.01

5. EVALUATION OF THE 2D-SIMULATION RESULTS

5.1. INTRODUCTION

This section describes the procedure for determining the aerodynamic derivatives and the critical flutter wind velocity. The results are compared to wind tunnel measurements. The procedure is based on the forced oscillation technique. By use of the simulation described appendix B, it is possible to find the aerodynamic forces on the bridge deck caused by the motion-induced forces. This is explained in section 3.3. The simulation is performed by use of Ansys CFX, using a SST turbulence model, with 20.954 nodes and 15.168 elements. The general equations behind this program are described in appendix C.

The dimensionless time step, defined in (5.1), is equal to $\Delta t^* = 0.05$ for all simulations. The turbulent kinetic energy and the specific dissipation rate, as mentioned in appendix C, is defined so that the kinematic eddy viscosity is of the magnitude $\nu_T \sim 10^{-12}$. This is done to ensure that the Reynold's number, Re, defined in (5.1), is primarily dependent on the molecular kinematic viscosity, ν, which ensures the desired turbulent flow.

$$\mathrm{Re} = \frac{UL}{\nu + \nu_T}$$

$$\Delta t^* = \frac{\Delta t U}{W} \tag{5.1}$$

where

L is a characteristic length

5.2. THE FORCED OSCILLATION OF THE BRIDGE DECK

The amplitudes of the rotational and vertical motion are chosen as 2 meters and 5° and 10° for translation and rotation respectively. The motion is harmonic as shown in Figure 16. The rotation is defined as positive clockwise and the translation is positive upwards as shown in Figure 16.

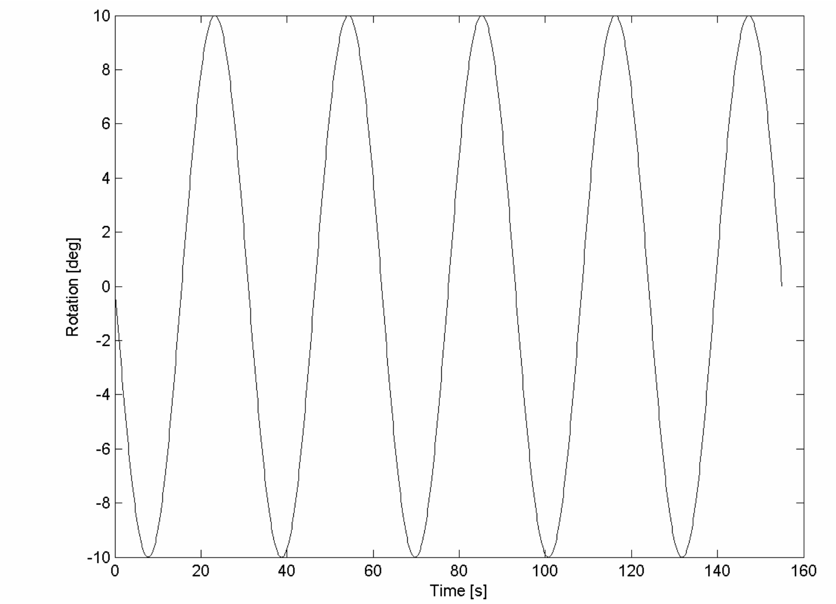

Figure 16: Harmonically varying rotation, with amplitude of 10°. T=31 s. as used in one of the simulations.

5.3. LIFT AND MOMENT ON THE BRIDGE DECK

As explained in section 3.2.4, the vertical and rotational motions induce a load on the structure. By integrating the pressure and wall shear forces, the total load on the structure can be calculated. The force is expected to be harmonic with the same frequency as the motion, but with a phase shift. For a section of length 1 meter the lift and moment forces for a rotational movement can be found to the values shown on the figures below. The rotation starts from rest and moves anti clockwise. The mean velocity in the simulation is chosen as $10\,\frac{\mathrm{m}}{\mathrm{s}}$. This leads to a reduced velocity of 10, defined by

$$U_r = \frac{2\pi U}{\omega W} \tag{5.2}$$

where

U_r	is the reduced velocity $\left[\frac{\mathrm{m}}{\mathrm{s}}\right]$
ω	is the circular frequency of the motion [s^{-1}]
W	is the width of the bridge [m]

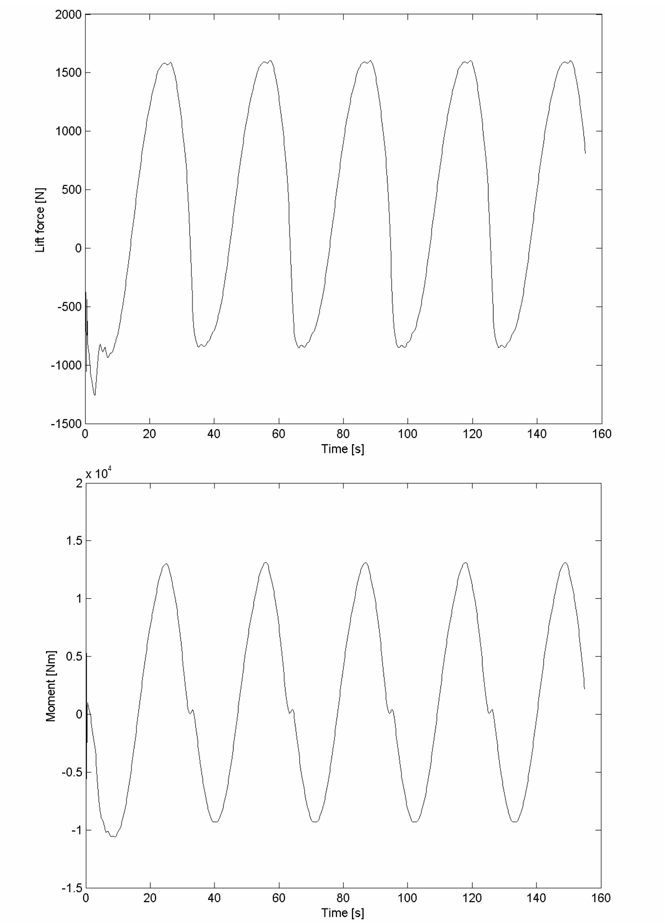

Figure 17: Lift and moment forces for the bridge deck.

The lift and moment coefficients for the rotation, seen in Figure 16, are shown on Figure 18.

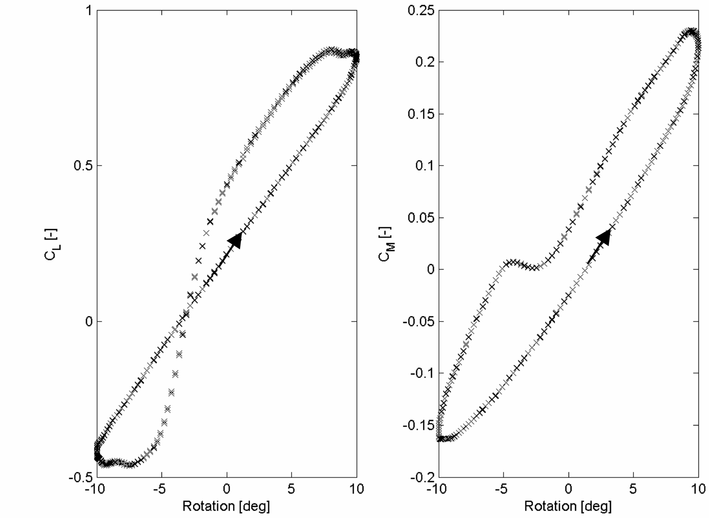

Figure 18: Lift and moment coefficient for a moving deck. The motion pattern is described by the arrows. The curvature of the path is discussed further in section 5.3.2.

5.3.1. STATIONARY FORCE COEFFICIENTS

The previously described load coefficients can be seen to be strongly dependent on the motion pattern. To investigate the difference from a stationary bridge, a calculation of the force coefficients are performed. This is done to avoid the effects from the motion. The lift coefficient for a stationary condition, when the deck is rotated 10 degrees anti-clockwise can be seen in Figure 19. The solution is stabilized after approximately 20 s. The

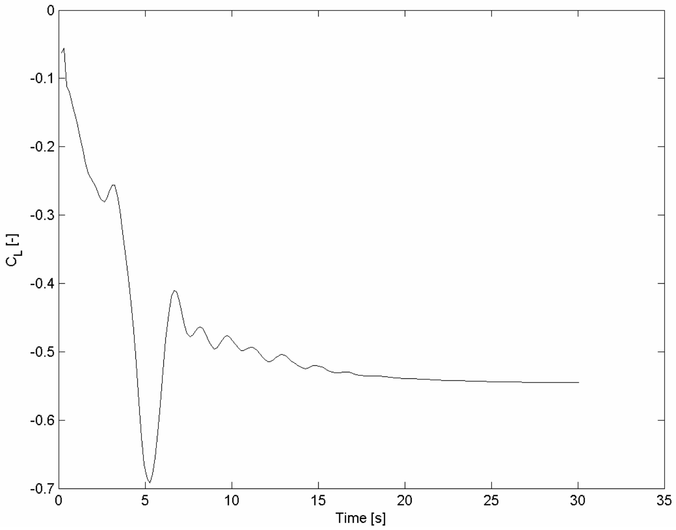

Figure 19: Stationary solution for the lift coefficient, when the bridge deck is rotated -10°.

By performing a series of stationary solutions, the following relationship between the force coefficients and the rotation can be found.

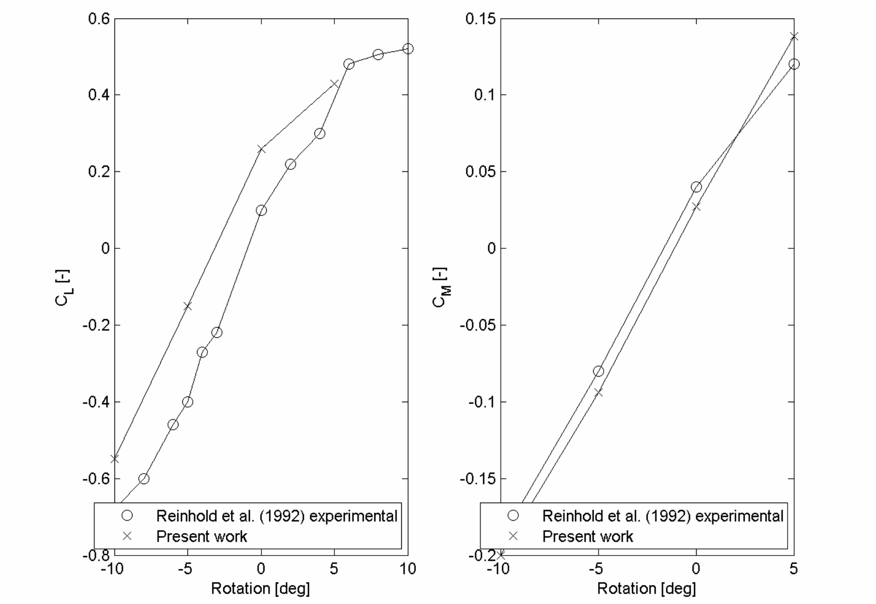

Figure 20: Stationary solutions for C_L and C_M.

It is seen that the used bridge deck geometry results in a rather high lift coefficient compared to Reinhold data and other sources [Morgenthal and McRobie 2000]. This can be partially ascribed to the mesh generation used in the 2d simulation, where only one element is used over the length of the section, thereby not allowing any flow in this direction, creating what can be best described, as an enhanced tunnel-flow around the element. A better estimation of the lift coefficients could be found by use of a large eddy simulation.

5.3.2. VARIATION OF LIFT AND MOMENT DUE TO SEPARATION

As seen in Figure 18, the variation in the load coefficient is significant, as expected due to the motion. However, a small deviation occurs around a rotation of -3°. This is seen to be caused by a sudden change in pressure, caused by a sudden change in the flow condition. The results of this can be seen on the moment force, around 62.5-65 seconds, as shown in Figure 21.

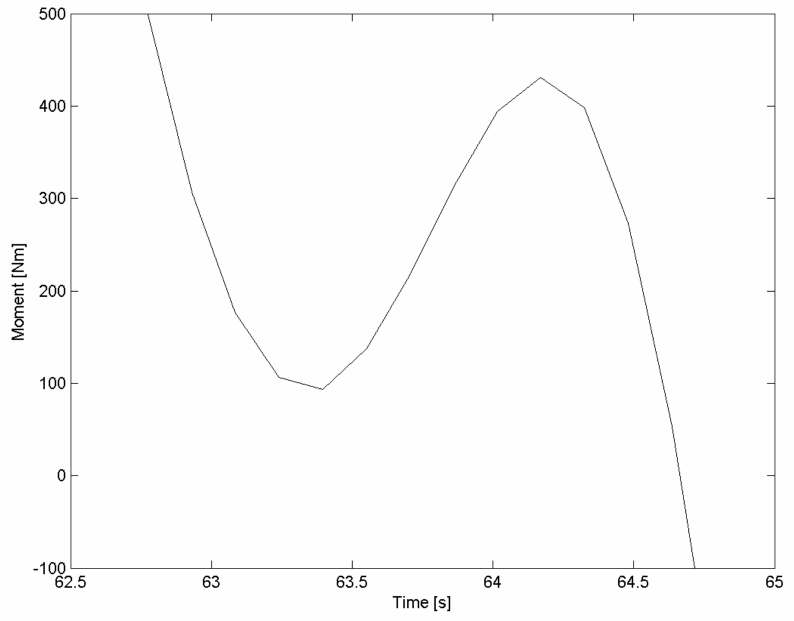

Figure 21: Detail of moment around 62.5-65 seconds.

To clarify the reason for this change, the pressure around this interval is investigated. A contour plot of the pressure for three time steps in this interval can be seen on Figure 22.

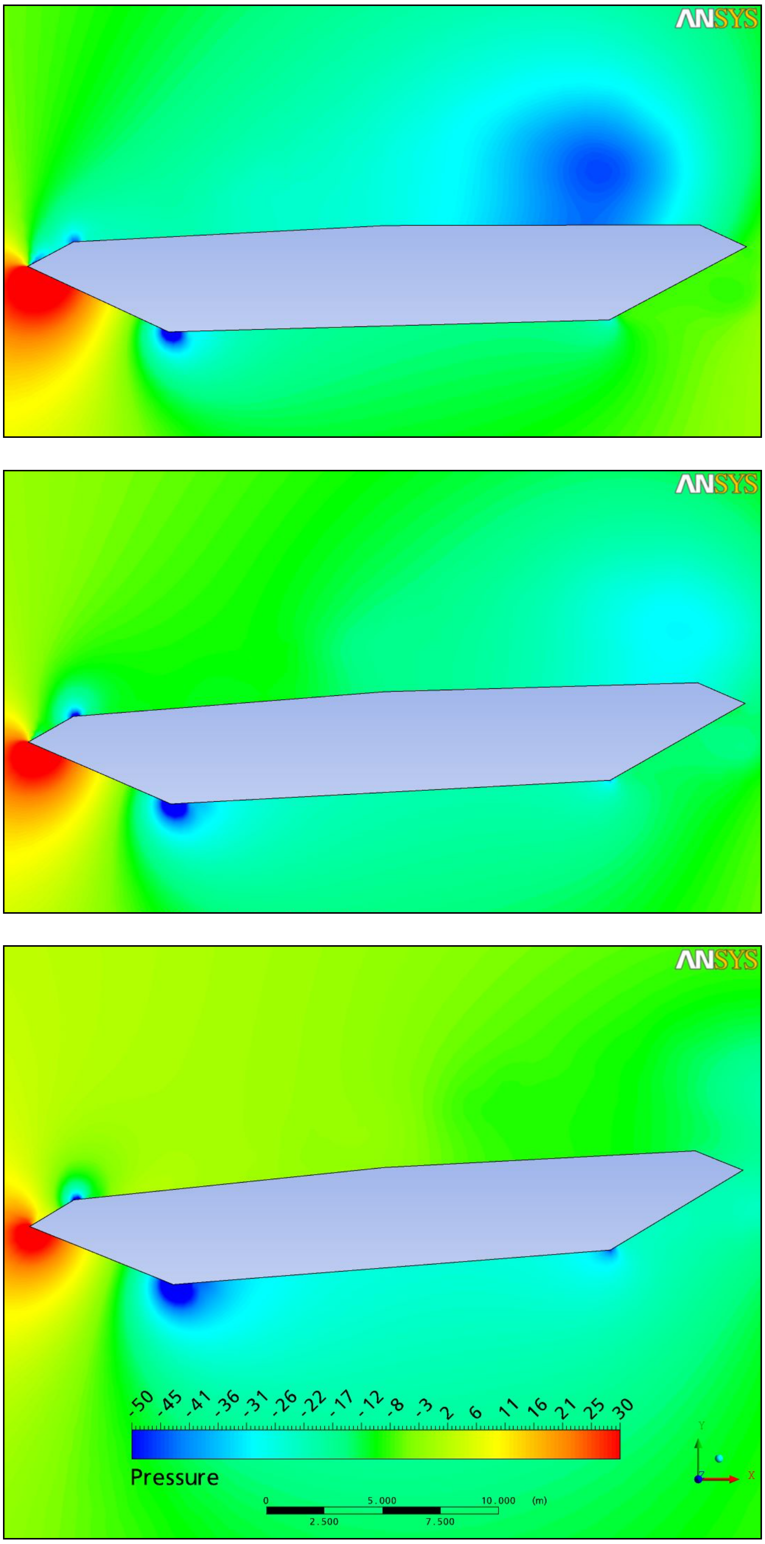

Figure 22: The pressure around the bridge deck in Pa, for time steps 62.775 s, 63.55 s and 64.325 s. A counter clockwise rotation of the bridge deck is ongoing.

The following remarks can be made of the pressure condition.

- A pressure, resulting in an upwards force, is acting on the leading edge of the deck. The pressure field is, even though it is decreasing, still positive in the three time steps.
- A vortex moving right along the top of the deck is resulting in a negative pressure. This is acting opposite the pressure at the leading edge.
- An almost evenly distributed negative pressure field is acting on the bottom of the bridge deck. The pressure field is increasing in size due to the counter clockwise rotation, but the contribution to the moment is considered to be rather limited.

By considering these three dominating effects on the bridge deck, the unexpected change in the moment, can be seen to be a result of the vortex moving right on the top of the deck. When this is shed from the deck, an increase in the (positive) moment is seen on Figure 21. A similar effect can be shown to be the reason for the change in lift.

5.4. AERODYNAMIC DERIVATIVES

The following sections will describe the calculation of the aerodynamic derivatives (AD´s), which are derived in appendix A. The center of attention is on the overall procedure, and not the specific results and use of the formulas, as this merely is a mathematical expression for the modal parameters. The formulas for the determination of the six Ads' are repeated in(5.3).

$$\begin{aligned}
H_1^* &= \mathrm{Im}\left(\frac{C_L W e^{-i\psi_L}}{K^2\tilde{u}}\right) & A_1^* &= \mathrm{Im}\left(\frac{C_M W e^{-i\psi_M}}{K^2\tilde{u}}\right) \\
H_2^* &= \mathrm{Im}\left(\frac{C_L e^{-i\psi_L}}{K^2\tilde{\alpha}}\right) & A_2^* &= \mathrm{Im}\left(\frac{C_M e^{-i\psi_M}}{K^2\tilde{\alpha}}\right) \\
H_3^* &= \mathrm{Re}\left(\frac{C_L e^{-i\psi_L}}{K^2\tilde{\alpha}}\right) & A_3^* &= \mathrm{Re}\left(\frac{C_M e^{-i\psi_M}}{K^2\tilde{\alpha}}\right)
\end{aligned} \qquad (5.3)$$

[Hansen and Dyrbye 1997]

5.4.1. PARAMETERS USED FOR DETERMINING THE AERODYNAMIC DERIVATIVES

As seen in appendix A derivations and the formulas above, the determination of the amplitude and phase of the load relative to the motion are the substantial parameters in the determination of AD's. Since the motion, for both rotation and translation, is fully known, the focus must be on the motion-induced wind load on the bridge deck, in search of the load coefficients, which act harmonically with the same frequency as the motion, and the phase difference between motion and load. This is done by use of a Fast Fourier Transformation analysis (FFT). To cut off the unstable data in the beginning of the time series, a period of the motion is removed. It is then possible to perform a FFT-analysis on the data in time domain, converting this to amplitudes in the frequency domain. The assumption for deriving the formulas above is that the motion-induced wind load has the same frequency as the motion itself. This can be verified, when looking at the frequency domain. The frequency domain for the lift coefficients for the case with a reduced velocity of 10 is shown for the load coefficients in Figure 23.

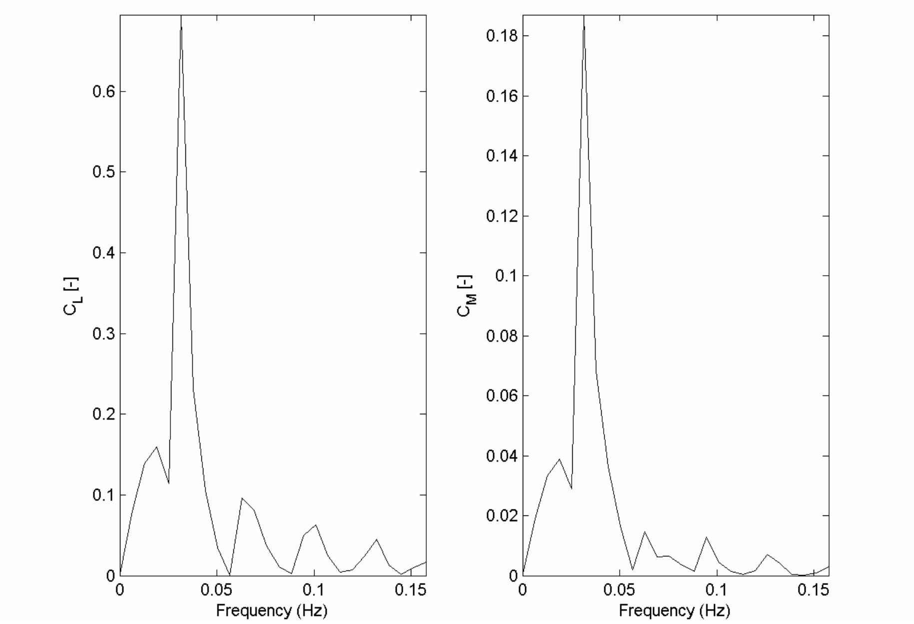

Figure 23: Frequency domains for lift and moment coefficients for a reduced velocity of 10.

As can be seen on the frequency domains two distinct load amplitudes are found at a frequency of 0.0315 Hz. This is the dominating motion-induced wind load. The frequency of the motion is found from a period of 31 s, to 0.0323 Hz. The small deviation between the motion and load frequency, less than 2.5 %, can be minimized by increasing the extent of the FFT-analysis, but with a corresponding increase in calculation time. For example by introducing a data filter. As the 2d-case is not the focus area of this report, as well as Fast Fourier Transformation, this is not investigated further. The number of FFT-points used in this analysis is chosen as the smallest power of two that is greater than or equal to the number of data points, since an FFT operation is more efficient when the sequence length is an exact power of two [Zill and Cullen 2001]. The pressure variations, due to phenomena as shown in Figure 22, can be seen in the frequency domain as small variations in the load coefficients, especially evident after 0.05 Hz.

By considering the formulas in (5.3), the last unknown is the phase shift ψ, which can be found with the time interval between the motion and the load as shown in Figure 24.

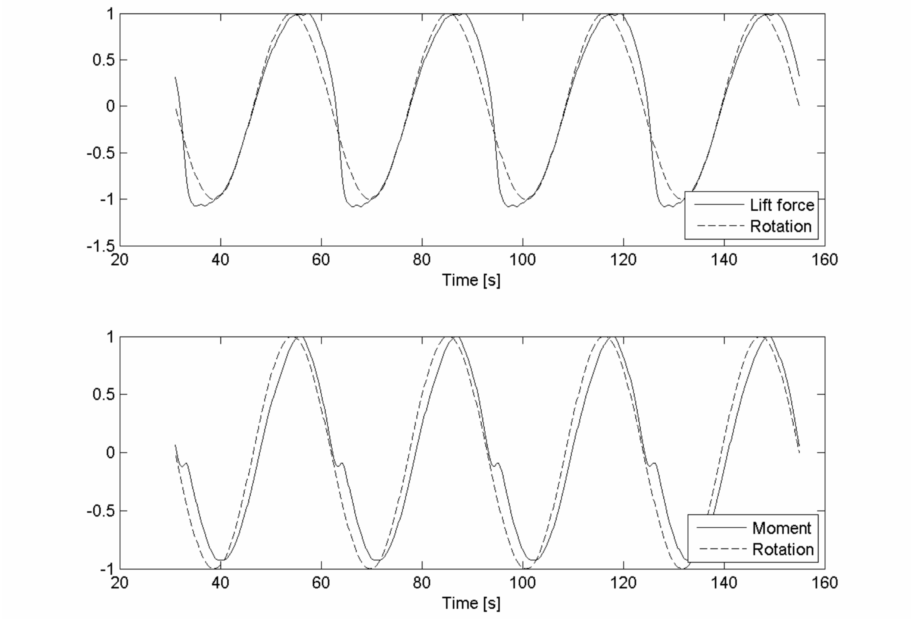

Figure 24: Normalized rotation, lift force and moment for illustration of the phase shift for the case with a reduced velocity of 10.

The motion and load are correlated as expected, as a positive rotation (clock wise) results in a positive moment and an upward lift, cf. the definition sketch in Figure 8. The phase shift is found by use of a zero down-crossing analysis. The time interval found in this particular case is approximately 1 s for the lift and 0.3 s for moment. The phase difference is converted from time interval to radians as

$$\psi = \frac{2\pi \cdot \Delta t}{T} \tag{5.4}$$

where

Δt is the time interval [s]

5.4.2. RESULTS

The previous section gave a short introduction on how to find the parameters used when determining the AD´s. This section will consider the AD´s calculated. The results are evaluated by comparison with wind tunnel tests. Since the focus of this report is not on the 2d case, it is chosen to centre the attention on considering which parameters, effects etc. are dominant in the calculations, so that the conclusion can be extended to the 3d case.

By evaluating the results it is evident that the needed parameters for different simulations, especially at high incoming wind velocities, become unstable, not necessarily wrong, when considering their usability in (5.3). This is described in detail later in this section. In general, two different principal simulations have been performed, when finding the AD's for different values of the reduced velocity defined in (5.5).

$$U_r = \frac{2\pi U}{\omega W} \tag{5.5}$$

The two variables in (5.5) are identified as the wind velocity, U, and the frequency of the motion, ω. Another parameter, which can be controlled, is the amplitude of the motion, as seen in (5.3). To different simulation types are performed by altering these variables:

- **Constant frequency of motion:** Control of the reduced velocity, U_r, is done by use of the velocity U. The amplitude of this case is ± 10 degrees for rotation and ± 2 meters for translation.

- **Constant velocity:** Control of the reduced velocity is done by use of the frequency of motion. The amplitude of this case is ± 5 degrees for rotation and not investigated for the case with vertical motion.

The reason why the amplitude of the rotation and velocity is lowered is due to unstable results, for the AD's, seen later in this section.

Aerodynamic derivatives found by use of a rotation

The AD's H_2, H_3, A_2 and A_3 are found by use of a rotational motion of the bridge deck. The results can be seen in Figure 25 to Figure 28. The unstable results, occurring at reduced velocities above 9, are easily seen in the figures. The reason for this is expected to be the high wind velocity and an extreme rotation of the deck, which is expected to create severe turbulent flow conditions around the leading edge of the bridge deck when this is rotated close to its maximum. This can be seen in Figure 18 where it is possible to see a change in the lift force around the maximum rotation, in a similar way that the moment changes around -3° which is explained in detail in section 5.3.2. By reducing the amplitude of the rotation, and using a lower constant velocity, thereby controlling the reduced velocity by use of the frequency of motion, the severe flow conditions are reduced, and the results are seen to stabilize, with a clear tendency. Further adjusting of the simulation for the 2d case is not the purpose of this report, and the reasonable results obtained are accepted. The calculated data is compared to the data from [Hansen 2008].

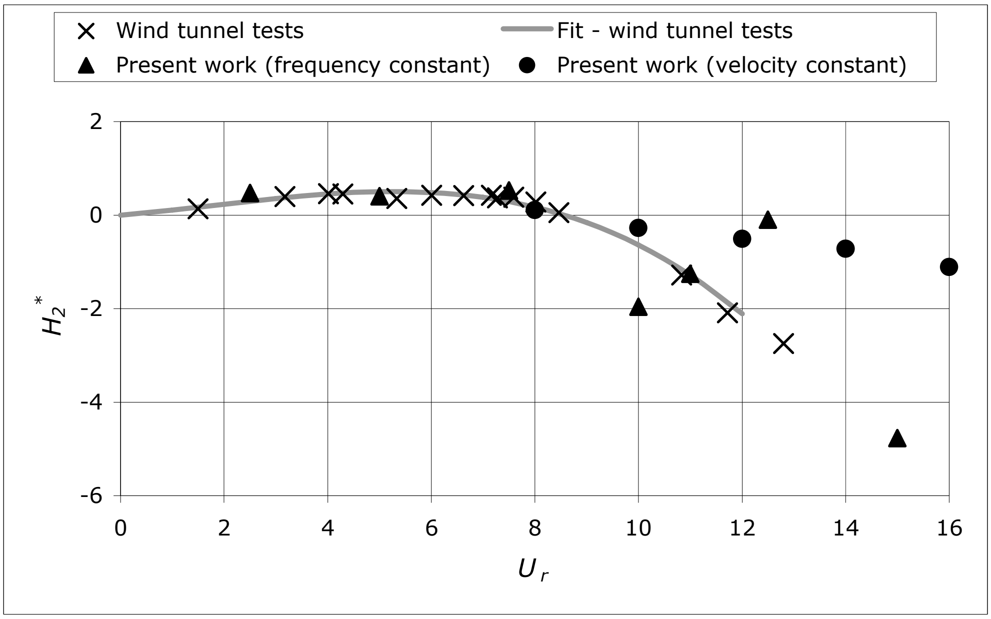

Figure 25: H_2 as function of the reduced velocity.

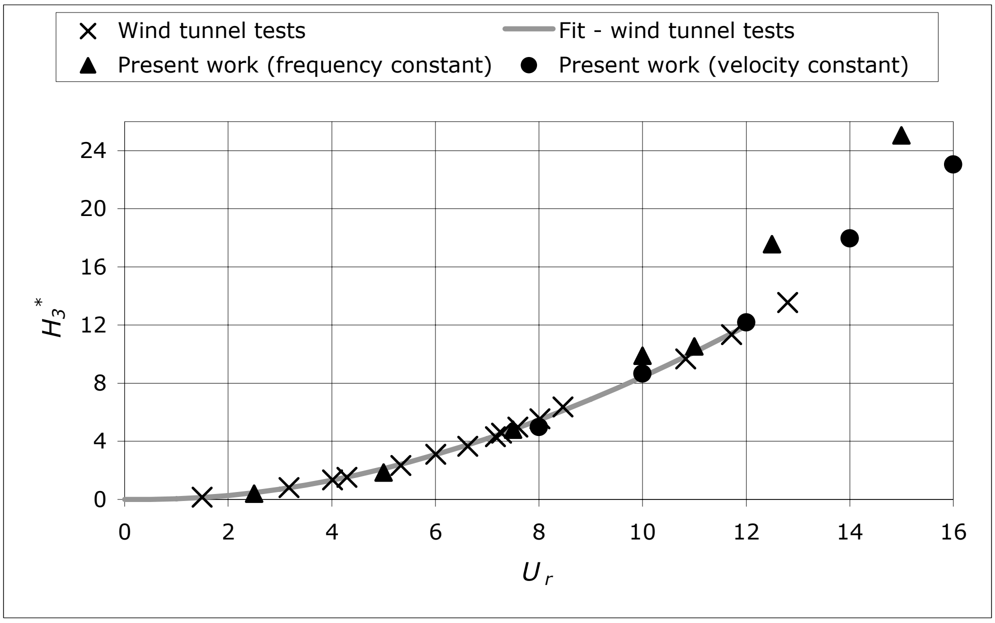

Figure 26: H3 as a function of the reduced velocity.

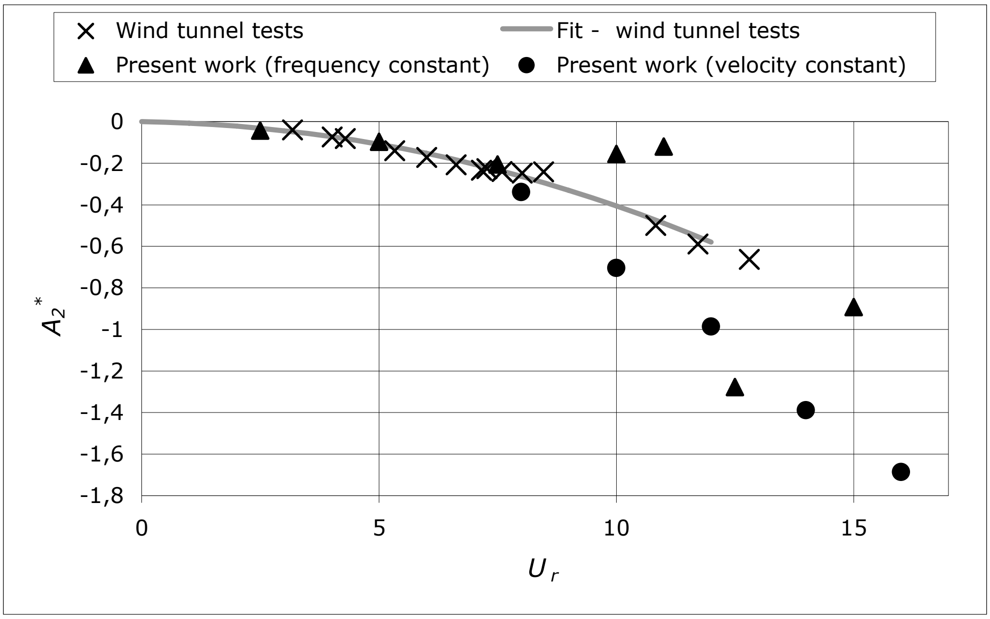

Figure 27: A2 as a function of the reduced velocity.

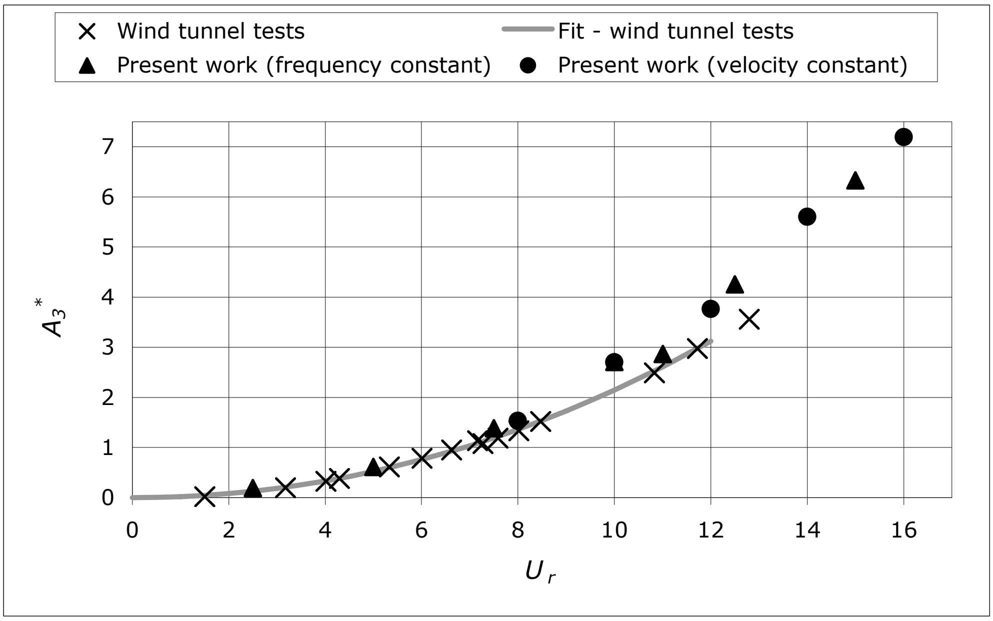

Figure 28: A3 as a function of the reduced velocity.

Aerodynamic derivatives found by use of a translation

The AD's for the translation are H_1 and A_1. The results are seen in Figure 29 and Figure 30. It can be seen that the results are stable with a clear tendency. This supports the conclusion made previously that the instability is caused by severe turbulent flow conditions around the leading edge of the bridge deck, which is more likely to occur when this has large rotational amplitude in a strong incoming wind.

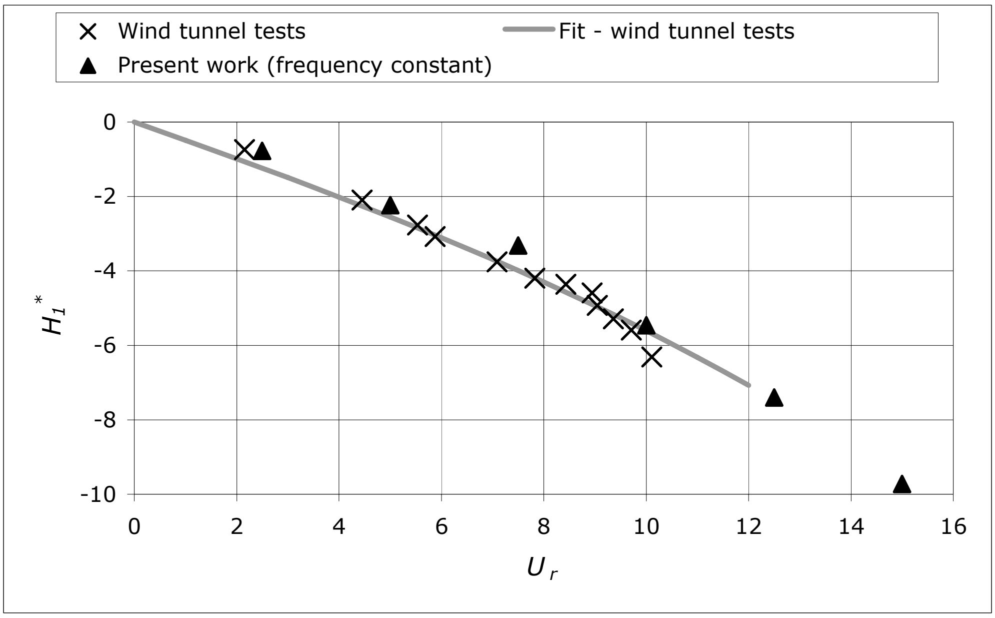

Figure 29: H_1 *as a function of the reduced velocity.*

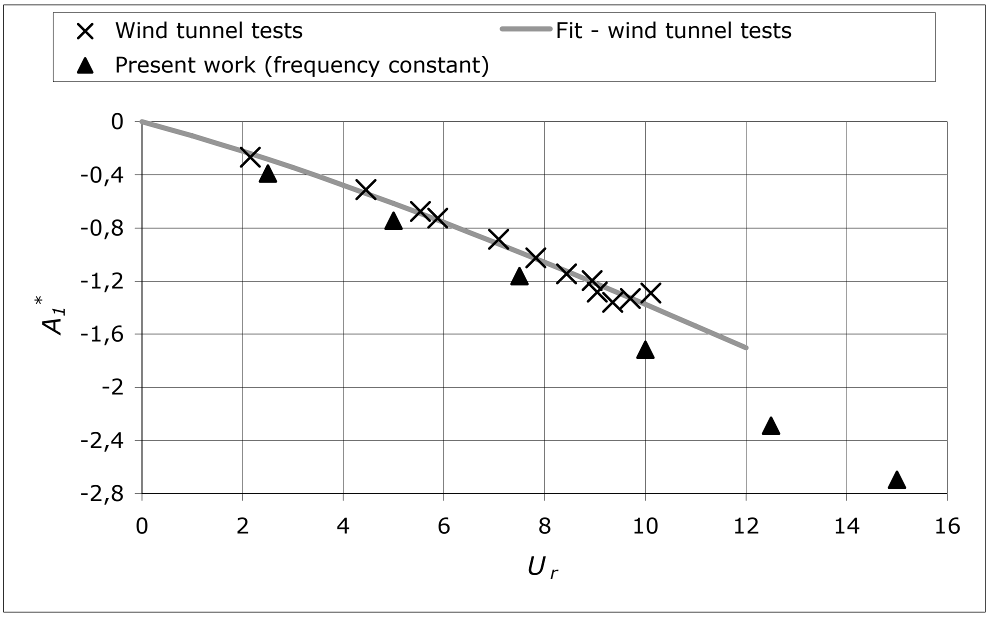

Figure 30: A_1 *as a function of the reduced velocity.*

Critical velocity and flutter frequency

The critical flutter wind velocity is found by use of the flutter condition, derived in appendix A. The condition describes a multivariate, non-linear system, which is to be solved for the flutter frequency, and the critical flutter wind velocity. As seen in appendix A, the AD's are dependent on the reduced frequency *K,* and thereby the reduced velocity U_r. To solve the system, it is chosen to fit the AD's to a function of U_r.

By use of a third order polynomial, and the least square method, the AD's are fitted as seen in the figures below. The data are only fitted in the simulated range, and is not extrapolated.

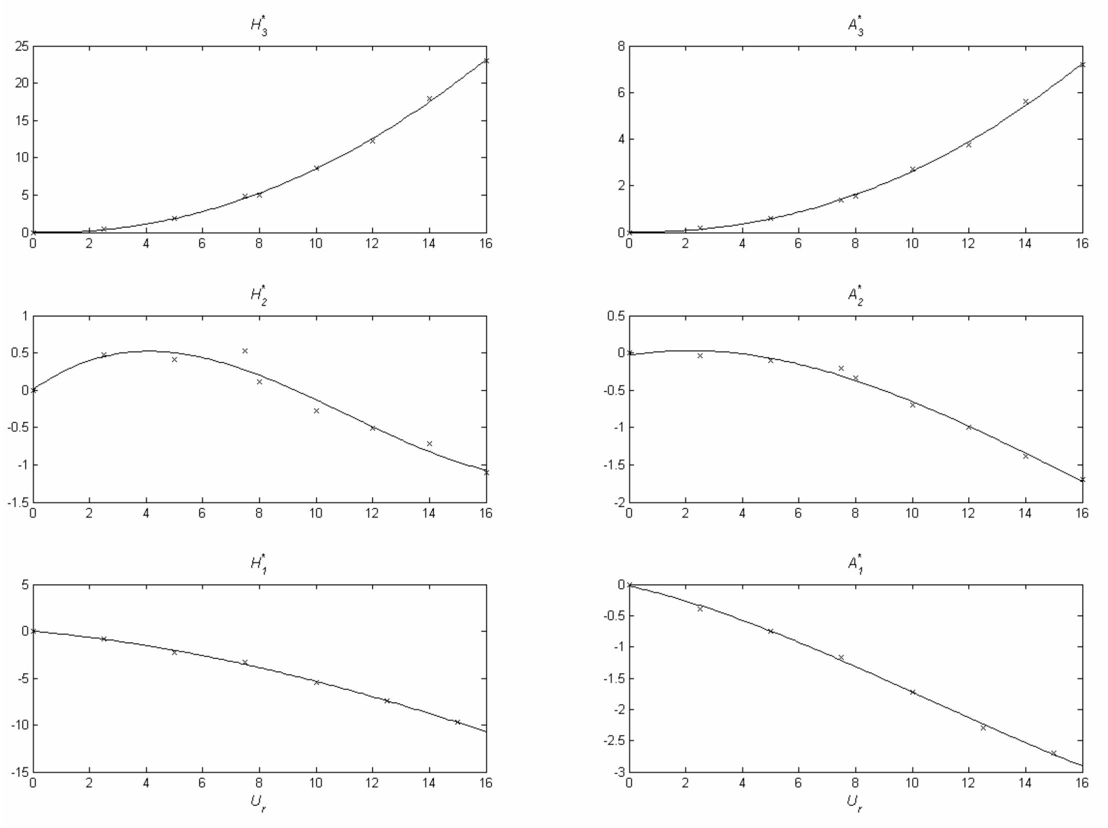

Figure 31: AD's fitted by use of a third-order polynomial.

The constants for solving the flutter condition are found by use of a modal analysis, by which the natural frequencies are determined. The values used are listed in Table 1 in section 4. By inserting the values in the flutter condition, and solving the system for when the imaginary part is equal to the real part, the solution can be illustrated as seen in Figure 32. The solution which gives the lowest value of the critical velocity is of interest. It is noted that the solution lies in the interval of the found AD's and no extrapolation is needed.

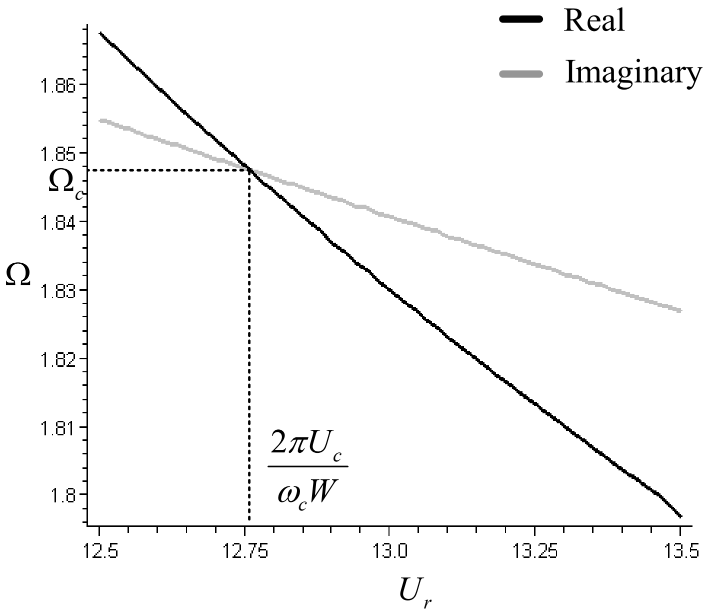

Figure 32: Illustration of the solution of the critical flutter wind velocity U_c, at the flutter frequency, found by Ω_c.

The intersection point in Figure 32, (U_c, Ω), is found to (12,752; 1,847). The critical velocity and the flutter frequency are then found by use of equation (5.6)

$$\frac{2\pi U_c}{\omega_u W} = \frac{2\pi U_c}{\omega_c W}\Omega_{cr} \tag{5.6}$$

[Hansen and Dyrbye 1997]

Table 3: Critical values for flutter from selected references.

Reference	Critical flutter wind velocity U_c [m/s]	Flutter frequency n_c [Hz]
Present work (two modes)	71,9	0,1819
[Nielsen et al 2007] (two modes)	68,8	0,1833
Wind tunnel tests [Reinhold et al. 1992]	70-74	N.A.
[Enevoldsen et al 1999] Multi-mode numerical	70-80	N.A.
[Frandsen 2003]	65-60	N.A.
[Awruch and Braun 2003]	73	N.A.

As seen in Table 3, the calculations show a good agreement, when compared to other references. It should be noted that railings, wind screens etc. on top of the deck not are simulated. This will decrease the critical flutter wind velocity. Considering a multi-mode vibration, the critical flutter wind velocity will increase, due to the increased energy dissipation from the added modes. [Frandsen 2003] [Nielsen et al. 2007]

6. EVALUATION OF THE 3D-SIMULATION RESULTS

6.1. INTRODUCTION

The three dimensional analysis is performed in two different ways. In section 6.3 an approach similar to the one used in the 2d-case is investigated. Aerodynamic derivatives are extracted from a forced vibration test, and the flutter equations are solved for the flutter frequency and the critical flutter velocity. The mesh of the domain consists of 97.683 elements and 30.374 nodes. This is described in appendix B mesh requirements.

In section 6.4, a set of dynamic equations are used to model the movements of the bridge when subject to wind loads. This is known as a fluid-structure interaction. This method requires the simulation of a long period of time, which is the reason why the domain is modeled very coarse. The domain consists of 20.217 elements and 4.431 nodes.

In both cases, a flow is allowed around the free end of the bridge, which results in changed wind loads. In general, two major differences are found from the 2d bridge section:

- End flow effect
- Change in modal mass and stiffness, and thereby the natural frequencies, dependent on the erection sequence strategies.

The erection sequence and the approach to solve for the aerodynamic derivatives are described in section 4.

6.2. END EFFECT

Besides the difference in how to treat mass and stiffness of a bridge during erection, compared to a finished bridge, there is also a change in flow. The flow is allowed to pass the ends of the bridge deck, thereby resulting in end effects. The end effect is also used when considering more typical structures as a freestanding wall, where a reduction in the lateral force coefficients can be seen, when taking the end effect into account. [EN 1991-1-4 2005] The end effect will result in smaller lift forces on the bridge deck, thereby increasing the critical flutter wind velocity.

The difference in pressure for a bridge deck with the end effect can be seen on the figure below, where a change in pressure can be seen around the end. The change can be seen for both pressure and suction. This is illustrated in Figure 34.

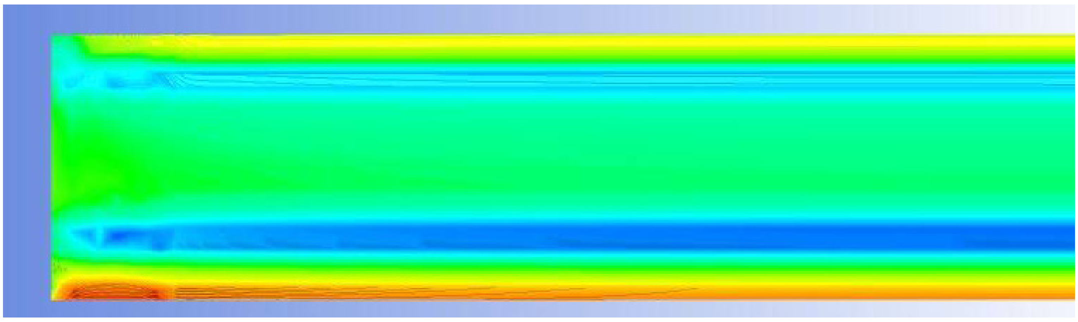

Figure 33: Illustration of the end effect on the bottom of the bridge deck, when the bridge is moving up.

To illustrate the change in the fluctuating part of the pressure, the bridge is considered in three different cases:

- The pressure on the inner part of the bridge, where no end effects are present
- The outer 15 meters of the bridge, where the end effect is dominating
- The two parts combined, which is the case used in the flutter calculations

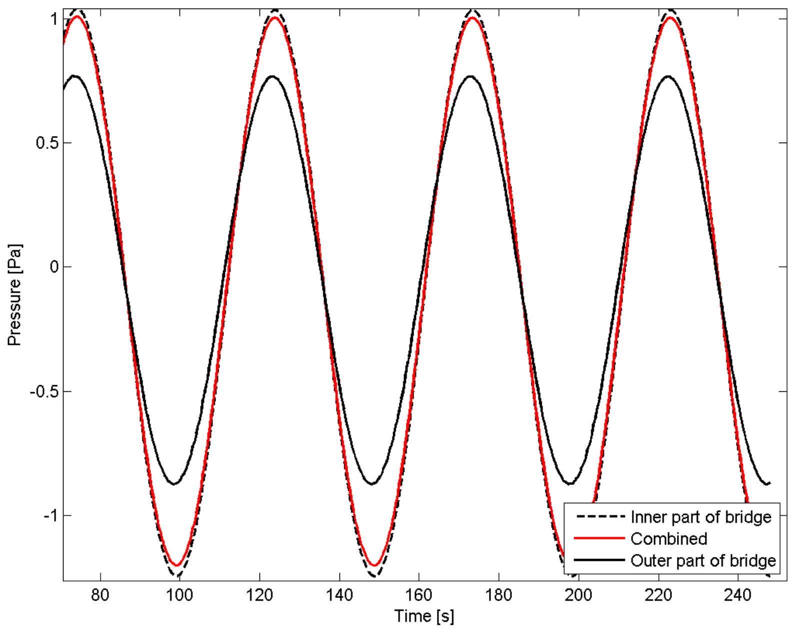

Figure 34: Fluctuating pressure for a translating bridge, calculated for three different cases.

As seen in the figure, the reduction in pressure and suction, when allowing flow around the free end of the bridge, is evident. The difference in lift force is dependent on the slenderness of the bridge, where a small slenderness ration will result in the largest pressure reductions. This is also the case for other structures, exposed to end flows. [EN 1991-1-4 2005]

6.3. RESULTS OF THE 3D FORCED VIBRATION TEST

As mentioned in section 4, the frequency separation is much smaller, compared to the 2d case, and this result in a much lower critical flutter wind velocity. The necessary values for calculating the critical flutter velocities are seen in Table 2 in section 4. The coupled flutter mode is found by use of the 1. symmetric vertical and rotational mode.

The solution of the flutter condition for the real and imaginary part is seen on Figure 35.

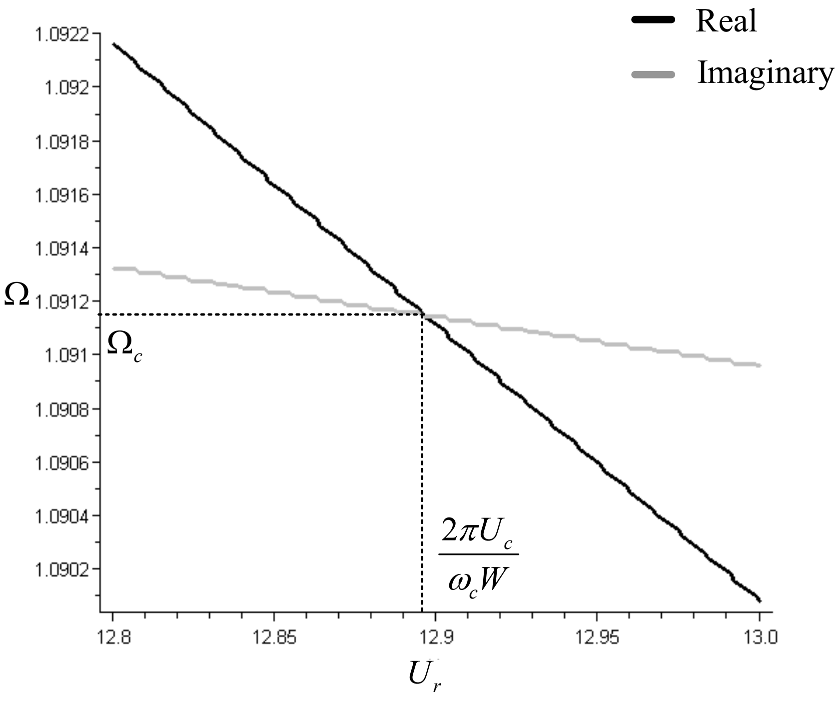

Figure 35: Illustration of the solution of the critical flutter wind velocity U_c, *at the flutter frequency, found by* Ω_c.

By use of the critical reduced velocity and the flutter frequency, the critical values can be found in a similar way as it was done for the 2d case. The two values are found as (U_c, Ω_c), (12.898;1.09175). The critical values are compared to [Hansen 1996] in the table below. A difference of less than 14 % is found, which is acceptable.

Table 4. Critical flutter wind velocities for the bridge during erection.

	Critical flutter wind velocity [m/s]	Flutter frequency [Hz]
Present work	47,6	0.119
[Hansen 1996]	43,3	N.A.

6.4. FLUID STRUCTURE INTERACTION

In the present chapter it is described how an interaction between the movements of the bridge and the fluid flow can be modelled. The aim of the exercise is to determine the critical flutter velocities of the bridge profile in a similar way as when working in a wind tunnel. The wind tunnel technique is described in section 2.3. In theory, a perfect FSI is able to simulate the exact behaviour of the system, and more detailed knowledge of the movements of the system, prior and after the critical velocity is reached, are therefore made available.

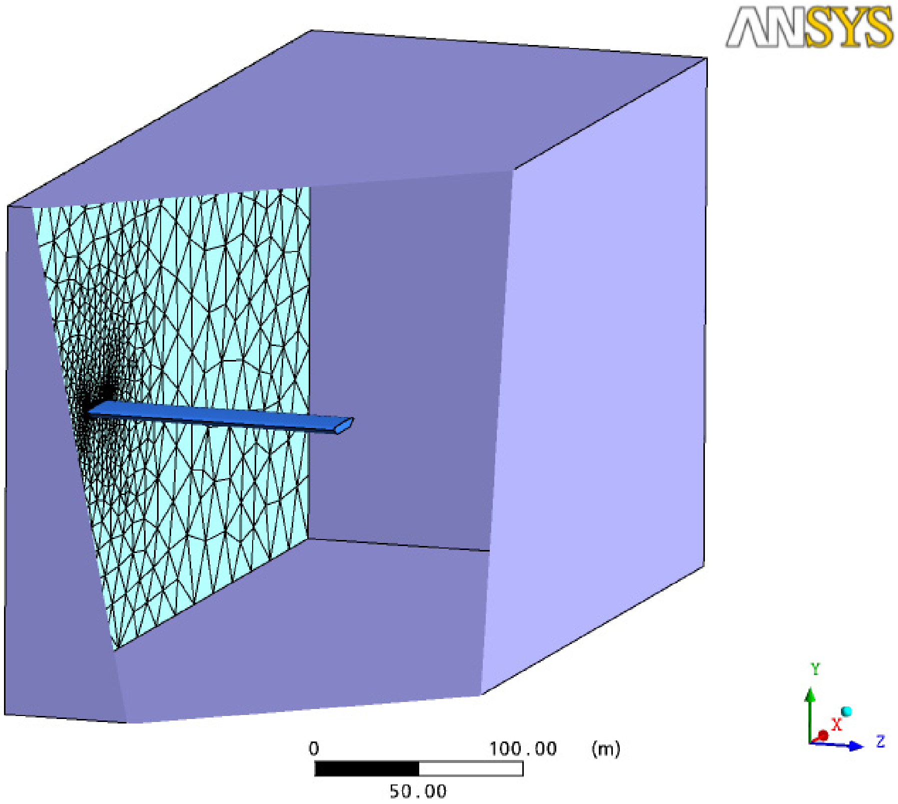

Figure 36: The three dimensional model of the bridge in the virtual wind tunnel.

In the following, the dimensions of the fluid domain, shown in Figure 36, are the same as described in appendix B. The meshing however is far coarser, to reduce the calculation time.

The formulation of the bridge itself is described in the present chapter. Two different formulations have been used in the attempt to describe the movements of the bridge deck. These are respectively a finite element model, generated in Ansys 11, and a rigid body motion generated in CFX by the use of *CFX Expression Language*, CEL. In the following these two methods are described, and the results are presented.

6.5. FSI BY FINITE ELEMENT MODELLING

In order to model the two lowest eigenmodes correctly, as described in section 4.2, a finite element model of the bridge deck can be employed. Ansys 11 has a built-in tool for structural analysis, which is used in this part of the FSI-modelling. In the construction phase, the vertical stiffness of the bridge deck is not yet established. This is a result of the method used when joining two bridge sections. Only a few hinges connects the bridge sections, allowing rotations, but not relative torsional movements. In theory, a full finite element model may be used in order to simulate the correct frequencies, mode shapes and modal masses. However, in this project the lowest frequencies and modal masses have been provided by [Hansen 1996]. These are values for the bridge when five sections have been attached – a total of 249 metres. The mode shapes have not been provided. It is therefore assumed, that the first symmetrical vertical mode shape follows the free cable movements as described in section 4. By the use of symmetry around the centre of the bridge, the mode shape is approximated by

$$\Phi_1 = 2\frac{z^3}{(2\cdot L)^3} - 3\frac{z^2}{(2\cdot L)^2} + 1 \tag{6.1}$$

where

Φ_n is the n^{th} mode shape

z is the coordinate

L is half of the length of the erected bridge.

The approximated mode shape prescribes a movement as shown in Figure 37, where the vertical movement at the centre of the bridge is twice as large as at the free end.

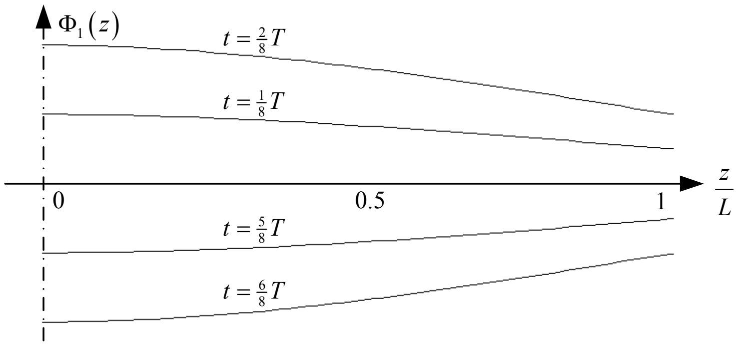

Figure 37: Approximation to the first symmetric vertical eigenmode.

The construction of an element model, which results in the correct frequencies and modal masses, can be done by the following steps:

- Determination of the mass per unit length, μ from the provided modal mass and the approximated mode shape. This is done by solving the formulation of the modal mass, as done in (6.2).

$$\begin{aligned} m_1 &= \int_0^L \mu \Phi_1^2(z)\,dx \quad \Leftrightarrow \\ m_1 &= \frac{383}{560}\mu L \quad \Leftrightarrow \\ \mu &= \frac{560}{383}\frac{m_1}{L} \end{aligned} \tag{6.2}$$

where

μ	is the mass per length
m_n	is the n^{th} modal mass

- Determination of Young's Modulus from the formulation of the modal stiffness, as done in (6.3) .

$$\begin{aligned} k_1 &= \omega_1^2 \cdot m_1 = \int_0^L EI \cdot \left(\frac{d^2\Phi_1(z)}{dz^2}\right)^2 dx \quad \Leftrightarrow \\ \omega_1^2 \cdot m_1 &= \frac{3}{4}\frac{EI}{L^3} \quad \Leftrightarrow \\ E &= \frac{4}{3}\frac{\omega_1^2 m_1 L^3}{I} \end{aligned} \tag{6.3}$$

where

k_i	is the modal stiffness
ω_n	is the n^{th} cyclic eigenfrequency
E	is Young's Modulus
I	is the second moment of area around the length axis of the bridge.

The values of μ and E are assigned to the model of the bridge and the boundary conditions are applied. The boundary conditions at the line of symmetry allow vertical movements and a rotation around the z-axis. The boundary conditions at the free end allow all movements except a rotation around the y-axis and a horizontal movement in the x-direction. Four springs are attached as shown in Figure 38.

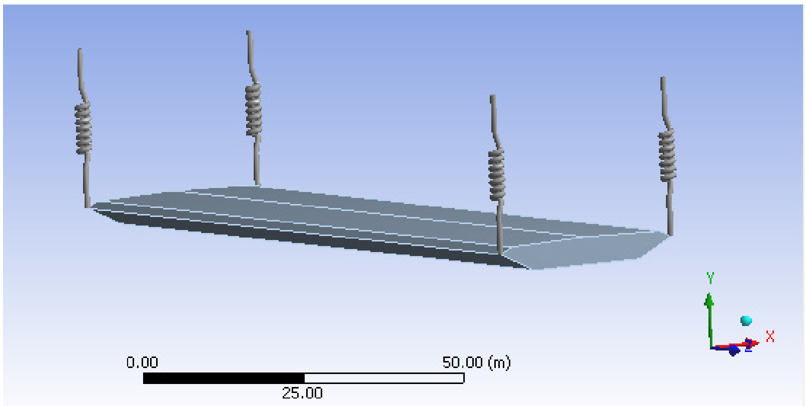

Figure 38: Structural setup for the bridge deck

The spring constants are adjusted so the frequency of the first vertical mode shape is correct. This can be done by iteration. In the present simulation a suitable set of spring constants were found by four or five iterations. Hence, the first vertical symmetrical mode shape is shown in Figure 39, which is the result of a modal analysis in Ansys.

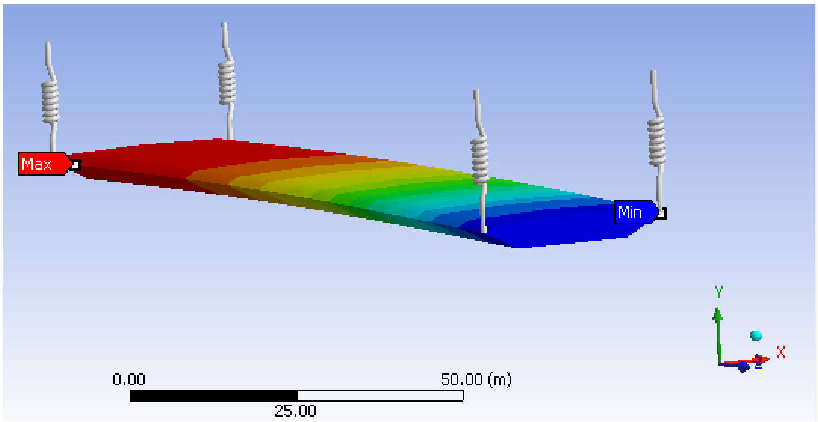

Figure 39: First symmetric vertical mode shape.

The modal mass of this mode shape should automatically be near the provided value. This may be validated by Ansys, and the mass of the bridge can be slightly adjusted to get the correct value. This naturally affects the frequency, but again an iteration of a few steps will provide a good result. The provided frequency is n_1=0.109 Hz, and the frequency found in Ansys is n_1=0.108 Hz. The first symmetrically torsional mode shape and eigenfrequency is adjusted, by moving the springs closer to- or away from the centerline of the bridge. As the bridge deck attains the torsional stiffness immediately during construction the mode shape is assumed to be one over the entire length. The mode shape is shown in Figure 40.

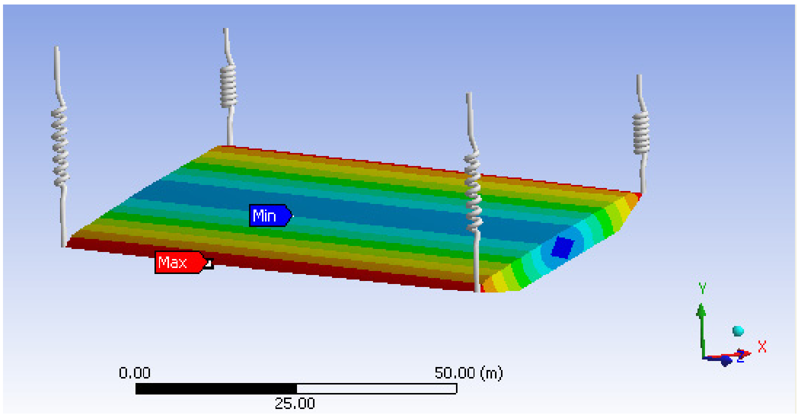

Figure 40: First symmetrical torsional mode shape.

The modal mass of this mode shape can be adjusted by adding rotational point masses between the springs.

The bridge deck is set as a Fluid Structure Surface in Ansys, which allows the loads from the fluid domain to be transferred to the structure. Iteration between the structural and the fluid solver performs the actual fluid structure interaction.

This method has not been used in this project, due to programming problems. A structural model has been built and analysed in Ansys. In this part of the process, no problems were experienced, but when the loads from the fluid domain were imported an error occurred. The error was related to the constraints of the bridge deck. The method worked well, when the constraints were changed so the bridge was fixed at the centre line. This however does not provide the correct mode shape, and the method is therefore not used.

6.6. FSI BY CFX EXPRESSION LANGUAGE

As described in section 2.3, a rigid body motion of the bridge deck can be a good approximation to the real movements of the bridge during construction. This approximation has been adopted in the wind tunnel tests, carried out in the design phase of the Great Belt Bridge. These wind tunnel tests were performed on a rigid section model of the bridge deck where the stiffness and damping were modelled by springs outside the section. A rigid body formulation in two degrees of freedom forms the basis of a FSI by CEL. The formulations for the two degrees of freedom are given in (6.4).

$$\begin{aligned} m\left(\ddot{u}+2\xi_1\omega_1\dot{u}+\omega_1^2u\right)&=F_1 \\ I\left(\ddot{\alpha}+2\xi_2\omega_2\dot{\alpha}+\omega_1^2\alpha\right)&=F_2 \end{aligned} \tag{6.4}$$

where

m	is the modal mass for the first symmetrical vertical eigenmode
I	is the modal mass moment of inertia for the first symmetrical torsional eigenmode
u	is the vertical degree of freedom
α	is the rotational degree of freedom
ξ_1	is the damping ratio of the first symmetrical vertical eigenmode
ξ_2	is the damping ratio of the first symmetrical torsional eigenmode
ω_1	is the circular eigenfrequency of the first symmetrical vertical eigenmode
ω_2	is the circular eigenfrequency of the first symmetrical torsional eigenmode
F_1	is the lift on the bridge deck
F_2	is the moment on the bridge deck

These general equations of motion can be discretized to express updated values for the two degrees of freedom when the forces on the bridge deck are calculated. In the following, the vertical movement is used as an example. The acceleration $\ddot{u}$ is discretized in (6.5).

$$\ddot{u}_{n+1}=\frac{d\dot{u}}{dt}=\frac{\dot{u}_{n+1}-\dot{u}_n}{\Delta t} \tag{6.5}$$

The updated value for the velocity $\dot{u}_{n+1}$ is found similarly in (6.6).

$$\dot{u}_{n+1}=\frac{du}{dt}=\frac{u_{n+1}-u_n}{\Delta t} \tag{6.6}$$

These updated values are inserted into (6.4).

$$\begin{gathered} m\left(\ddot{u}+2\xi_1\omega_1\dot{u}+\omega_1^2u\right)=F_1 \quad \Leftrightarrow \\ m\left(\frac{\dfrac{u_{n+1}-u_n}{\Delta t}-\dot{u}_n}{\Delta t}+2\xi_1\omega_1\frac{u_{n+1}-u_n}{\Delta t}+\omega_1^2u_{n+1}\right)=F_1 \end{gathered} \tag{6.7}$$

The updated value for the displacement u_{n+1} is the only unknown and can therefore be expressed explicitly. This is shown in (6.8).

$$u_{n+1}=\frac{mu_n+m\dot{u}_n\Delta t+2m\omega_1\xi_1\Delta tu_n+F_1\Delta t^2}{m+2m\omega_1\xi_1\Delta t+k_1\Delta t^2} \tag{6.8}$$

A similar formulation for the rotation can be found for the rotation degree of freedom. The simulation is initialized by a prescribed vertical movement of the bridge deck to a position of $u = -2m$. No initial rotation has been applied. After the initial movement has been reached, the bridge deck is released and the displacement is found by (6.8). The harmonic oscillating movements of the bridge deck will have decreasing amplitude if the wind speed is below the critical flutter wind velocity. If the amplitudes of the motion are increasing, the wind speed has surpassed the critical flutter wind velocity. Only in the unlikely event, that the exact critical flutter velocity has been applied, the bridge deck will perform an oscillating movement of constant amplitude.

6.7. VALIDATION OF THE STRUCTURE MODEL

The formulation of the dynamic system may be validated in Ansys, by applying an initial displacement and then releasing the structure. In Figure 41, the vertical oscillating movements are plotted when the bridge is released from -10 metres with an initial velocity of -2$\frac{m}{s}$.

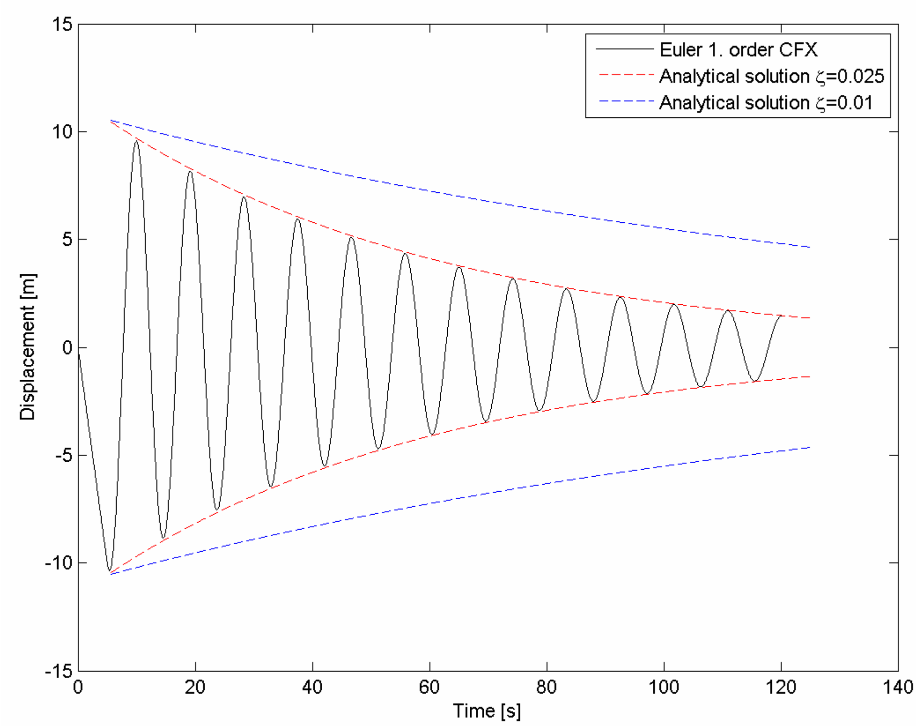

Figure 41: Vertical vibration of the bridge deck when given an initial displacement of -10 metres and an initial velociy of -2 m/s.

The wind load on the bridge deck is set to zero in this analysis and the damping ratio is $\xi = 0.01$. It is seen, that the oscillations are damped out, but not as expected. The damping ratio can be found from the formulation of the exponentially decaying functions, G enclosing the harmonic motion. The formulation is given in (6.9).

$$G = \pm A e^{-\xi \omega_0 t} \tag{6.9}$$

which is the time dependent amplitude of the general motion of a damped system, as seen in (6.10).

$$x(t) = A e^{-\xi \omega_0 t} \cos\left(\sqrt{1-\xi^2}\,\omega_0 t - \Psi\right) \tag{6.10}$$

where

$$A = \left({x_0}^2 + \left(\frac{\dot{x}_0 + \xi \omega_0 x_0}{\omega_0 \sqrt{1-\xi^2}} \right)^2 \right)^{\frac{1}{2}}$$

$$\tan \Psi = \left(\frac{\dot{x}_0 + \xi \omega_0 x_0}{x_0 \omega_0 \sqrt{1-\xi^2}} \right)$$

“0” denotes initial values, and the dot is the number of time derivations.

[Nielsen 2004]

The damping ratio is found to be $\xi = 0.025$, as seen in Figure 41, which is somewhat larger than expected. The numerical integration scheme used in this simulation is a first order backward Euler algorithm, with a time step of 0.044 s. A Newmark algorithm has also been tested, with the same result. It is, however, believed that the solution algorithm is part of the reason for the energy dissipation from the system, which is not unusual in many numerical integration schemes. [Nielsen 2005] notes that damping in a Newmark algorithm requires extremely small time steps. The programming in CEL may have some error, which needs to be investigated further if the results are to be used.

The modelling of the natural frequencies is of the highest importance when simulating flutter. In the vibration test the frequency is found by FFT. A normalised single sided frequency spectrum is shown in Figure 42. It can be seen that the natural frequency of $n = 0.109\,\text{Hz}$ is dominating.

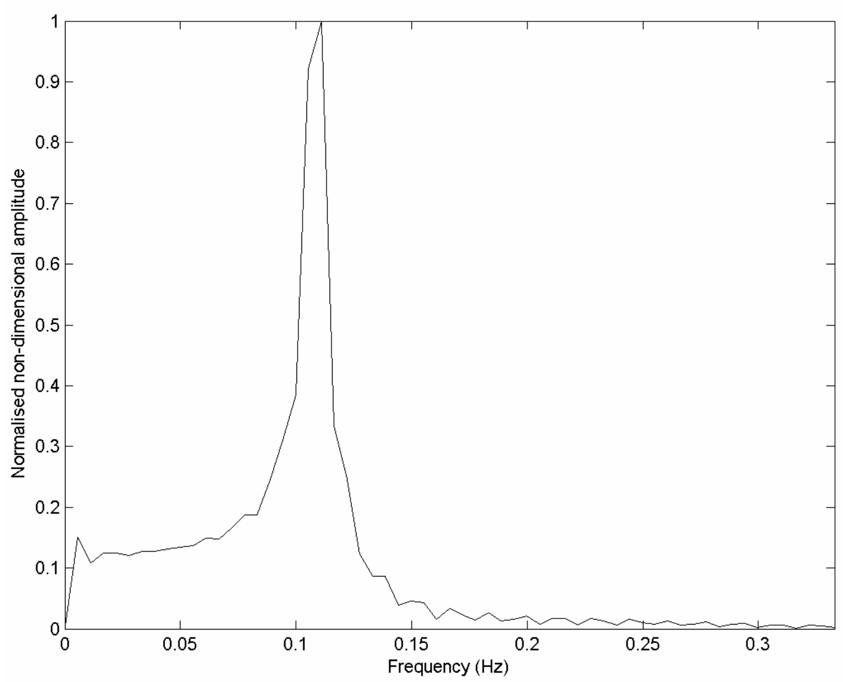

Figure 42: Normalized single sided frequency spectrum of vertical vibration test

A similar vibration test can be performed for the rotational degree of freedom. The results are similar for this case: A correct frequency is modeled, but the damping is too high.

6.8. RESULTS OF THE 3D FSI ANALYSIS

The critical flutter wind velocity for the bridge under construction, found by the use of the forced vibration test, as shown in section 5, is $U_c = 47.6 \frac{m}{s}$ with a flutter frequency of 0.119 Hz. [Hansen 1996] has found a critical velocity of $U_c = 43.3 \frac{m}{s}$. A range of FSI-simulations around these velocities have been performed, in order to compare the two methods. It is found that flutter occur at a lower velocity than expected, probably as a result of a problematic system. The oscillation amplitude for 20 and 25 $\frac{m}{s}$ are seen in the figure below. The critical flutter wind velocity is expected to be found in this interval, due to the diverging oscillations for the simulation with 25 $\frac{m}{s}$ compared to the more stable, but slightly decaying oscillations, for 20 $\frac{m}{s}$. As a higher damping results in a higher critical flutter wind velocity, it must be concluded that the problem relating the solution of the system, not only is related to the damping ratio. Furthermore, the FSI also permits other aeroelastic phenomena as single-mode flutter and galloping, which also may influence the results.

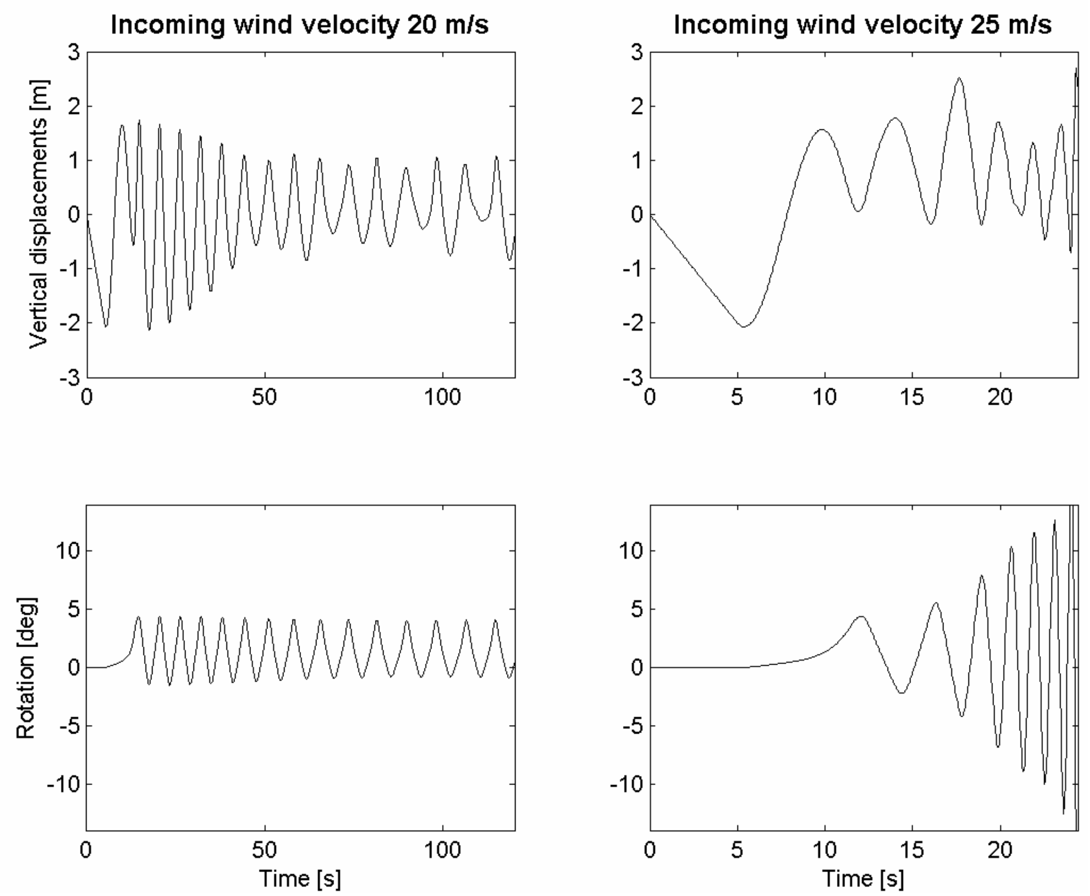

Figure 43: Vertical and rotational movements for 20 $\frac{m}{s}$ and 25 $\frac{m}{s}$.

For the case with an incoming wind of 25 $\frac{m}{s}$, the frequency of the oscillations are found to approximately 0.122 Hz, which is close to the calculated flutter frequency, and is in between the vertical and rotational natural frequencies of 0.109 Hz and 0.135 Hz, respectively.

As seen in the flutter condition, the critical flutter wind velocity is dependent on the frequency separation, and a high frequency separation will lead to a high critical flutter wind velocity. The damping also has a positive effect on the critical velocity, as mentioned previously, and shown in Figur 44.

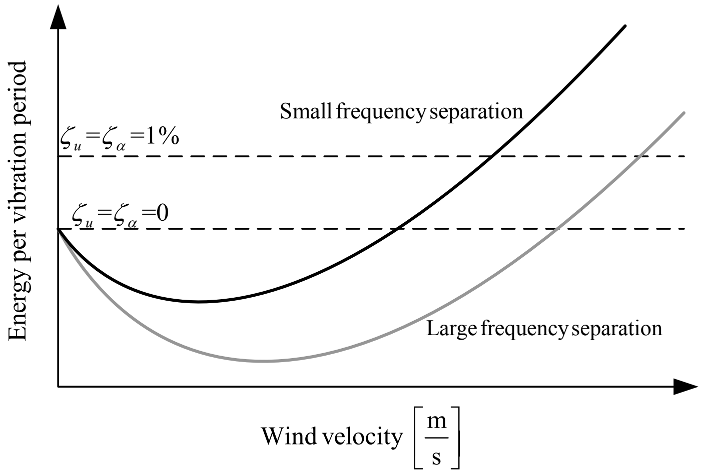

Figur 44: The influence of frequency separation and damping on the critical flutter wind velocity. The dotted lines show the energy dissipation per vibration period and the solid lines the input. [Hansen and Dyrbye 1997]

To illustrate the importance of the frequency separation, the FSI-calculations are performed for a higher rotational natural frequency. This leads to a frequency ratio, γ_ω, on 4.59, compared to the real value of 1.24. The influence this has on the oscillations is seen in Figure 45.

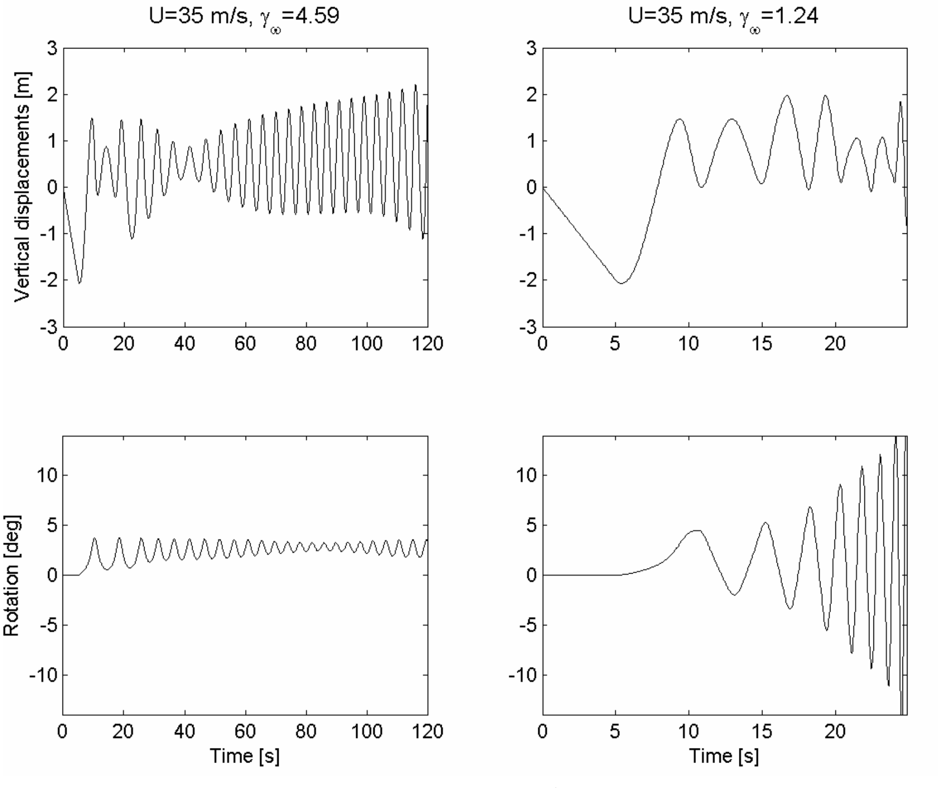

Figure 45: The influence of frequency separation for 35 m/s in the FSI-simulation.

It is clearly seen that the rotational movements are decaying for the case of a high frequency separation. The growing vertical displacements could be created by the same effects as seen for galloping.

An illustration of flutter, fully developed for a high incoming velocity, is illustrated on the figure below. The case of the high frequency separation is used to ensure a high critical velocity.

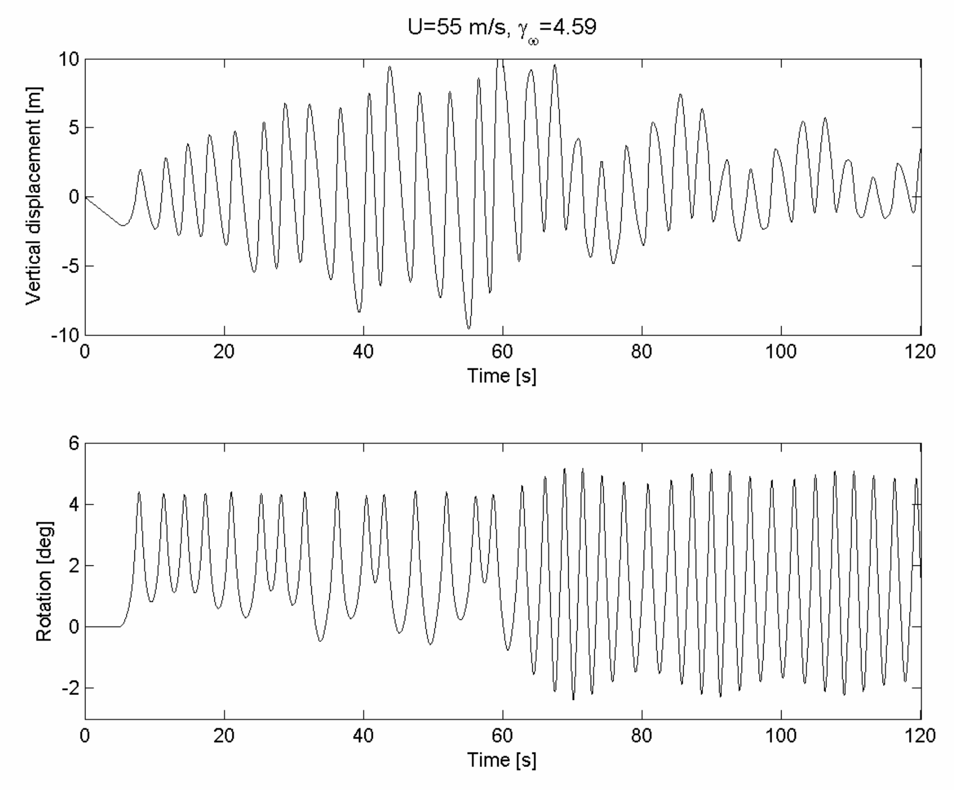

Figure 46: Flutter, with shift in the dominating mode.

As seen in Figure 46, the dominating mode in the flutter movements shifts from the vertical mode to the rotational mode, at approximately 60 s of simulation time, indicating that the rotational and vertical movements are uncoupled. This leads to believe that the bridge is undergoing single-mode flutter, initially for vertical movements, but then changing to rotational movements at t=60 s.

The flow in the FSI-simulation is shown in Figure 47 and Figure 48 for the case with the lowest frequency separation and a velocity of the incoming wind of $35\,\frac{m}{s}$. The bridge deck is shown just before the oscillations increase dramatically, causing the simulation to end.

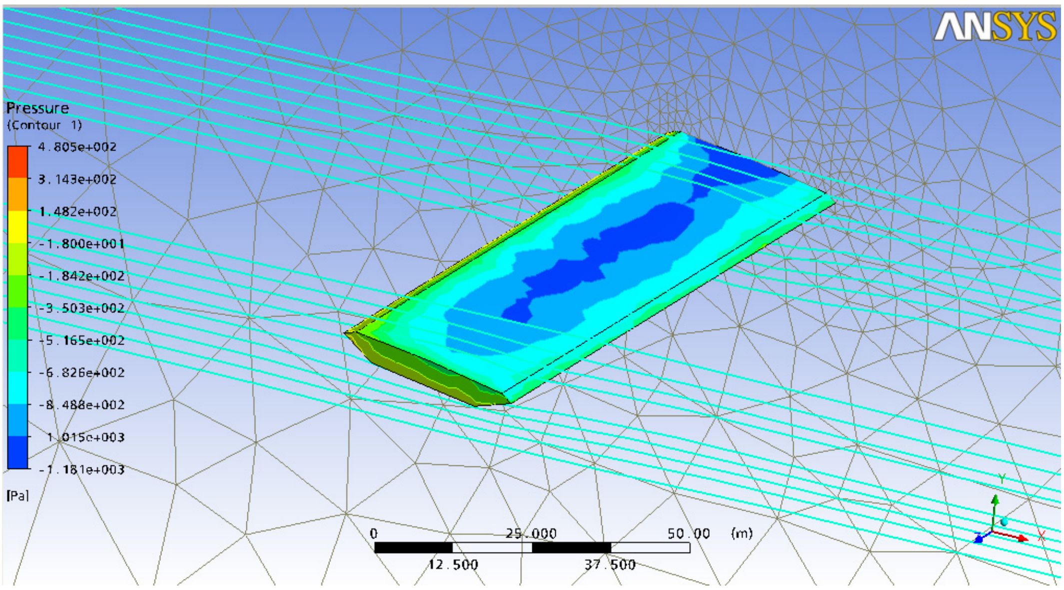

Figure 47: The bridge deck in flutter. There is negative aerodynamic damping, due to the suction on the top of the deck for an upwards movement.

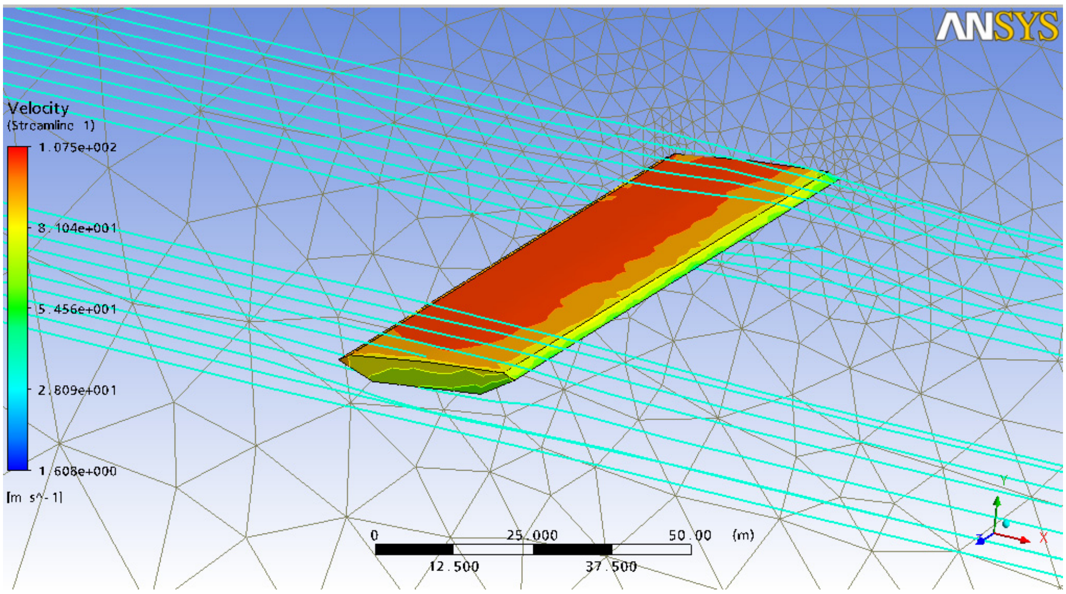

Figure 48: The bridge deck in flutter, with aerodynamic damping in the case where the bridge deck is moving down.

7. REFERENCES

[Al-Assaf 2006] ISSN/ISBN
Adel Al-Assaf
Flutter Analysis of Open-Truss Stiffened Suspension Bridges Using Synthesized Aerodynamic Derivatives
WASHINGTON STATE UNIVERSITY, Department of Civil and Environmental Engineering

[Ansys 2006]
Ansys
Ansys CFX-Solver Theory Guide

[Awruch and Braun 2003] 1678-5878
A. M. Awruch and A. L. Braun
Numerical Simulation of the Wind Action on a Long-Span Bridge Deck
Journal of the Brazilian Society of Mechanical Sciences and Engineering

[Brorsen 2005]
Michael Brorsen
Strømningslære
Instituttet for Vand, Jord og Miljøteknik, Aalborg Universitet

[Chen and Kareem 2003]
Xinzhong Chen and Ahsan Kareem
New Frontiers in Aerodynamic Tailoring of Long-Span Bridges: An Advanced Analysis Framework
Department of Civil Engineering and Geological Sciences, University of Notre Dame

[Diana et al 2006]
G. Diana, F. Resta, M. Belloli, D. Rocchi
On the vortex shedding forcing on suspension bridge deck
Journal of Wind Engineering and Industrial Aerodynamics 94 (2006) 341–363

[EN 1991-1-4 2005]
Eurocode 1: Actions on structures - Part 1-4: General actions - Wind actions

[Enevoldsen et al 1997] 90 5809 059 0
I. Enevoldsen, C. Pederson, S. O. Hansen, L. T. Thorbek and T. Kvamsdal
Computional Wind Simulations for Cable-Supported Bridges.
Wind Engineering into the 21st century, Vol. 2., pp 1265-1270

[Frandsen 2003]
J. B. Frandsen
Numerical Bridge Deck Studies Using Finite Elements Part I:Flutter
Department of Civil and Environmental Engineeering, Louisiana State University

[Gu and Qin 2004]
Ming Gu and Xian-Rong Qin
Direct Identification of Flutter Derivatives and Aerodynamic Admittances of Bridge Dekcs
State Key Laboratory for Disaster Reduction in Civil Engineering, Tongji University

[Hansen 1996]
Svend Ole Hansen and Lars T. Thorbek
Analysis of Critical Flutter Wind Velocities During Construction

[Hansen 1997]
Svend Ole Hansen and Lars T. Thorbek
Buffeting Response of the Great Belt Suspension Bridge During Construction

[Hansen 2008]
Svend Ole Hansen and Lars T. Thorbek
Aerodynamic derivatives for the completed Great Belt Bridge
Aerodynamic derivatives recieved from Lars Thorbek in an Excel spreadsheet. The data is based on wind tunnel tests carried out in 1996.

[Hansen og Dyrbye 1997] 0 471 95651 1
Svend Ole Hansen og Claës Dyrbye
Wind Loads on Structures

[Malalasekera and Versteeg 2007] 978-0-13-127498-3
W. Malalasekera and H. K. Versteeg
An introduction to computational fluid dynamics - The finite volume method

[Menter 1993]
F.R. Menter
Zonal Two Equation k-omega Turbulence Models For Aerodynamic Flows
Paper recieved by Niels N. Sørensen, Risø.

[Morgenthal 2000]
Guido Morgenthal
Fluid-Structure Interaction in Bluff-Body Aerodynamics and Long-Span Bridge Design: Phenomena and Methohds
University of Cambridge, Department of Engineering

[Morgenthal and McRobie 2000]
Guido Morgenthal and F.A. McRobie
A Comparative Study of Numerical Methods for Fluid-Structure
Interaction Analysis in Long-Span Bridge Design

[Nielsen 2004] 1395-8232
Søren R. K. Nielsen U2004-1
Vibration Theory, Vol 1. Linear Vibration Theory

[Nielsen 2005] 1395-8232
Søren R. K. Nielsen U2005-1
Structural Dynamics Vol 9 - Computational Dynamics

[Nielsen et al. 2007]
Søren R. K. Nielsen, Jesper Stærdahl and Niels Sørensen
Aeroelastic Stability of Suspension Bridges using CFD

[Reinhold et al 1992] 90 5410 0427
T.A. Reinholdt, M. Brinch and M. Damsgaard
Wind Tunnel Tests for the Great Belt Link
Aerodynamics of Large Bridges, proceedings of the 1. International
Symposium 1992, Copenhagen Denmark.

[Scanlan 1978]
Robert H. Scanlan
The Action of Flexible Bridges Under Wind, I: Flutter Theory
Department of Civil Engineering, Princeton University

[Scanlan 1993]
Robert H. Scanlan
Problematics In Formulation of Wind-Force Models for Bridge Decks
Journal of Engineering Mechanics, Vol. 119, No. 7, July, 1993

[Scanlan 1997]
Robert H. Scanlan
Amplitude and Turbulence Effects on Bridge Flutter Dervatives

[Thorbek 2008]
Lars T. Thorbek
Meeting with Lars Thorbæk, Rambøll. Lars Thorbæk worked with
Svend Ole Hansen ApS, when the company was investigating the Great
Belt Bridge by wind tunnel tests. Lars Thorbæk is presently senior
project manager in Rambøll's dapartement for bridges

[Vairo 2003]
Giuseppe Vairo
A numerical model for wind loads simulation on long-span bridges

[Wilcox 2006] 978-1-928729-08-2
David C. Wilcox
Turbulence Modeling for CFD, 3rd edition

[Zahlten and Eusani 2006]
Wolfhard Zahlten and Renato Eusani
Numerical simulation of the aeroelastic response of bridge structures including instabilities
Institute for Structural Mechanics and Numerical Methods, University of Wuppertal, Pauluskirchstrasse 7, D-42285 Wuppertal, Germany

[Zill and Cullen 2001] 0-534-38002-6
Dennis G. Zill and Michael R. Cullen
Differential Equations with Boundary-Value Problems, 5th edition

TABLE OF CONTENTS

APPENDIX A: AERODYNAMIC DERIVATIVES AND FLUTTER CONDITION

By use of the equation of motion, disregarding the dead loads by considering the system from the equilibrium state, [Nielsen 2004], and by performing the analysis from the aerostatic equilibrium, created by the load from the mean wind, the vertical system of one degree of freedom reduces to

$$m\ddot{u} + c\dot{u} + ku = F_{ae} \tag{A.1}$$

Formula (A.1) thereby describe the equation of motion of a moving bridge deck, disregarding buffeting and turbulence, as explained in detail in section 3.3. The equation can be rewritten as

$$\ddot{u} + \frac{c}{m}\dot{u} + \frac{k}{m}u = \frac{F_{ae}}{m} \tag{A.2}$$

By introducing the circular eigenfrequency and the definition of the damping ratio from [Nielsen 2004], the system can be written as

$$\ddot{u} + 2\zeta\omega_0\dot{u} + \omega_0^2 u = \frac{F_{ae}}{m} \tag{A.3}$$

where

ω_0	is the circular eigenfrequency of the system
ζ	is the damping ratio

The force, created by the self-excited bridge deck, is now described by introducing the notation from [Scanlan 1978]. A two-degree-of-freedom system is considered, neglecting the drag. The effect of the vertical displacement on the loads is also omitted. Also, the inertial coefficients for the vertical and rotational acceleration is assumed to be negligible, since very heavy structures, as a bridge deck, is seldom exposed to large accelerations, even in the case of resonance. This leads to a system, for both moment and lift, of three aerodynamic derivatives for both the vertical and rotational motion. This notation is based on the assumption of a linear connection between forces and the structural displacements, as mentioned previously. The equations, for both the vertical and rotational motions, are shown in (A.4). [Scanlan 1978]

$$\begin{aligned} &\ddot{u} + 2\zeta_u \omega_{0,u} \dot{u} + \omega_{0,u}^2 u = H_1 \dot{x} + H_2 \dot{\alpha} + H_3 \alpha \\ &\ddot{\alpha} + 2\zeta_\alpha \omega_{0,\alpha} \dot{\alpha} + \omega_{0,\alpha}^2 \alpha = A_1 \dot{x} + A_2 \dot{\alpha} + A_3 \alpha \end{aligned} \tag{A.4}$$

where

H_i, A_i are coefficients that describe the self-excited aerodynamic effects

If all the derivatives were to be included, the system would consist of six AD's, for each load term, hereby still neglecting the coefficients for acceleration. It is noted that several constants, such as the mass as seen from (A.3) to (A.4), is contained in the coefficients. By introducing a number of dimensionless variables, which also ensures an easier transfer from model to full scale sizes, the full equation of motion, as shown in (A.1), can be written as shown in (A.5). The equation in (A.5) is on a slightly different form as the one introduced in [Scanlan 1978], and results in aerodynamic derivatives twice the magnitude and with different sign convention. [Hansen 1997]

$$\begin{aligned} m\left(\ddot{u} + 2\zeta_u \omega_{0,u} \dot{u} + \omega_{0,u}^2 u\right) &= \frac{1}{2}\rho U^2 W \left(K H_1^*(K) \frac{\dot{u}}{U} + K H_2^*(K) \frac{W\dot{\alpha}}{U} + K^2 H_3^*(K) \alpha \right) \\ I\left(\ddot{\alpha} + 2\zeta_\alpha \omega_{0,\alpha} \dot{\alpha} + \omega_{0,\alpha}^2 \alpha\right) &= \frac{1}{2}\rho U^2 W^2 \left(K A_1^*(K) \frac{\dot{u}}{U} + K A_2^*(K) \frac{W\dot{\alpha}}{U} + K^2 A_3^*(K) \alpha \right) \end{aligned} \tag{A.5}$$

where

H_i^*, A_i^* are the aerodynamic derivatives, for the vertical and rotational motion respectively

U is the mean wind velocity of the incoming wind

The aerodynamic derivatives are functions of the motion and the incoming wind, here described by the reduced frequency, *K*.

$$K = \frac{W\omega}{U} \tag{A.6}$$

where

ω is the circular flutter frequency of the bridge deck

[Hansen and Dyrbye 1997]

Identification of the aerodynamic derivatives is possible by finding the relation between the self-excited forces on the bridge deck, and the motion. This is done, as previously mentioned, by prescribing a harmonic motion to the system, and assuming that the motion-induced lift and moment varies in the same way. The dimensionless lift and moment coefficients are used, and here the reason for using the modified Scanlan notation becomes clear, when observing that the denominator resembles part of (A.5), when considering the length to be unity.

$$C_L = \frac{F_y}{\frac{1}{2}\rho U^2 W L}$$
$$C_M = \frac{M_z}{\frac{1}{2}\rho U^2 W^2 L} \tag{A.7}$$

where

C_L	is the lift coefficient [-]
C_M	is the moment coefficient [-]
F_y	is the measured lift force [N]
M_z	is the measured moment [Nm]
L	is the length of the considered bridge section [m]

The harmonic behavior of the system is introduced, by use of the following expressions for the vertical and rotational motion

$$\begin{Bmatrix} u(t) \\ \alpha(t) \end{Bmatrix} = \begin{Bmatrix} \tilde{u} \\ \tilde{\alpha} \end{Bmatrix} e^{i\omega t} \tag{A.8}$$

where

$u(t),\alpha(t)$	is the translation and rotation respectively
$\tilde{u}\,,\tilde{\alpha}$	is the amplitude of the translation and rotation respectively.
ω	is the frequency
t	is the time variable [s]

The force, described by the moment and lift coefficient, is expected to vary in a similar way. A phase difference, between the motion and the load is assumed in a similar way as derived in [Nielsen 2004]. Equation (A.5) is then written as

$$C_L e^{i(\omega t-\psi_L)} = \left(KH_1^*(K)\frac{\dot{u}}{U} + KH_2^*(K)\frac{W\dot{\alpha}}{U} + K^2 H_3^*(K)\alpha \right) e^{i\omega t}$$
$$C_M e^{i(\omega t-\psi_M)} = \left(KA_1^*(K)\frac{\dot{\alpha}}{U} + KA_2^*(K)\frac{W\dot{\alpha}}{U} + K^2 A_3^*(K)\alpha \right) e^{i\omega t} \tag{A.9}$$

where

ψ	is the phase difference between the motion and load

By inserting the function for the motion derivatives, found by use of (A.8), formula (A.9) can be written as

$$
\begin{aligned}
C_L e^{i(\omega t-\psi_L)} &= K\left(i\omega H_1^*\left(K\right)\frac{\tilde{u}}{U} + i\omega H_2^*\left(K\right)\tilde{\alpha}\frac{W}{U} + KH_3^*\left(K\right)\tilde{\alpha} \right)e^{i\omega t} \\
C_M e^{i(\omega t-\psi_M)} &= K\left(i\omega A_1^*\left(K\right)\frac{\tilde{u}}{U} + i\omega A_2^*\left(K\right)\tilde{\alpha}\frac{W}{U} + KA_3^*\left(K\right)\tilde{\alpha} \right)e^{i\omega t}
\end{aligned} \tag{A.10}
$$

Derivation of the aerodynamic derivatives, related to the lift force, is performed. Derivation of the ones for the moment is considered trivial. By use of the reduced frequency, (A.10) is written as

$$
C_L e^{i(\omega t-\psi_L)} = K^2\left(iH_1^*\left(K\right)\frac{\tilde{u}}{B} + \tilde{\alpha}\left(iH_2^*\left(K\right) + H_3^*\left(K\right)\right) \right)e^{i\omega t} \tag{A.11}
$$

The aerodynamic derivative H_1^* is related to the damping of the vertical motion, as seen in the formulas. It is only relevant for the vertical motion, and for this motion, $\tilde{\alpha}$ is zero, making it possible to define H_1^* as

$$
H_1^* = \mathrm{Im}\left(\frac{C_L W e^{-i\psi_L}}{K^2\tilde{u}} \right) \tag{A.12}
$$

By considering (A.11) in the case of the rotational motion, H_2^* and H_3^* is found as the imaginary and real part, respectively, of the same expression.

$$
\begin{aligned}
H_2^* &= \mathrm{Im}\left(\frac{C_L e^{-i\psi_L}}{K^2\tilde{\alpha}} \right) \\
H_3^* &= \mathrm{Re}\left(\frac{C_L e^{-i\psi_L}}{K^2\tilde{\alpha}} \right)
\end{aligned} \tag{A.13}
$$

In a similar way, the remaining three aerodynamic derivatives are found as

$$
\begin{aligned}
A_1^* &= \mathrm{Im}\left(\frac{C_M W e^{-i\psi_M}}{K^2\tilde{u}} \right) \\
A_2^* &= \mathrm{Im}\left(\frac{C_M e^{-i\psi_M}}{K^2\tilde{\alpha}} \right) \\
A_3^* &= \mathrm{Re}\left(\frac{C_M e^{-i\psi_M}}{K^2\tilde{\alpha}} \right)
\end{aligned} \tag{A.14}
$$

Flutter occurs at the motion-induced wind load, created by the so called critical wind velocity, at which the vertical and torsional vibration couple at the flutter frequency. The flutter frequency is found between $\omega_{0,u}$ and $\omega_{0,\alpha}$ and it is assumed that the vertical and rotational motion are of the same frequency. Identification of these two variables are done by deriving them from (A.5). When the motion defined in (A.8), and the respective derivatives, are inserted into (A.5), the two equations take the following forms.

$$
\begin{aligned}
m\tilde{x}e^{i\omega t}\left(-\omega^2+2i\zeta_u\omega_{0,u}\omega+\omega_{0,u}^2\right)&=\frac{1}{2}\rho U^2W\left(KH_1^*(K)\frac{i\omega\tilde{x}}{U}+KH_2^*(K)\frac{i\omega W\tilde{\alpha}}{U}+K^2H_3^*(K)\tilde{\alpha}\right)e^{i\omega t}\\
I\tilde{\alpha}e^{i\omega t}\left(-\omega^2+2i\zeta_\alpha\omega_{0,\alpha}\omega+\omega_{0,\alpha}^2\right)&=\frac{1}{2}\rho U^2W^2\left(KA_1^*(K)\frac{i\omega\tilde{x}}{U}+KA_2^*(K)\frac{i\omega W\tilde{\alpha}}{U}+K^2A_3^*(K)\tilde{\alpha}\right)e^{i\omega t}
\end{aligned}
\tag{A.15}
$$

By rearranging and using the reduced frequency, defined in (A.6), the equations can be written as

$$
\begin{aligned}
\tilde{x}\left(-\omega^2+2i\zeta_u\omega_{0,u}\omega+\omega_{0,u}^2\right)&=\frac{\rho U^2W}{2m}K^2\left(i\frac{\tilde{x}}{W}H_1^*(K)+i\tilde{\alpha}H_2^*(K)+\tilde{\alpha}H_3^*(K)\right)\\
\tilde{\alpha}\left(-\omega^2+2i\zeta_\alpha\omega_{0,\alpha}\omega+\omega_{0,\alpha}^2\right)&=\frac{\rho U^2W^2}{2I}K^2\left(i\frac{\tilde{x}}{W}A_1^*(K)+i\tilde{\alpha}A_2^*(K)+\tilde{\alpha}A_3^*(K)\right)
\end{aligned}
\tag{A.16}
$$

For simplification, the normalized masses defined in (A.17) are introduced, and by inserting *K,* the equations are further reduced in form. Note that the normalized masses in (A.17) are introduced by use of the modal masses, since it is of extreme importance that the contribution from the whole bridge, for example the mass of vibrating cables, are included in the simplified 2-dof system. This is explained later in this section.

$$
\gamma_m=\frac{m_e}{\rho W^2}\qquad\qquad \gamma_I=\frac{I_e}{\rho W^4}
\tag{A.17}
$$

$$
\begin{aligned}
\frac{\tilde{x}}{W}\left(-\omega^2+2i\zeta_u\omega_{0,u}\omega+\omega_{0,u}^2\right)&=\frac{\omega^2}{2\gamma_m}\left(i\frac{\tilde{x}}{W}H_1^*(K)+i\tilde{\alpha}H_2^*(K)+\tilde{\alpha}H_3^*(K)\right)\\
\tilde{\alpha}\left(-\omega^2+2i\zeta_\alpha\omega_{0,\alpha}\omega+\omega_{0,\alpha}^2\right)&=\frac{\omega^2}{2I}\left(i\frac{\tilde{x}}{W}A_1^*(K)+i\tilde{\alpha}A_2^*(K)+\tilde{\alpha}A_3^*(K)\right)
\end{aligned}
\tag{A.18}
$$

By identifying H_2^* and H_3^* and A_2^* and A_3^* as defining a complex number, which together can be shown to define the damping and stiffness in the rotational motion, for lift and moment forces, explicitly defined in [Gu and Qin 2004], but can be derived from the equations in this sections, (A.18) is arranged as shown below.

$$
\begin{aligned}
\frac{\tilde{x}}{W}\left(-\omega^2+2i\zeta_u\omega_{0,u}\omega+\omega_{0,u}^2\right)&=\frac{\omega^2}{2\gamma_m}\left(i\frac{\tilde{x}}{W}H_1^*(K)+\tilde{\alpha}\left(iH_2^*(K)+H_3^*(K)\right)\right)\\
\tilde{\alpha}\left(-\omega^2+2i\zeta_\alpha\omega_{0,\alpha}\omega+\omega_{0,\alpha}^2\right)&=\frac{\omega^2}{2I}\left(i\frac{\tilde{x}}{W}A_1^*(K)+\tilde{\alpha}\left(iA_2^*(K)+A_3^*(K)\right)\right)
\end{aligned}
\tag{A.19}
$$

By dividing all parts with the circular natural eigenfrequency squared for the vertical motion, $\omega_{0,u}^2$, and introducing the following two dimensionless quantities in (A.20), the equation can be rewritten as shown in (A.21)

$$
\Omega=\frac{\omega}{\omega_{0,u}}\qquad\qquad \gamma_\omega=\frac{\omega_{0,\alpha}}{\omega_{0,u}}
\tag{A.20}
$$

$$\begin{aligned}
&\frac{\tilde{x}}{W}\left(-\Omega^2+2i\zeta_u\Omega+1-i\frac{\Omega^2}{2\gamma_m}H_1^*(K)\right)-\tilde{\alpha}\left(\frac{\Omega^2}{2\gamma_m}\left(iH_2^*(K)+H_3^*(K)\right)\right)=0\\
&\frac{\tilde{x}}{W}\left(-i\frac{\Omega^2}{2\gamma_I}A_1^*(K)\right)+\tilde{\alpha}\left(-\Omega^2+2i\zeta_\alpha\gamma_\omega\Omega+\gamma_\omega^2-\frac{\Omega^2}{2\gamma_I}\left(iA_2^*(K)+A_3^*(K)\right)\right)=0
\end{aligned} \tag{A.21}$$

It is noted, that the flutter condition, shown in (A.21), is valid only for bridge deck section, with constant mode shapes, assuming a coupling coefficient between the two modes of one. If the equations in (A.21) are to be used in a modal analysis when considering several mode shapes, coupling coefficients and modal coordinates must be introduced, and all masses generalized. The coupling coefficients are introduced on the parts, which describe the connection between the vertical and the rotational motion, and vice versa. This is shown in (A.22).

$$\begin{aligned}
&\frac{\tilde{x}}{W}\left(-\Omega^2+2i\zeta_u\Omega+1-i\frac{\Omega^2}{2\gamma_m}H_1^*(K)\right)-\tilde{\alpha}\left(\frac{C_u\Omega^2}{2\gamma_m}\left(iH_2^*(K)+H_3^*(K)\right)\right)=0\\
&\frac{\tilde{x}}{W}\left(-i\frac{C_\alpha\Omega^2}{2\gamma_I}A_1^*(K)\right)+\tilde{\alpha}\left(-\Omega^2+2i\zeta_\alpha\gamma_\omega\Omega+\gamma_\omega^2-\frac{\Omega^2}{2\gamma_I}\left(iA_2^*(K)+A_3^*(K)\right)\right)=0
\end{aligned} \tag{A.22}$$

where

C is the coupling coefficient for the two modes considered [-]

[Hansen and Dyrbye 1997]

The two equations are written in matrix form.

$$\begin{aligned}
&\mathrm{A}\bar{x}=0\\
&\begin{bmatrix}
-\Omega^2+2i\zeta_u\Omega+1-i\dfrac{\Omega^2}{2\gamma_m}H_1^*(K) & -\dfrac{\Omega^2}{2\gamma_m}\left(iH_2^*(K)+H_3^*(K)\right)\\
-i\dfrac{\Omega^2}{2\gamma_I}A_1^*(K) & -\Omega^2+2i\zeta_\alpha\gamma_\omega\Omega+\gamma_\omega^2-\dfrac{\Omega^2}{2\gamma_I}\left(iA_2^*(K)+A_3^*(K)\right)
\end{bmatrix}
\begin{bmatrix}\dfrac{\tilde{x}}{W}\\ \tilde{\alpha}\end{bmatrix}=\begin{bmatrix}0\\0\end{bmatrix}
\end{aligned} \tag{A.23}$$

The trivial solutions of the system, where the motion amplitudes are zero, are not of interest. Therefore, (A.23) must be fulfilled when the matrix, A, is non-invertible, found when the determinant is zero. This must be fulfilled for both the real and imaginary part of the matrix, thereby making it possible to define two governing multivariate, non-linear equations to solve the system.

$$\begin{aligned}
\mathrm{Re}\left(\det(\mathrm{A})\right)=0\\
\mathrm{Im}\left(\det(\mathrm{A})\right)=0
\end{aligned} \tag{A.24}$$

The dimensionless variable Ω is thereby assumed to describe the flutter frequency ω, on complex form, written as $\omega_1 + i\omega_2$, for which the flutter oscillation is decaying when $\omega_2>0$ and increasing for $\omega_2<0$. The critical flutter wind velocity is found when the oscillation is neither decaying nor diverging, for $\omega_2=0$. [Hansen and Dyrbye 1997]. Solution of the system is done by finding the case for which the real and imaginary part intersects. The two equations are solved for both Ω and K, or U_r.

APPENDIX B: MESH REQUIREMENTS

In the present chapter, the meshing strategy is discussed. It is investigated how different meshing techniques can be used to capture different phenomena of a flow around a sharp edged body. In order to start building the mesh around the bridge profile, the expected flow pattern must be identified. In Figure 1, a schematic flow around a stationary bridge profile is visualised.

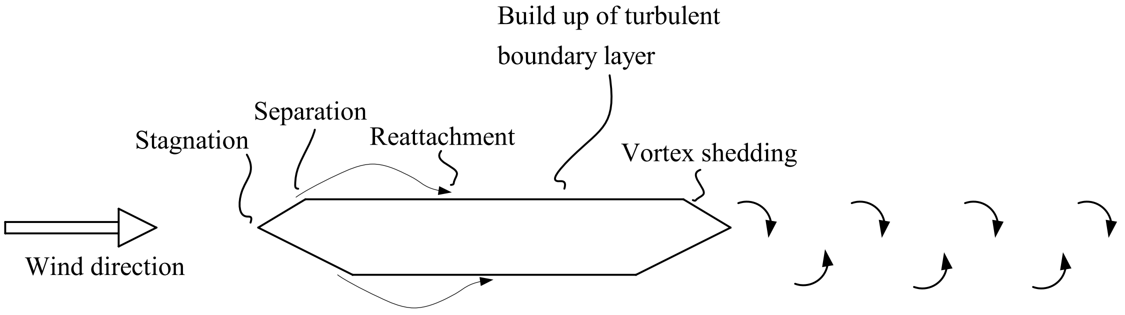

Figure 1: Schematic flow around a bridge profile

On the windward side of the profile, a point of stagnation is expected for a bridge at rest. On the first two edges the flow is expected to separate, forming two standing vortices. Due to the relatively large afterbody it is expected that the flow reattaches to the bridge deck. After the reattachment a turbulent boundary layer builds up until the end of the profile is reached. Due to the sharp edges on the leeward side of the profile, vortices are expected to be shed periodically forming a well known vortex street in the wake.

To capture all these phenomena an extremely fine mesh structure is required. Not all phenomena are, however essential to the determination of aerodynamic derivatives, which is the scope of these simulations. In the following, the domain size and the flow phenomena in Figure 1 are commented. The performed analysis are all modelled to full scale, so mesh statistics can easily be compared to characteristic lengths of the bridge.

B.1 DOMAIN SIZE

The size of the domain is dictated by two contradicting requirements. One the one hand, the domain must be sufficiently large so the boundaries have a minimal impact on the flow around the bridge profile. This means that the streamlines near the boundaries must be independent of the bridge profile. For the upper and lower confining walls the streamlines must be parallel to the boundaries. In the upstream area it is important that the flow is approximately horizontal before curving around the profile. In the wake a great deal of turbulence is generated. If the simulation must capture the full wake after the profile, an extremely large domain is required. In practical use the wake is normally cut off some lengths downstream from the profile.

On the other hand, an increasing domain size will add to the computer processing time, cpu-time. It is found, that there is a linear connection between number of mesh elements and the cpu-time. The mesh used in this analysis is described in section B.7. Four simulations have been run with different sizes of domain, as shown in Figure 2. The mesh statistics are given in Table 1.

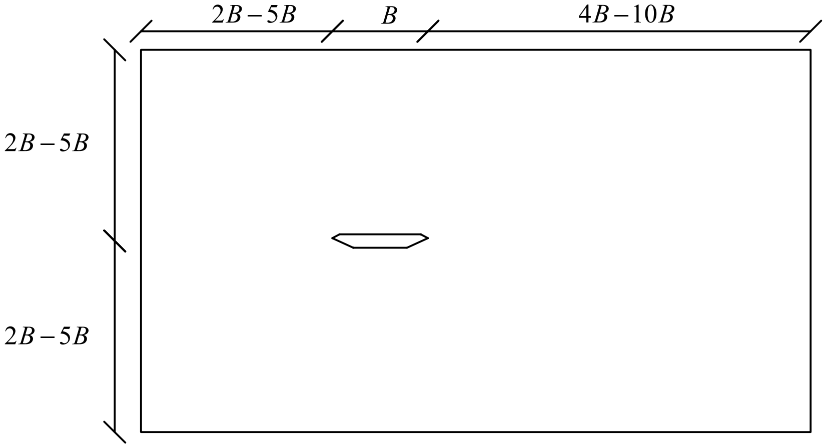

Figure 2: Four different sizes of the domain are analysed

Table 1: Mesh statistics

	4B x 7B	6B x 10B	8B x 13B	10B x 16B
# Nodes	30.802	32.864	36.230	38.478
# Prisms	13.961	16.007	19.362	21.586
# Elements	22.149	24.195	27.550	29.774
Cpu-time for last time step	18,02s	19,05s	21,25s	22,75s

The height of the domain varies from 4B to 10B, and the length varies from 7B to 16B. In Figure 3 the cpu-time is plotted for the different domains. In the analysis the bridge profile undergoes a forced periodic rotation.

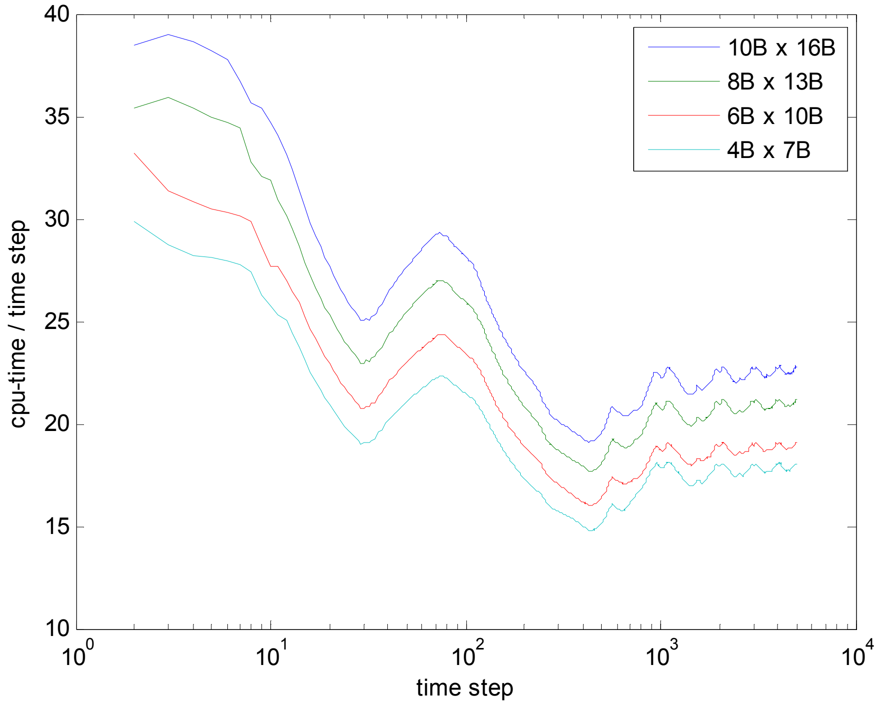

Figure 3: Cpu-time per time step for selected domain sizes.

The importance of the domain size is evaluated by considering the global forces on the bridge and the phase shift of these compared to the harmonic rotation. These values are used when calculating the aerodynamic derivatives. Therefore a small investigation of the importance of the domain size, when considering these values, has been made. The deviations are found from the largest domain introduced. The results can be seen in Table 1.

Table 1: Deviations in percent of the phase shift and force coefficients in four domains.

	Phase shift, lift [%]	Phase shift, moment [%]	C_L [%]	C_M [%]
4B x 7B	-1.98	39.32	-18.71	-10.20
6B x 10B	-0.94	2.56	-9.28	-4.70
8B x 13B	-0.43	-5.58	-3.22	-1.60
10B x 16B	-	-	-	-

As expected, the smallest domain results in the largest deviation, but a significant decrease in the deviations are seen in the following domains. In all the considered values, except the phase shift for the moment for 8Bx13B, a rapid decrease is seen. This deviation can be caused by severe flow conditions around the leading edge of the bridge deck, when this is positioned in the maximum angles of rotation. This is described in more detail in chapter 5. When determining aerodynamic derivatives in two dimensions a domain of $8B \times 15B$ is used. A domain of this size has been found to produce good results in accordance with [Hansen 2008] and [Reinhold et al. 1992].

B.2 STAGNATION

On the front of the bridge profile a point of stagnation is expected. In order to capture this point, a fine mesh is required. The point itself has no further importance to the aeroelastic parameters and it is not easily found in a simulation. However, a refinement of the mesh in this area will capture the contracting streamlines and the strong velocity gradients of the wind, as it approaches the bridge. The mesh is refined in a radius of 10 metres from the leading edge, as shown in Figure 4, to a maximum size of 1 metre. This refinement is coarser than the one near the edge as described in B.5

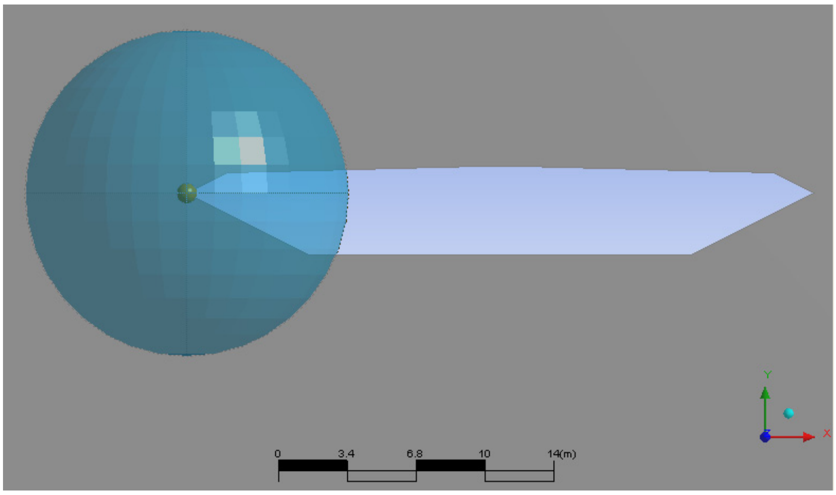

Figure 4: The mesh is refined in the area around the leading edge

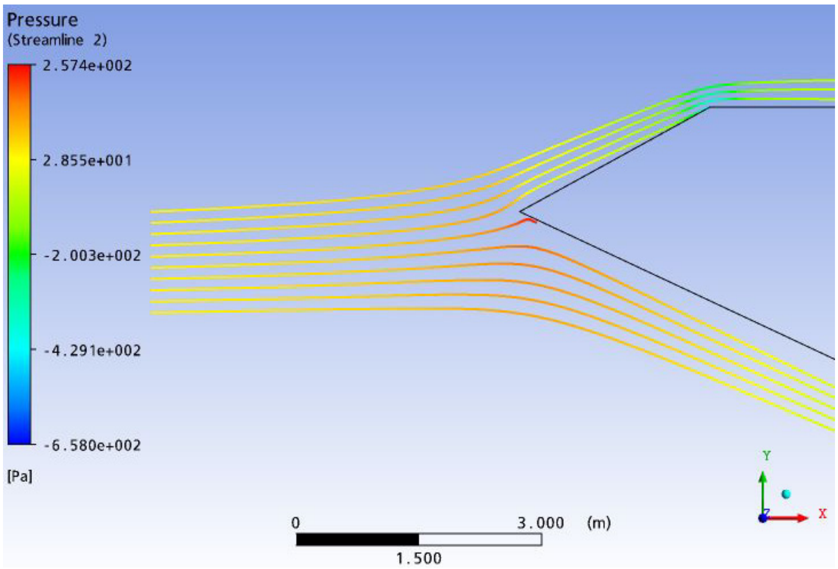

Figure 5: Stagnation and velocity gradients near the leading edge. The streamlines are coloured by the relative pressure

B.3 SEPARATION

Strong adverse pressure gradients are expected to arise when the wind passes over the sharp edges on the top and bottom of the bridge. This will cause the flow to separate from the boundary, forming two standing vortices. The vortex on the top side of the bridge is formed on a sharper edge, resembling a backward facing step. Therefore this vortex is expected more easily to be captured in a simulation. The meshing must be very fine around the edges, where the flow separates from the bridge deck. In order to resolve the vortices, the mesh must also be fine in the area behind the edge, where the flow is turbulent. The mesh near the boundary is dictated by the inflation layer, used to capture the turbulent boundary layer as described in section B.5. Above this, the mesh is set to a maximum size of one metre.

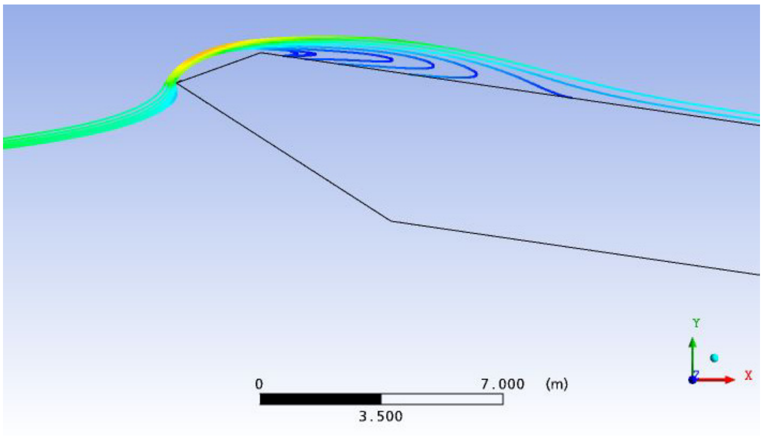

Figure 6: Streamlines around the leading edge visualizes the vortex on the upper part of the bridge. The vortex is captured at an angle of attack of 8,5°, as the bridge is returning to horizontal in a forced harmonic vibration. The figure also captures the reattachment of the flow to the bridge deck.

In Figure 6 it can be seen, that the used mesh captures the vortex very nicely. In the figure, the vortex is captured in a forced harmonic motion, as the bridge is returning to horizontal. No vortex is seen when the bridge is moving away from horizontal.

B.4 REATTACHMENT

After the separation on the top and bottom of the bridge profile the flow is expected to reattach to the surface. This is expected as the width of the bridge is larger than the vortex formed on the edge. The location of the reattachment is not strongly dependent on the size of the mesh. The inflation layer around the profile, as described in section B.5 easily captures the point of reattachment, see Figure 6. The global forces on the bridge deck are very sensitive to the reattachment, as this dictates the size of the vortex where the relative pressure is large.

B.5 BUILD UP OF TURBULENT BOUNDARY LAYER

After the reattachment a turbulent boundary layer is expected to build up. A typical velocity profile for a turbulent boundary layer is given by [Wilcox 2006], see Figure 7.

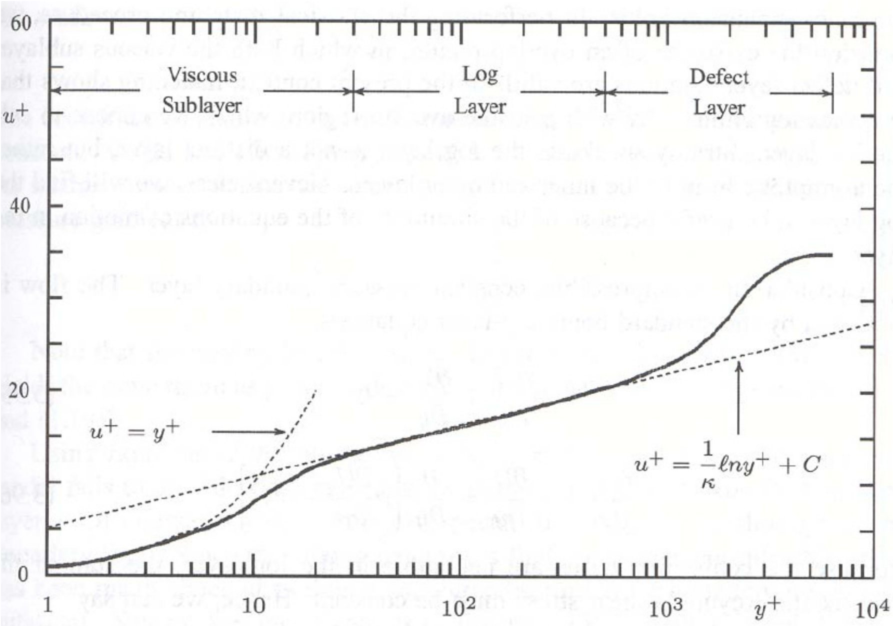

Figure 7: Typical velocity profile for a turbulent boundary layer [Wilcox 2006]

In this model Wilcox introduces the dimensionless velocity u^+ and wall distance y^+ given by

$$u^+ = \frac{U}{u_\tau} \quad \text{and} \quad y^+ = \frac{u_\tau y}{\nu} \tag{B.1}$$

Where

U	is the free stream velocity.
y	is the distance from the wall.
ν	is the kinematic molecular viscosity.
u_τ	is the friction velocity. $u_\tau = \sqrt{\frac{\tau_w}{\rho}}$, where τ_w is the surface shear stress and ρ is the density.

In order to capture the entire boundary layer very small mesh elements are required near the surface. If it is wished to model the viscous sublayer, the dimensionless wall distance needs to be in the region of 1-2, making the element height as small as 0.1mm. The aspect ratio needs to be below approximately 100, which means that the number of mesh elements rapidly grows to around 200.000 around the bridge profile. Such a fine mesh is time consuming not only to generate, but the cpu-time for the simulation also becomes very long. For an analysis of the aerodynamic derivatives the viscous sublayer is not important. In the 2d-simulations the log layer is modelled by the use of rectangular mesh elements, which are 4mm's high near the surface. The size of the elements grows exponentially in an inflated boundary as shown in Figure 8.

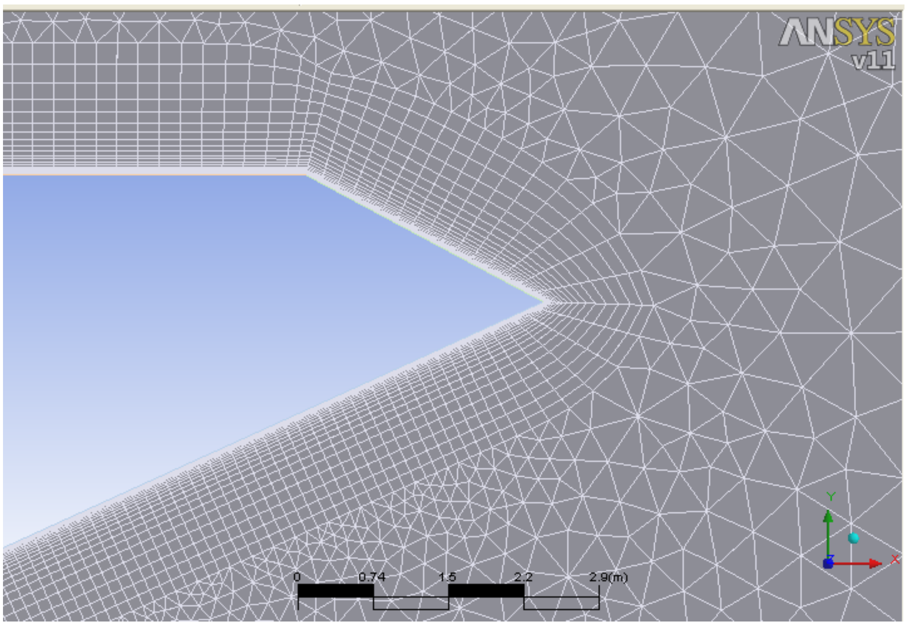

Figure 8: Inflated boundary with 23 layers. First layer thickness is 4mm.

The loglayer is captured with the used mesh, as shown in Figure 9.

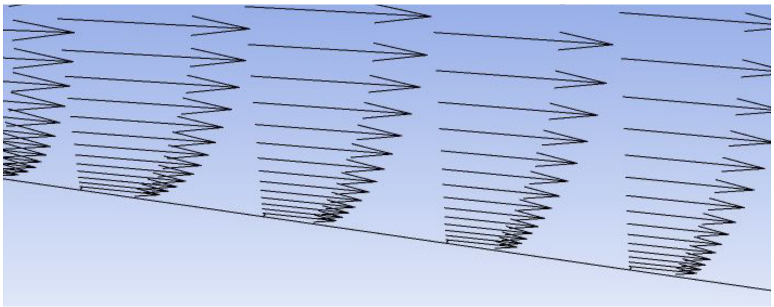

Figure 9: Visualization of loglayer.

Some investigations have been carried out to establish the importance of the loglayer to the global forces and the simulated flow around the bridge. In the turbulent boundary layer friction forces cause great velocity and pressure gradients which may be important to turbulent structure of the flow. However, [Frandsen 1999] has captured vortex shedding with an element thickness of 1 metre near the surface. This indicates that the flow solver in Ansys uses a wall function that substitutes the real boundary layer very well. In the simulations carried out for this project it has not been possible to capture vortex shedding with a mesh structure as coarse as the one used by [Frandsen 1999]. When the inflated boundary mesh is applied, the value of y^+ is as shown in Figure 10.

According to the velocity profile for a turbulent boundary layer, Figure 7, this is sufficiently small to capture the loglayer on most of the surface.

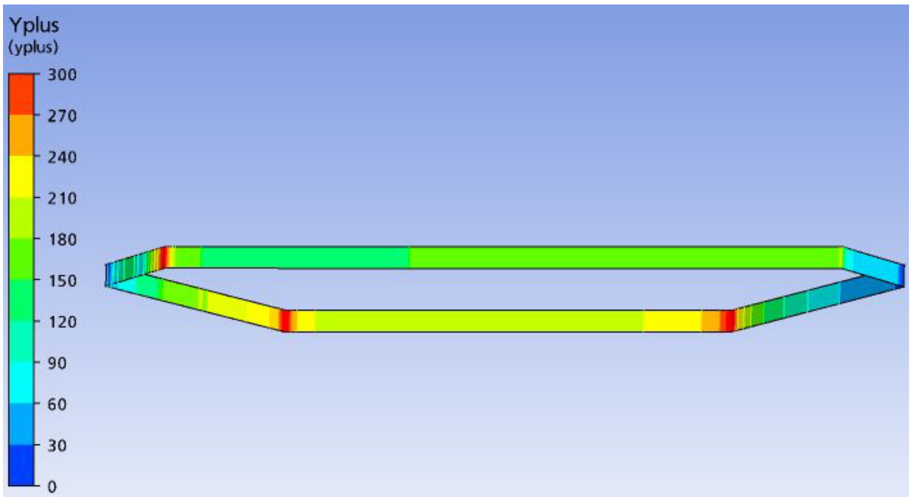

Figure 10: Dimensionless wall distance, y^+.

B.6 SHEDDING

The formation of periodic alternating vortices, von Karman's vortex street, in the wake of the bridge profile is highly dependent on the mesh near the surface and in the area downwind. Naturally the size of the vortices determines the size of the mesh, as the vortices must be resolved in several mesh elements. In Figure 11 a fully developed vortex street is shown, and in Figure 12 it is shown how an increasing element size destroys the vortices. In Figure 11 the mesh is relatively fine in the wake throughout the domain, whereas in Figure 12 the mesh elements are only relatively fine in part of the wake. This indicates that the element size of the wake needs a characteristic length of approximately 0.2 times the diameter of the vortices shed on the bridge. As these Vortices have a diameter of approximately the same size as the height of the bridge profile, the elements in the wake have a characteristic length of 0.25m to 1m.

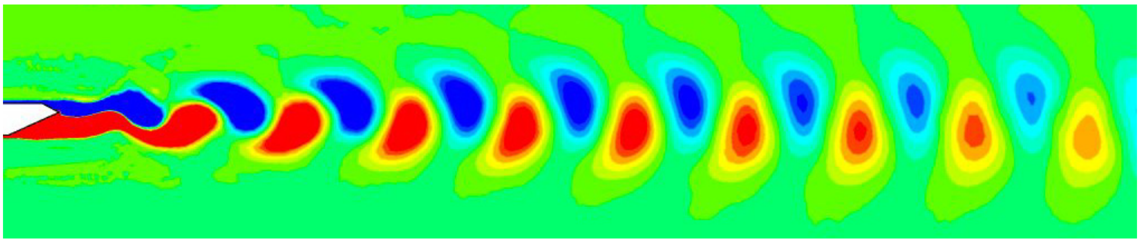

Figure 11: Fully developed vortex street

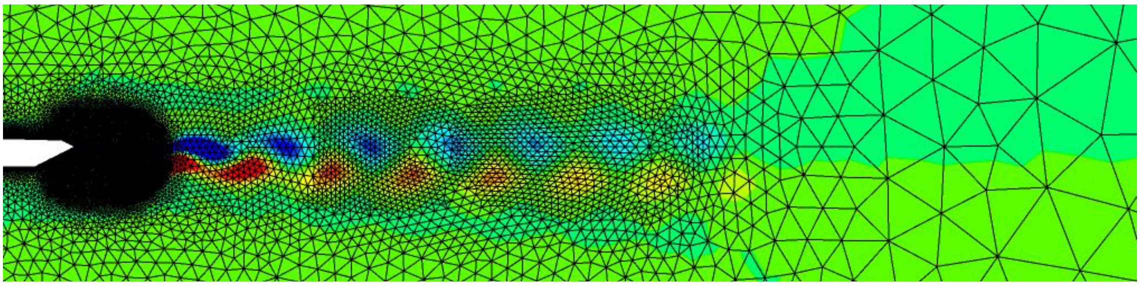

Figure 12: The increasing mesh size downwind destroys the periodic vortex shedding on the bridge.

The element size around the bridge profile also plays a role in the forming of vortices behind the bridge. Very high values of velocity gradients near the surface require a very fine mesh. The vortices on a sharp edged body as a bridge are formed on the edges, as shown in Figure 13. Therefore the mesh requirements near the surface are not due to modelling of a loglayer or a viscous sublayer, which dictates the separation point in a boundary layer.

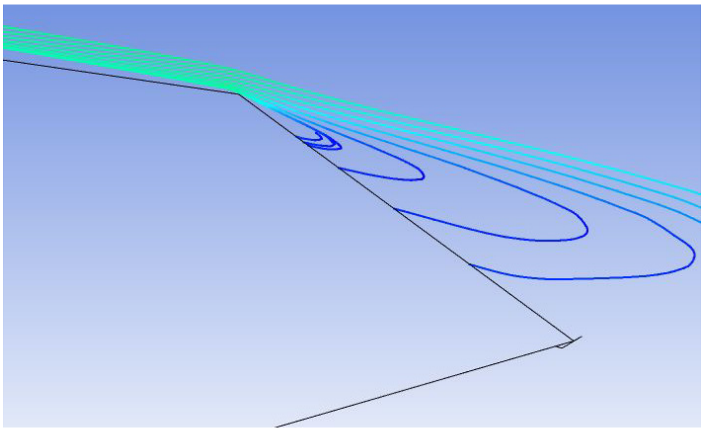

Figure 13: A vortex is formed on the sharp edge of the bridge

An inflated boundary layer, as described in B.5 sufficiently captures the vortices behind the bridge. In Figure 14 the result of a combined simulation is shown. In the first part a vortex street is formed when an inflated boundary layer is used around the bridge profile. In the second part of the simulation the inflated boundary layer is removed, but the remaining mesh is maintained.

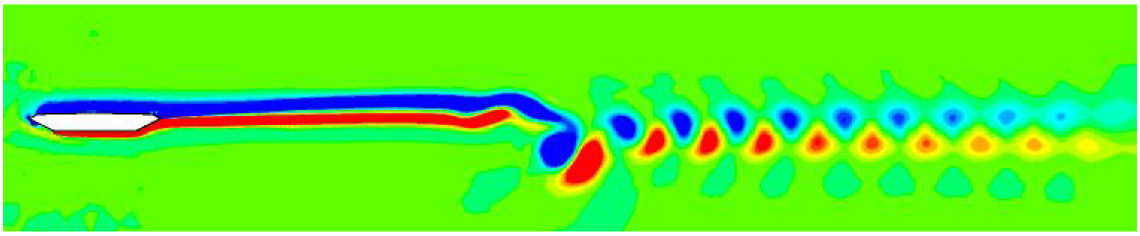

Figure 14: A vortex street is destroyed when the element size around the bridge is increased.

Figure 14 clearly demonstrates the effect of the inflation layer. In *Figure 15* and *Figure 16* the mesh around the bridge profile is shown for the two parts of the simulation.

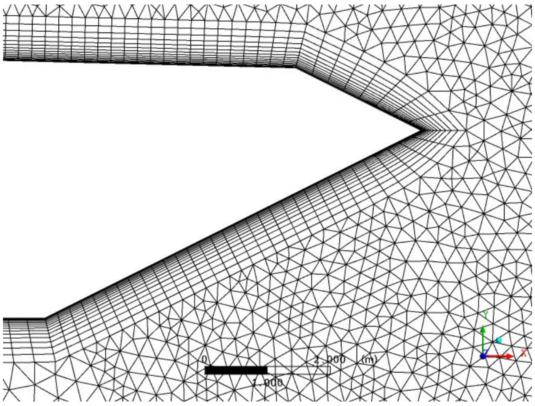

Figure 15: An inflation layer is used to generate a vortex street as shown in Figure 14.

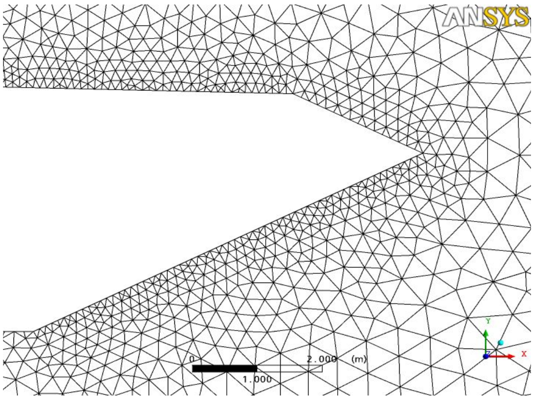

Figure 16: When the inflation layer is removed, the vortex street is destroyed.

B.7 THREE DIMENSIONAL MESH GENERATION

In the following, the meshing strategy for the two different three dimensional flutter analyses is described. The analyses are respectively the 3D forced vibration and the 3D fluid-structure interaction method as described in section 6.4. Due to limitations of computer power and to avoid lengthy simulation running for several weeks, the mesh is far coarser for both 3D cases than the 2D case. It is acknowledged, that the aim of this project is educational and that the results of the simulations therefore are of minor importance. The 3D analyses are meshed so the simulations run for a maximum of approximately 24 hours.

B.8 MESH FOR FORCED VIBRATION TEST

The bridge profile is extruded 124.5 metres from the symmetry plane into a domain with a width of 170 metres. This allows 45.5 metres of ‘free’ flow around the free end of the bridge. The domain is meshed in two stages, in order to use an extruded 2D mesh on the part nearest the plane of symmetry. In Figure 17 this part of the domain is shown along with the bridge. As it can be seen, the bridge is sticking out by 14.5 metres until the domain is closed by the section shown in Figure 18.

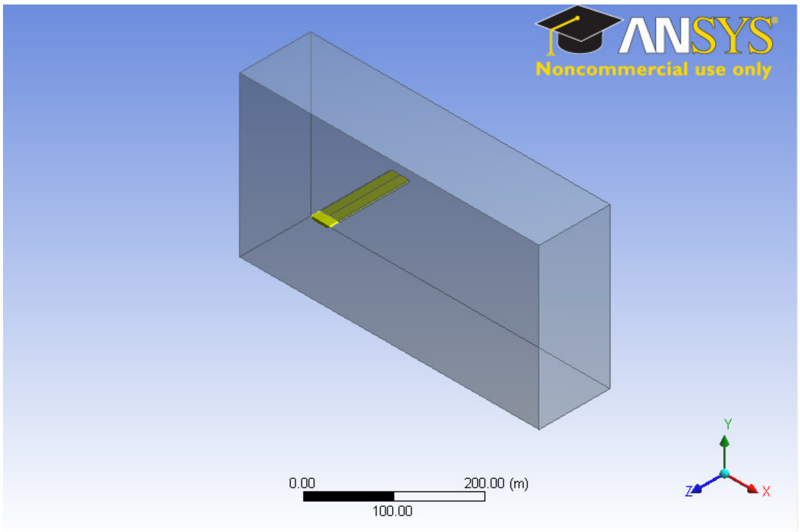

Figure 17: Subdomain 1 near the symmetry plane

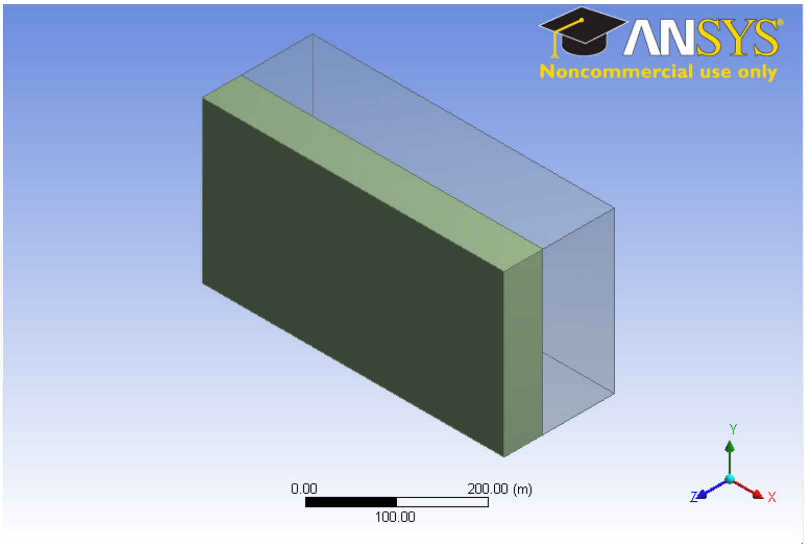

Figure 18: Subdomain 1 and subdomain 2.

The mesh of subdomain 1 is extruded from a 2D mesh generated by the values given in Table 2

Table 2: Values for 2D mesh on the surface of subdomain 1.

Constant edge spacing for bridge profile	0.5 m
Number of inflated layers	5
Height of first inflation layer	1 m
Expansion factor for inflation layer	1.2
Default body spacing	23 m
Default face spacing, angular resolution	30°
Default face spacing, maximum edge length	23 m
Default face spacing, minimum edge length	1.2 m

The generated 2D mesh is shown in Figure 19

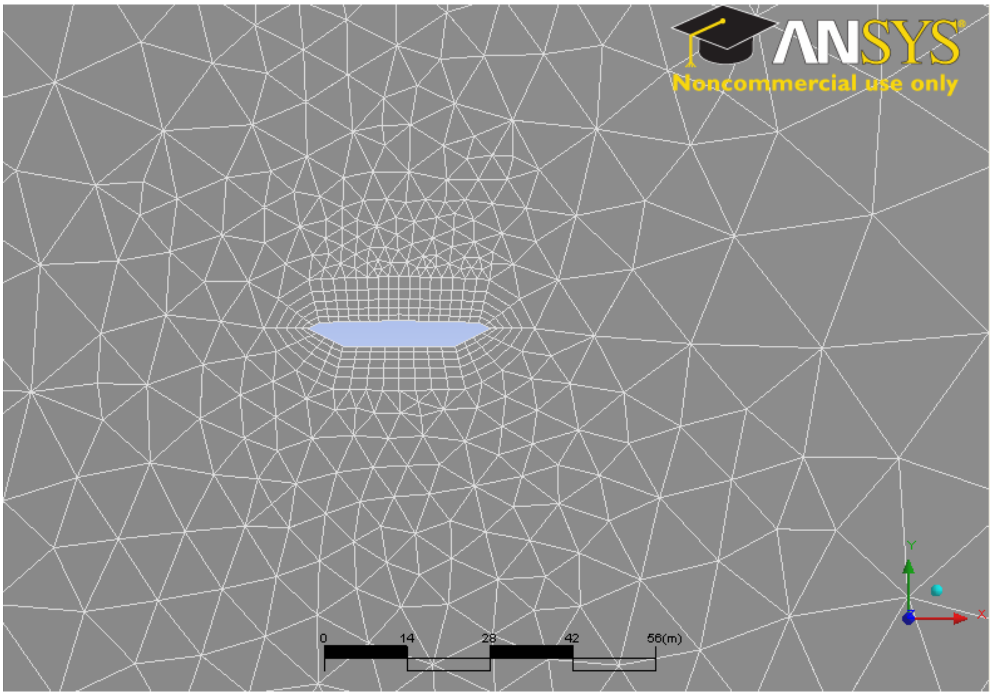

Figure 19: 2D mesh for extrusion into subdomain 1.

The mesh is extruded from the plane of symmetry so the element size is decreasing towards the free end of the bridge. This is shown in Figure 20.

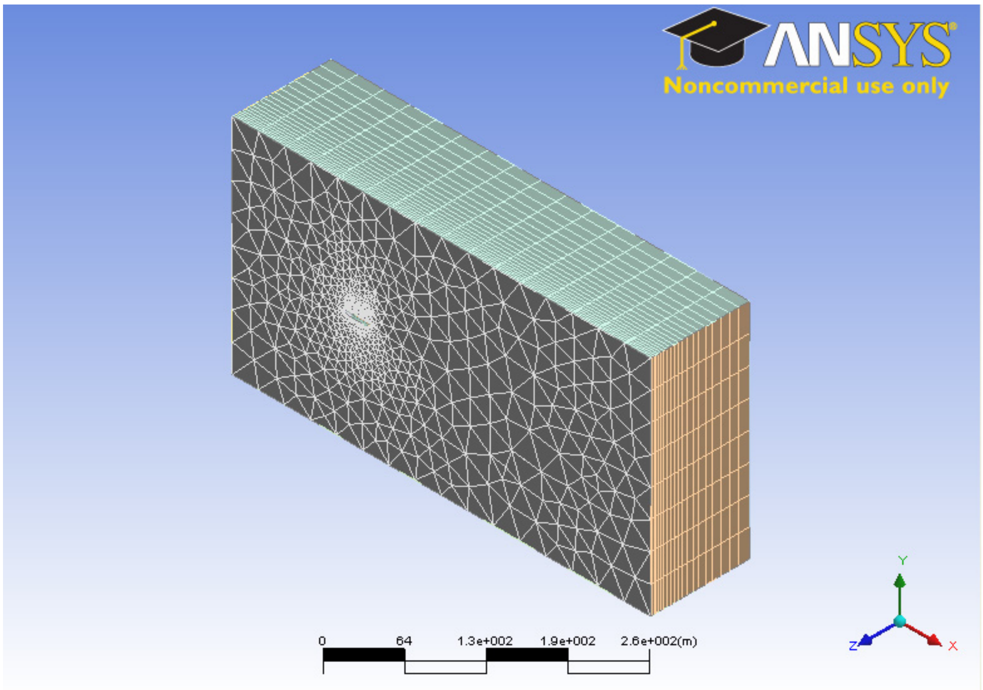

Figure 20: The 2D mesh is extruded with a decreasing size near the free end of the bridge.

The mesh of domain 2 is generated by the same settings around the bridge profile. The only difference from domain 1 is that the 3D mesh is unstructured instead of extruded. The mesh elements around the free end of the bridge have a characteristic length of 0.5 meters.

B.9 MESH FOR FLUID-STRUCTURE INTERACTION

The mesh used when performing a fluid-structure interaction is the coarsest mesh used in this project. The settings for the mesh elements of the domain are mainly the default settings, set by Ansys. The reason for this is the need of a long simulation time. When performing a fluid-structure interaction the simulation time is set to 120 seconds, in order for the oscillating movements to be fully developed. A simulation like this, with the mesh shown in Figure 21 takes around 12-16 hours for the highest velocities used. The settings are given in Table 3.

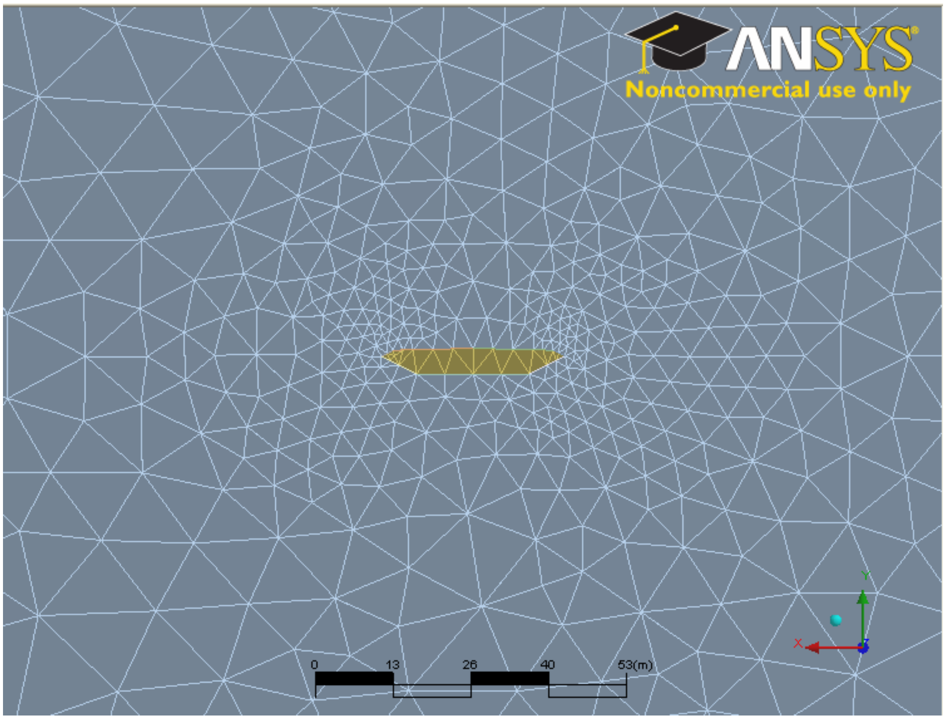

Figure 21: 3D mesh for the domain in a fluid-structure interaction.

Table 3: Settings of 3D mesh of subdomain 2.

Default body spacing	23 m
Default face spacing, angular resolution	30°
Default face spacing, maximum edge length	23 m
Default face spacing, minimum edge length	1.2 m

APPENDIX C: GENERAL TRANSPORT EQUATIONS

In this appendix the governing equations of the fluid flow is briefly described. The main purpose of the appendix is to establish the different schemes used by Ansys CFX, when solving the general transport equations for the fluid domain. This part of the appendix is naturally closely linked to the theory guide of Ansys. Furthermore, the applied types of turbulence modeling are explained. The appendix will not serve as a textbook example of the derivation of transport equations and turbulence models. It will, however briefly introduce the underlying physics of the equations solved in Ansys CFX.

C.1 NAVIER-STOKES EQUATIONS

General equations, describing the fluid flow and heat transfer, some basic physical conservation laws of mass, momentum and energy form the foundation of the calculations. These are Newton's Second Law of Motion, the First Law of Thermodynamics and the mass conservation of a fluid body. The derivation of the general equations is done in many textbooks, and is therefore omitted here. The result is a set of five transport equations and two state equations, constituting the Navier-Stokes equations of the flow of a compressible Newtonian fluid. The equations are given in (C.1).

$$
\begin{aligned}
1: &\quad \frac{\partial p}{\partial t} + \operatorname{div}\left(\rho \boldsymbol{u}\right) = 0 \\
2: &\quad \frac{\partial\left(\rho u\right)}{\partial t} + \operatorname{div}\left(\rho u \boldsymbol{u}\right) = -\frac{\partial p}{\partial x} + \operatorname{div}\left(\mu \cdot \nabla u\right) + S_{Mx} \\
3: &\quad \frac{\partial\left(\rho u\right)}{\partial t} + \operatorname{div}\left(\rho v \boldsymbol{u}\right) = -\frac{\partial p}{\partial y} + \operatorname{div}\left(\mu \cdot \nabla y\right) + S_{My} \\
4: &\quad \frac{\partial\left(\rho u\right)}{\partial t} + \operatorname{div}\left(\rho w \boldsymbol{u}\right) = -\frac{\partial p}{\partial z} + \operatorname{div}\left(\mu \cdot \nabla w\right) + S_{Mz} \\
5: &\quad \frac{\partial\left(\rho i\right)}{\partial t} + \operatorname{div}\left(\rho i \boldsymbol{u}\right) = -p \cdot \operatorname{div} \boldsymbol{u} + \operatorname{div}\left(k \cdot \nabla T\right) + \Phi + S_i \\
6: &\quad p = p\left(\rho, T\right) \\
7: &\quad i = i\left(\rho, T\right)
\end{aligned}
\tag{C.1}
$$

where

p	is the pressure
t	is the time
ρ	is the density

$\boldsymbol{u}$	is the velocity vector
x, y, z	are cartesian coordinates
u, v, w	are velocities in direction of x, y and z
μ	is the molecular viscosity
S	is a source term
i	is static enthalpy
k	is the thermal conductivity
Φ	is a dissipation function
T	is the temperature

[Malalasekera and Versteeg 2007]

The first equation expresses the mass conservation in three dimensions. Equations 2-4 express the conservation of momentum in three dimensions. The fifth equation expresses the conservation of energy in three dimensions, while equations 6 and 7 are constitutive relations, linking four thermodynamic variables: pressure, density, static enthalpy and temperature. In general, the resulting system provides seven equations and seven unknowns.

When the fluid or gas flows at low speeds it is customary to regard them as incompressible, leaving no density variations in the domain. Without density variations the equations can often be solved merely by considering the continuity and momentum equations. Equation five, the energy equation, needs only to be solved when a heat transfer is of interest.

C.2 DISCRETIZATION OF NAVIER-STOKES EQUATIONS

Only in very rare occasions, an analytical solution to the Navier-Stokes equations is possible. In most cases, a discretization of the fluid domain is necessary. In the following, it is described how Ansys CFX discretizes and solves the seven equations given in (C.1). In the process of discretization, a mesh is generated. Ansys CFX creates control volumes around each node, confined by the surrounding elements as shown in Figure 22. In general the volumes are not two-dimensional, with a unit depth as shown in Figure 22, but fully three-dimensional. The variables of the Navier-Stokes equations are integrated over the control volume to ensure conservation of mass, momentum and energy at every discrete volume. The variables are stored at the element nodes.

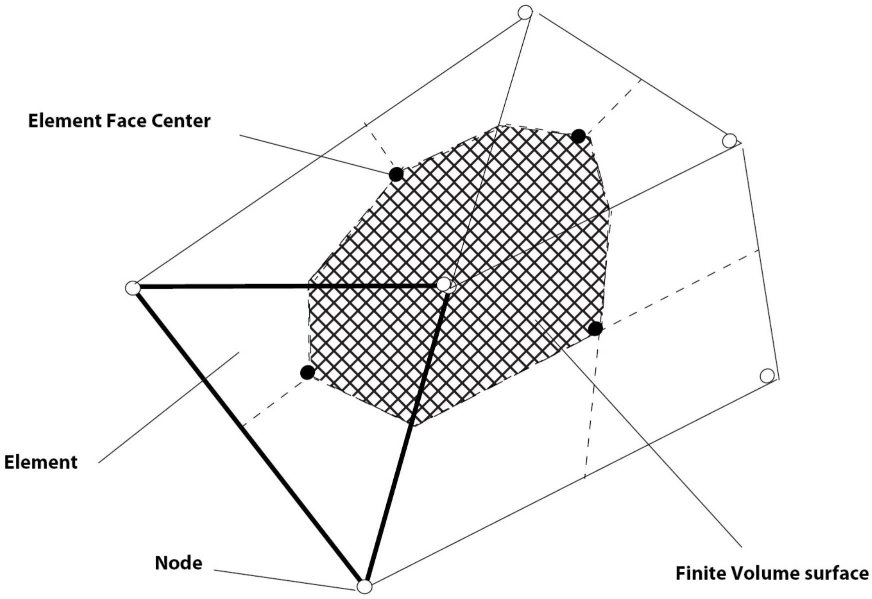

Figure 22: Control volume (hatched area) is confined by the surrounding elements.[Ansys 2006]

Volumetric values, such as the source terms are approximated in each sector as shown in Figure 23 and integrated over all the segments constituting the control volume. Area terms are approximated at integration points on the surface of the control volume and integrated over the entire surface.

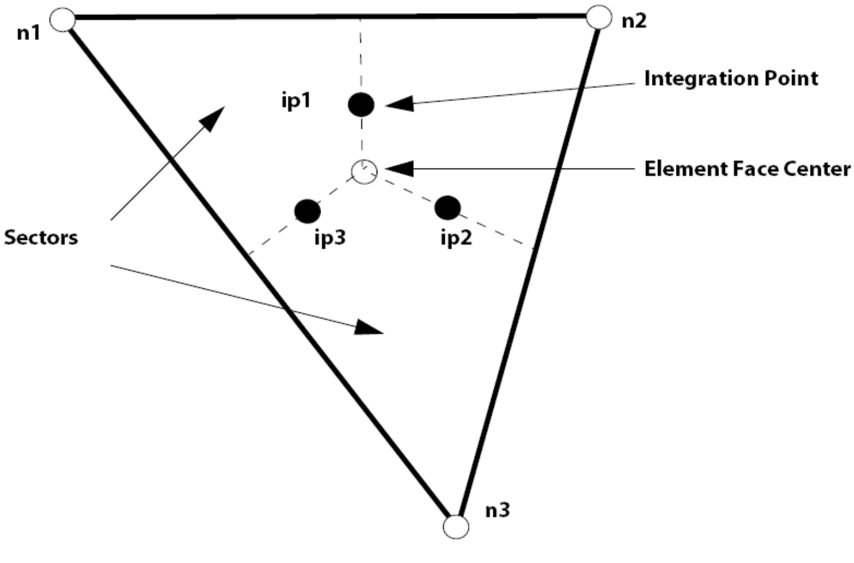

Figure 23: Mesh element [Ansys 2006]

The discrete form of the momentum equation is shown in (C.2) as an example.

$$V\left(\frac{\rho u-\rho^{0}u^{0}}{\Delta t}\right)+\sum_{ip}\left(\left(\rho U_{i}\Delta n_{i}\right)_{ip}u_{ip}\right)=\sum_{ip}\left(P\Delta n\right)_{ip}+\sum_{ip}\left(\mu_{eff}\nabla u\Delta n_{i}\right)_{ip}+\overline{S_{Mx}}V \tag{C.2}$$

where

V	is the control volume
Δt	is the time step
Δn_i	is the outward normal vector for the surface
μ_{eff}	is the effective viscosity. A sum of the molecular and the eddie viscosity.

An overbar indicates a mean value, a superscript *0* indicates a value from the previous step and a subscript *ip* indicates the integration points.

C.3 TRANSIENT SCHEME

When solving transient analysis, Ansys provides two different schemes for updating values from one time step to the next. These are respectively the *first-* and *second order backward Euler* methods. The following equations are only valid for stationary mesh elements, i.e. no change in the geometry of the control volumes. For the *first order backward Euler* method, the discrete formulation of the *n*th transient term is given by (C.3).

$$\frac{\partial}{\partial t}\int_{V}\left(\rho\theta\right)^{n}dV=V\frac{\left(\rho\theta\right)^{n}-\left(\rho\theta\right)^{n-1}}{\Delta t} \tag{C.3}$$

The *first order backward Euler* method is a stable scheme which is first order accurate with the chosen time step. However, the scheme tends to introduce discretization errors, and is therefore not used in the analysis of the present project. [Ansys 2006]

The discrete formulation of the *second order backward Euler* scheme for the nth transient term is given by (C.4) to (C.6)

$$\frac{\partial}{\partial t}\int_{V}\left(\rho\phi\right)^{n}dV\approx V\frac{\left(\rho\phi\right)^{n+½}-\left(\rho\phi\right)^{n-½}}{\Delta t} \tag{C.4}$$

$$\left(\rho\phi\right)^{n-½}=\left(\rho\phi\right)^{n-1}+\frac{1}{2}\left(\left(\rho\phi\right)^{n-1}-\left(\rho\phi\right)^{n-2}\right) \tag{C.5}$$

$$\left(\rho\phi\right)^{n+½}=\left(\rho\phi\right)^{n}+\frac{1}{2}\left(\left(\rho\phi\right)^{n}-\left(\rho\phi\right)^{n-1}\right) \tag{C.6}$$

The *second order backward Euler* is a less stable algorithm, but second order accurate with the chosen time step [Ansys 2006]. This scheme is used in the transient analysis of the present project.

C.4 ADVECTION SCHEME

When running a transient simulation, Ansys provides three different schemes for solving the advection term in the Navier-Stokes equations. All three are variations of the general equation in (C.7).

$$\phi_{ip} = \phi_{up} + \beta \nabla \phi \cdot \Delta \bar{r} \tag{C.7}$$

where

ϕ	is the quantity of interest
β	is a coefficient, $0 \le \beta \le 1$.
$\nabla \phi$	is the average of the adjacent nodal gradients when using the *specified blend scheme* and $\nabla \phi$ is the nodal gradient of the upwind node when using the *high resolution scheme.*
$\bar{r}$	is the vector from the upwind node to the integration point.

The three different advection schemes are described in the following:

- In the *upwind differencing scheme*, a value of $\beta = 0$ is applied. The scheme is very stable, but is likely to introduce discretization errors, smearing out steep gradients of the variables in space. This is shown in Figure 24.

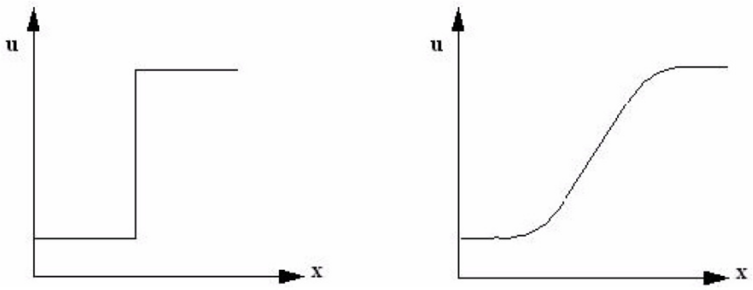

Figure 24: The figure shows how a steep spatial gradient on the left is smeared out on the right by the use of the upwind differencing scheme [Ansys 2006].

- When using the *specified blend scheme*, the user is allowed to set the value of β manually. A choice of $\beta = 1$ is theoretically second order accurate in space, i.e. with the chosen element size. However, a choice of $\beta = 1$ introduces a secondary oscillating error, when approximating steep spatial gradients, as shown in Figure 25. [Ansys 2006]

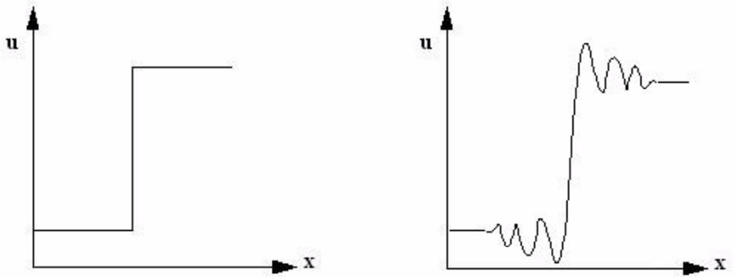

Figure 25: The figure shows how a steep spatial gradient on the left is approximated on the right by the use of the specified blend scheme [Ansys 2006].

- The last method is the *high resolution scheme*, which will set a value of β as close to one as possible without introducing the oscillations shown in Figure 25. The advantage of the scheme is that it will solve most of the domain with a second order spatial accuracy, only reducing the value of β in regions of steep gradients. This method is used in the simulations in the present project.

C.5 TIME STEP INITIALIZATION

When solving a simulation using the *second order backward Euler* scheme, there are three different options for initializing the time step iteration:

- The *Previous time* step option simply uses the solution of the last time step to initialize the current.
- The *Extrapolation* option uses the two previous solutions to extrapolate to the current time step initialization.
- The *Automatic* option evaluates the Courant number for every mesh element. The Courant number is defined in one dimension in (C.8).

$$Courant = \frac{u\Delta t}{\Delta x} \tag{C.8}$$

The Courant number needs to be sufficiently low in transient analysis for the solution to converge. When using the second order backward Euler scheme, and the automatic time step initialization, Ansys will use a blend of previous time step and extrapolation if the Courant number is between five and ten. For values below five, previous time step is used, and for values above ten, the extrapolation method is used.

C.6 TURBULENCE MODELLING

In theory, the Navier-Stokes equations presented in section C.1 fully describe any fluid flow. However, in order to resolve the finest turbulence scales of interest, the mesh size needs to be sufficiently small. This leads to use of many elements and thereby requiring computer processors far more powerful than the ones available today or in the near future. To solve this problem, a method, known as *Direct Numerical Simulation*, DNS, is normally used, but only for detailed simulations where the range of the turbulence is small. In the present project this approach is not an option, due to the nature of the turbulent structure of the atmospheric boundary layer. Turbulence is represented in very wide spectrum, ranging from the low frequency scales from vortices which may be several times larger than the considered structure to the highest frequency turbulence created on the surface of the bridge.

C.7 REYNOLDS AVERAGING

In practical applications a turbulence model is often applied, simplifying the turbulent structure in different ways. Many of the most well known and well tested turbulence models are based on Reynolds time averaging, assuming that a turbulent flow may be separated into a mean flow and a fluctuating part. This is formally stated for the x-component of the velocity vector in (C.9).

$$u = U + u' \tag{C.9}$$

where

- u is the x-component of the velocity vector
- U is the mean value of u
- u' is the fluctuating part of u.

A similar separation is used for the total velocity vector **u**, and the pressure, *p*. It is customary to disregard the fluctuations in density and viscosity of the flow. If (C.9) is inserted into the momentum equation (C.1), the time averaged *x*-momentum equation is found.

$$\frac{\partial U}{\partial t} + \mathrm{div}\left(U\mathrm{U}\right) + \mathrm{div}\overline{\left(u'\mathrm{u}'\right)} = -\frac{1}{\rho}\frac{\partial P}{\partial x} + \nu \cdot \mathrm{div}\left(\mathrm{grad}\left(U\right)\right) \tag{C.10}$$

where

- ν is the kinematic molecular viscosity, $\nu = \dfrac{\mu}{\rho}$

An overbar indicates a time averaged value.

[Malalasekera and Versteeg 2007]

In (C.10) the source term in (C.1) has been omitted for the sake of simplicity. To a very large extent, equation (C.10) looks like (C.1), with just one term in difference. A time averaging of the fluctuating part of the velocity has been introduced into the equation. Similar equations are made for the two remaining directions. When expanding (C.10) and rearranging the terms so that the fluctuating parts are on the right hand side of the equation, it shows that six new unknowns have been introduced. These terms are known as the Reynolds stresses, and these are the keystones to the classical theory of turbulence modeling. The stresses are given in (C.11).

$$\begin{aligned}
\tau_{xx} &= -\rho\overline{u'^2} \\
\tau_{yy} &= -\rho\overline{v'^2} \\
\tau_{zz} &= -\rho\overline{w'^2} \\
\tau_{xy} &= \tau_{yx} = -\rho\overline{u'v'} \\
\tau_{xz} &= \tau_{zx} = -\rho\overline{u'w'} \\
\tau_{yz} &= \tau_{zy} = -\rho\overline{v'w'}
\end{aligned} \tag{C.11}$$

C.8 WILCOX' K-Ω MODEL

In order to close the undetermined system of 13 unknowns and only seven equations, an additional six equations are needed. For the type of turbulence models treated here, the Boussinesq Approximation shown in (C.12) is assumed to be valid.

$$\tau_{ij} = 2\nu_T S_{ij} - \frac{2}{3}k\delta_{ij} = \nu_T\left(\frac{\partial U_i}{\partial x_j} + \frac{\partial U_j}{\partial x_i}\right) - \frac{2}{3}k\delta_{ij} \tag{C.12}$$

where

τ_{ij}	is the Reynold's Stress Tensor.
ν_T	is the fluctuating velocity vector, consisting of *u'*, *v'* and *w'*.
S_{ij}	is the mean strain rate tensor.
k	is the kinetic turbulence energy, as defined in (C.13).
δ_{ij}	is the Kronecker Delta

This reduces the problem, as the elements of the Reynold's Stress Tensor are approximated by the mean strain rate tensor. In classical turbulence models for Reynolds-averaged Navier-Stokes (RANS) equations, models are closed by simplifying the turbulence by the kinetic turbulence energy and a turbulent length scale. The kinetic energy in the fluctuating part of the flow is defined in (C.13).

$$k = \frac{1}{2}\left(\overline{u'_i u'_i}\right) = \frac{1}{2}\left(\overline{u'^2} + \overline{v'^2} + \overline{w'^2}\right) \tag{C.13}$$

where

k is the specific kinetic energy of the fluctuating part of the flow.

u'_i is the fluctuating velocity vector, consisting of *u'*, *v'* and *w'*.

[Wilcox 2006]

It is widely recognized, that an additional transport equation of *k* will provide a good and physical basis of a turbulence model. It furthermore introduces an additional equation to the problem. The general transport equation for the turbulence kinetic energy is given in (C.14).

$$\frac{\partial k}{\partial t} + U_j \frac{\partial k}{\partial x_j} = \tau_{ij} \frac{U_i}{\partial x_j} - \varepsilon + \frac{\partial}{\partial x_j}\left[\nu \frac{\partial k}{\partial x_j} - \frac{1}{2}\overline{u'_i u'_i u'_j} - \frac{1}{\rho}\overline{p' u'_j}\right] \tag{C.14}$$

The derivation of (C.14) is somewhat lengthy, and can be seen in [Wilcox 2006]. The quantity ε is known as the dissipation per unit mass, defined in (C.15).

$$\varepsilon = \nu \overline{\frac{\partial u'_i}{\partial u'_j} \frac{\partial u'_j}{\partial u'_i}} \tag{C.15}$$

where

ν is the kinematic molecular viscosity, $\nu = \frac{\mu}{\rho}$.

Some turbulence models, the so called *one equation models,* will solve the RANS-equations by means of (C.14) alone. In order to close the system of equations these models will require some knowledge of the length scale of the turbulent structure. Due to this, one equation models are referred to as incomplete.

In the present project, the fluid domain is solved by the use of Wilcox' *k-ω* turbulence model. This introduces an equation for the turbulence length scale, in the form of the variable *ω*. In the literature the nature of this variable is found to be less clear than the interpretation of *k*. It is noted in [Wilcox 2006] that "… ω^2 is the mean square vorticity of the energy containing eddies", or that "… ω is a frequency characteristic of the turbulence decay process under its self-interaction". Wilcox himself simply regards ω as the ratio of ε to *k*. A transport equation is made for ω, much similar to (C.14). The transport equation is shown in (C.16).

$$\frac{\partial \omega}{\partial t} + U_j \frac{\partial \omega}{\partial x_j} = \alpha \frac{\omega}{k} \tau_{ij} \frac{\partial U_i}{\partial x_j} - \beta \omega^2 + \frac{\sigma_d}{\omega} \frac{\partial k}{\partial x_j} \frac{\partial \omega}{\partial x_j} + \frac{\partial}{\partial x_j}\left[\left(\nu + \sigma \frac{k}{\omega}\right) \frac{\partial \omega}{\partial x_j}\right] \tag{C.16}$$

However, [Menter 1993] has implied that the equation not satisfactorily accounts for the transport shear stress. Therefore an implementation of a so called stress limiter has been made to the classical *k-ω* model. The stress limiter is given in (C.17).

$$\nu_T = \frac{k}{\tilde{\omega}}, \qquad \tilde{\omega} = \max\left\{\omega, \frac{7}{8}\sqrt{\frac{2S_{ij}S_{ij}}{\beta}}\right\} \tag{C.17}$$

Where

β is a constant

[Wilcox 2006]

In equation (C.16) and (C.17) a series of coefficients are needed to close the problem. These coefficients are given in [Wilcox 2006] and in the Ansys theory guide. The turbulence model presented in (C.16) is referred to, as the Wilcox 2006 model by the author himself. Menter has furthermore implemented so called blending functions, which will blend the k-omega model with the classical k-epsilon model. This mix of the two turbulence models is solved in Ansys CFX, when choosing the *Shear Stress Transport* option.

When choosing the SST model, Ansys solves the classical k-epsilon model for the free flow in the domain, while the k-omega model is solved near boundaries. Ansys recommends the SST model for high accuracy boundary layer simulations. This turbulence model has been used in the simulations of this project.